



City Research Online

City, University of London Institutional Repository

Citation: Dionysios, S. (2020). Direct numerical simulation of secondary droplet breakup in fuel sprays. (Unpublished Doctoral thesis, City, University of London)

This is the accepted version of the paper.

This version of the publication may differ from the final published version.

Permanent repository link: <https://openaccess.city.ac.uk/id/eprint/24741/>

Link to published version:

Copyright: City Research Online aims to make research outputs of City, University of London available to a wider audience. Copyright and Moral Rights remain with the author(s) and/or copyright holders. URLs from City Research Online may be freely distributed and linked to.

Reuse: Copies of full items can be used for personal research or study, educational, or not-for-profit purposes without prior permission or charge. Provided that the authors, title and full bibliographic details are credited, a hyperlink and/or URL is given for the original metadata page and the content is not changed in any way.

Direct numerical simulation of secondary droplet breakup in fuel sprays

Stefanitsis Dionysios

Thesis submitted for the fulfilment of the requirements for
the Degree of Doctor of Philosophy



**School of Mathematics, Computer Science &
Engineering**

Department of Mechanical Engineering & Aeronautics

March 2020



“Η αρχή της σοφίας είναι η αναζήτηση” translation: “Wonder is the beginning of wisdom”

Socrates, 469-399 BC.

...to my family...

Contents

Contents	vii
List of Figures	xi
List of Tables	xvii
Acknowledgements	xix
Declaration	xxi
Abstract	xxiii
Thesis Contribution	xxv
Nomenclature	xxvii
Chapter 1 Introduction	1
1.1 Background and Motivation.....	1
1.1.1 Motivation.....	1
1.1.2 Non-dimensional numbers.....	3
1.1.3 Breakup modes	4
1.2 Literature review	5
1.2.1 Isolated droplet breakup.....	5
1.2.2 Cluster droplet breakup	10
1.2.3 Analytical models for droplet deformation and breakup.....	12
1.3 Scope of the PhD thesis - Novelty	18
1.4 Thesis outline.....	21
Chapter 2 Numerical models	23
2.1 Numerical model for droplet breakup	23
2.1.1 Flow equations and volume of fluid (VOF) method	23
2.1.2 Equations of state (EoS) and rest of fluid properties	25
2.1.3 VOF-to-DPM model	26
2.2 Numerical settings, assumptions and grid	27

Chapter 3 Model Validation.....	31
3.1 Introduction.....	31
3.2 Droplet breakup at low Mach numbers.....	31
3.2.1 Computational setup.....	31
3.2.2 Examined conditions.....	32
3.2.3 CFD results – comparison against experimental studies.....	33
3.2.4 Conclusions.....	40
3.3 Droplet breakup at high Mach numbers.....	41
3.3.1 Computational setup.....	41
3.3.2 Examined conditions.....	42
3.3.3 CFD results – comparison against experimental and numerical studies.....	42
3.3.4 Conclusions.....	46
Chapter 4 Isolated droplet breakup.....	47
4.1 Introduction.....	47
4.2 Low Mach number simulations.....	47
4.2.1 Computational setup and examined conditions.....	47
4.2.2 CFD results.....	48
4.3 High Mach number simulation.....	57
4.3.1 Computational setup and examined conditions.....	57
4.3.2 CFD results.....	58
Chapter 5 Cluster droplet breakup.....	65
5.1 Introduction.....	65
5.2 Tandem formation.....	65
5.2.1 Computational setup and examined conditions.....	65
5.2.2 CFD results.....	67
5.3 Single-sheet clusters.....	78
5.3.1 Computational setup and examined conditions.....	78
5.3.2 CFD Results.....	81
5.4 Multi-sheet clusters.....	88
5.4.1 Computational setup and examined conditions.....	88
5.4.2 CFD Results.....	89
5.5 Conclusions.....	98
Chapter 6 Analytical models for droplet deformation and breakup.....	101

6.1 Introduction	101
6.2 Mathematical models.....	101
6.2.1 Improved TAB model.....	101
6.2.2 Modified model based on the Navier-Stokes equations (M-NS).....	103
6.2.3 Unified secondary breakup model	106
6.2.4 Breakup condition	110
6.3 Computational setup and examined conditions of the CFD simulations	111
6.4 Results – comparison of analytical models with CFD simulations ...	112
6.4.1 Bag breakup regime – $We=10-20$	113
6.4.2 Multi-mode breakup regime – $We=21-65$	113
6.4.3 Sheet-thinning breakup regime – $We=66-350$	114
6.5 Conclusions.....	115
Chapter 7 Conclusions and future work	117
7.1 Conclusions.....	117
7.2 Future work	118
Appendix A . Difference between the RCD of the current work with that of a seven-droplet chain.....	121
Publications.....	123
Bibliography	125

List of Figures

Figure 1-1: Physical phenomena in fuel injection equipment.	2
Figure 1-2: Breakup modes as function of the We number [4].	4
Figure 1-3: Definition of the cross-stream droplet diameter and the non-dimensional droplet deformation.	12
Figure 1-4: Comparison between experimental data and the predictions of the various empirical models for the temporal evolution of droplet deformation for: a) $We=15$, b) $We=20$, c) $We=52.6$ and d) $We=101$	14
Figure 1-5: Comparison between experimental data and the predictions of the various theoretical models for the temporal evolution of droplet deformation for: a) $We=15$, b) $We=20$, c) $We=52.6$ and d) $We=101$	18
Figure 1-6: Examined parameters of the current and previous numerical studies presented in a) the $Oh-We$ plane and b) the $Re-N/\varepsilon$ plane. The representative Diesel and HFO engine conditions are drawn based on [7, 96, 97].	19
Figure 1-7: Examined We , a) L/D_0 and b) H/D_0 numbers in the current and previous numerical studies.	20
Figure 2-1: Droplet shape depicted with the VOF iso-values of: 0.01 (green line), 0.5 (black line) and 0.99 (red line).	28
Figure 2-2: Levels of local refinement around the liquid-gas interface.	30
Figure 3-1: Computational domain utilized for the a) 2-D axisymmetric and b) 3-D simulations of droplet breakup at low Mach numbers.	32
Figure 3-2: Temporal evolution of a) droplet shape and b) deformation, from the simulation of case 1 ($We=14$) and the experiment of Arcoumanis et al. [14].	34
Figure 3-3: Temporal evolution of droplet shape as predicted by: a) the 2-D axisymmetric simulation of case 2 ($We=54$), b) the 3-D simulation of case 2, and c) the experiment of Liu and Reitz [18].	35
Figure 3-4: Temporal evolution of droplet shape from the 3-D simulation of case 2 ($We=54$).	35

Figure 3-5: Droplet deformation for the simulation of case 2 ($We=54$) and the experiment of Liu and Reitz [18] as function of the distance travelled in the cross-stream direction.	36
Figure 3-6: Vortex shedding in the 3-D simulation of case 2 at various time instances (streamlines coloured with velocity magnitude).	37
Figure 3-7: Temporal evolution of droplet shape for: a) case 3 ($We=254$, $\varepsilon=695$) and the experiment of Liu and Reitz [18], and b) case 4 ($We=264$, $\varepsilon=79$) and the experiment of Lee and Reitz [19].	38
Figure 3-8: Droplet deformation for the simulation of case 3 ($We=254$) and the experiment of Liu and Reitz [18] as function of the distance travelled in the cross-stream direction.	39
Figure 3-9: Temporal variation of the cross-stream deformation for all validation cases.	39
Figure 3-10: Non-dimensional droplet velocity as function of modified time for all validation cases and the experiment of Dai and Faeth [77].	40
Figure 3-11: Predicted breakup initiation time as function of the We number for the validation cases along with the experimental correlations of Pilch and Erdman [38] and Dai and Faeth [77].	40
Figure 3-12: 2-D planar computational domain used for the simulation of water droplet breakup at high Ma number.	42
Figure 3-13: Pressure and Schlieren contours from the 2-D simulation of shock-wave induced droplet breakup ($\alpha=0.5$). Flow is from left to right.	43
Figure 3-14: Pressure and Schlieren contours as predicted by the simulation of [139] ($\alpha=0.9$). Flow is from left to right.	44
Figure 3-15: a) Holographic interferograms from the experiment of Igra and Takayama [142] and numerical schlieren images from the simulations of b) Meng and Colonius [139] and c) the current study, at two time instances. Flow is from left to right.	45
Figure 3-16: Temporal evolution of the non-dimensional a) streamwise deformation, b) cross-stream deformation and c) leading-edge displacement of the droplet, as predicted by the experiment of [142], the simulation of [139] and the simulation of the current work ($a=0.5$).	46
Figure 4-1: Temporal evolution of droplet shape for three We numbers and three Oh numbers ($\varepsilon=72$).	49
Figure 4-2: Temporal evolution of both main axes deformations (D_{cr} , D_{str}) for three Oh numbers and a) $We=54$ and $\varepsilon>694$, and b) $We=254$ and $\varepsilon=72$. The solid lines correspond to the cross-stream deformation and the dashed ones to the stream-wise one.	49

Figure 4-3: Temporal evolution of liquid surface area for three Oh numbers and a) $We=54$ and $\epsilon>694$, and b) $We=254$ and $\epsilon=72$	50
Figure 4-4: Temporal evolution of drag coefficient for three cases with $We=54$, $\epsilon>694$ and three Oh numbers.	51
Figure 4-5: Temporal evolution of droplet shape for $We=54$, $Oh=0.96$ and two density ratios.....	52
Figure 4-6: Temporal evolution of liquid surface area for seven cases with density ratios ranging from 5 up to 700 and close We numbers (264 up to 279).	53
Figure 4-7: a) Temporal evolution of drag coefficient for three cases with $\epsilon=10$, 112 and 700, and b) time-averaged drag coefficient as function of Re for various cases in the three breakup modes: bag, multi-bag and sheet-thinning.....	54
Figure 4-8: Breakup initiation time as predicted by eq. (4-3) (data points) and the simulations (straight lines).	55
Figure 4-9: Drag coefficient as function of Re number for solid sphere, solid disk and for deforming droplets calculated by the CFD simulations and correlation (2-6).	56
Figure 4-10: 3-D computational domain utilized for the simulation of droplet breakup at high Ma number.	58
Figure 4-11: Temporal evolution of droplet deformation as predicted by a) the experiment of [34], b) the simulation of [52] ($\alpha=0.01$) and c) the simulation of the current work ($\alpha=0.5$). Flow is from left to right.....	60
Figure 4-12: Contours in the X-Y plane ($Z=0$) of the non-dimensional velocity (top) and pressure (bottom) from the simulation of shock-wave induced droplet breakup. Flow is from left to right.	60
Figure 4-13: Temporal evolution of the dimensionless droplet a) velocity, b) displacement and c) acceleration, as well as d) the unsteady drag coefficient, as calculated in the current work and in the simulation of [52]......	62
Figure 4-14: Temporal evolution of droplet a) deformation in both axes (streamwise and cross-stream) and b) surface area.	62
Figure 5-1: 2-D axisymmetric domain utilized in the simulations of tandem droplet breakup ($L/D_0=2$).	66
Figure 5-2: Temporal evolution of droplet shape for chain ($We=40$, $L/D_0=2$) and isolated ($We=40$) droplets (streamlines colored with the non-dimensional relative velocity magnitude).	68
Figure 5-3: Dimensionless pressure contour for $We=40$ and $L/D_0=2$	68
Figure 5-4: Snapshot of droplet shapes for $We=40$ and $L/D_0=5$	68

Figure 5-5: Temporal evolution of droplet shape for chain ($L/D_0=2$) and isolated droplets with a) $We=20$ and b) $We=60$	69
Figure 5-6: L/D_0 - We map with the simulated cases of tandem droplet breakup, along with the regions of the various breakup regimes ($Oh=0.05$, $\varepsilon=51$ and $N=37$).....	72
Figure 5-7: Ratio $S_{max,RCD}/S_{max,is}$ as function of We and L/D_0 (scatter: CFD, lines: correlation of Table 5.2).....	73
Figure 5-8: Ratio $t_{br,RCD}/t_{br,is}$ as function of We and L/D_0 (scatter: CFD, lines: correlation of Table 5.2).	74
Figure 5-9: Ratio $Cd, RCD/Cd, is$ as function of We and L/D_0 (scatter: CFD, lines: correlation of Table 5.2).....	76
Figure 5-10: Temporal evolution of droplet velocity for two We numbers (40 and 60) and $L/D_0=2$ as predicted by the CFD simulations and the correlation (5-6).	77
Figure 5-11: Area of influence of the distance between the droplets depicted in the L/D_0 - We map along with the iso-lines of $S_{max,RCD}/S_{max,is}$, $t_{br,RCD}/t_{br,is}$, $Cd, RCD/Cd, is$ and the critical We	77
Figure 5-12: a) Actual configuration with an infinite cluster of droplets along with the computational domains and boundary conditions used in the simulations: b) 3-D-4 domain, c) 3-D-1 domain, and d) 2-D axisymmetric domain.	79
Figure 5-13: Droplet shape at the time instance of $t/t_{sh}=1$ as predicted by the simulation of a case with $We=40$ and $H/D_0=2$ using a) the 3-D-4 and b) the 3-D-1 computational domains.	80
Figure 5-14: Temporal evolution of a) cross-stream droplet deformation, b) streamwise droplet deformation, and c) droplet velocity, as calculated by a simulation with $We=40$ and $H/D_0=2$ using the three computational domains: i) 3-D-4, ii) 3-D-1 and iii) the 2-D axisymmetric.	81
Figure 5-15: Temporal evolution of droplet shape as predicted by a) the 3-D simulation and b) the 2-D axisymmetric (3-D rotation) of a droplet in a single-sheet cluster with $H/D_0=2$ and $We=40$, as well as an isolated droplet at the same We number (2-D axisymmetric). ..	82
Figure 5-16: Y-Z slices of the dimensionless a) velocity and b) pressure as predicted by the 3-D simulation of a case with $H/D_0=2$ and $We=40$ ($t/t_{sh}=0.9$).	83
Figure 5-17: Non-dimensional relative velocity contour (X-Z plane) for a case of a droplet in a cluster (3-D and 2-D axisymmetric) with $We=40$ and $H/D_0=2$, as well as an isolated droplet at the same We number.	83
Figure 5-18: Temporal evolution of droplet shape for three cases with $We=15$ and: a) $H/D_0=4$, b) $H/D_0=2$ and c) $H/D_0=1.25$	84

Figure 5-19: Dimensionless pressure contour for three cases with $We=15$ and: a) $H/D_0=4$ ($t/t_{sh}=0.7$), b) $H/D_0=2$ ($t/t_{sh}=0.6$) and c) $H/D_0=1.25$ ($t/t_{sh}=0.1$).	85
Figure 5-20: H/D_0 - We map with the simulated cases of single-sheet clusters, along with the encountered breakup regimes ($Oh=0.05$, $\varepsilon=51$ and $N=37$); the lines that separate the various breakup regimes are also presented.....	85
Figure 5-21: Ratio $S_{max,cl}/S_{max,is}$ as function of We and H/D_0 . The black line defines the region of influence of the maximum surface area of a droplet in a single-sheet cluster.....	86
Figure 5-22: Ratio $t_{br,cl}/t_{br,is}$ as function of We and H/D_0 . The black line defines the region of influence of the breakup time of a droplet a single-sheet cluster.....	87
Figure 5-23: Ratio $C_{d,cl}/C_{d,is}$ as function of We and H/D_0 . The black line defines the region of influence of the drag coefficient of a droplet a single-sheet cluster.	87
Figure 5-24: a) Actual configuration with an infinite cluster of droplets along with the computational domains and boundary conditions used in the simulations: b) 3-D-domain and c) 2-D axisymmetric domain.	88
Figure 5-25: Temporal evolution of droplet shape of the RCLD, as predicted by the 3-D simulation with $H/D_0=2$, $L/D_0=2$ and $We=40$	90
Figure 5-26: Y-Z slices of the dimensionless a) velocity and b) pressure as predicted by the 3-D simulation of a case with $H/D_0=2$, $L/D_0=2$ and $We=40$ ($t/t_{sh}=1$)......	90
Figure 5-27: Droplet shapes at $t/t_{sh}=1.3$, as predicted the 3-D simulation of a multi-sheet cluster with $H/D_0=2$, $L/D_0=2$ and $We=40$	90
Figure 5-28: Non-dimensional relative velocity contour (X-Z plane) of the RCLD as predicted by the 3-D simulations ($H/D_0=2$, $L/D_0=2$ and $We=40$)......	91
Figure 5-29: H/D_0 - We maps with the simulated cases of multi-sheet clusters (RCLD) for two streamwise droplet distances: a) $L/D_0=9$ and b) $L/D_0=1.25$ ($Oh=0.05$, $\varepsilon=51$ and $N=37$); the lines that separate the cases with breakup from those without breakup are also presented.....	92
Figure 5-30: Ratio $S_{max,RCLD}/S_{max,is}$ as function of We , H/D_0 and L/D_0	93
Figure 5-31: Ratio $t_{br,RCLD}/t_{br,is}$ as function of We , H/D_0 and L/D_0	94
Figure 5-32: Ratio $C_{d,RCLD}/C_{d,is}$ as function of We , H/D_0 and L/D_0	95
Figure 5-33: Temporal evolution of droplet shape as predicted by the 2-D axisymmetric simulation (3-D rotation) of droplets in: a) a multi-sheet cluster with $H/D_0=L/D_0=2$, b) a single-sheet cluster with $H/D_0=2$, c) tandem formation with $L/D_0=2$ and d) isolated formation ($We=40$).	96

Figure 5-34: Dimensionless pressure contour for a multi-sheet droplet cluster with $H/D_0=L/D_0=2$ and $We=40$	96
Figure 5-35: Temporal evolution of droplet velocity as predicted by the 2-D axisymmetric simulation of: a) an isolated droplet, b) the RCD ($L/D_0=2$), c) a droplet in single-sheet cluster ($H/D_0=2$) and d) the RCLD ($H/D_0=L/D_0=2$); for all cases $We=40$	97
Figure 5-36: Temporal evolution of droplet deformation in both axes of: a) an isolated droplet, b) the RCD ($L/D_0=2$), c) a droplet in single-sheet cluster ($H/D_0=2$) and d) the RCLD ($H/D_0=L/D_0=2$); for all cases $We=40$	98
Figure 5-37: Temporal evolution of surface area of: a) an isolated droplet, b) the RCD ($L/D_0=2$), c) a droplet in single-sheet cluster ($H/D_0=2$) and d) the RCLD ($H/D_0=L/D_0=2$); for all cases $We=40$	98
Figure 6-1: Definition of rim thickness and droplet radius in cylindrical coordinates.	103
Figure 6-2: Critical deformation as estimated by the CFD simulations and the experiments of [74], as well as the assumptions of the various breakup models.	111
Figure 6-3: Temporal evolution of droplet deformation as predicted by the three models (improved TAB, M-NS and unified) as well as the experimental data from the literature for a) $We=15$ and b) $We=20$	113
Figure 6-4: Temporal evolution of droplet deformation as predicted by the three models (improved TAB, M-NS and unified) along with the results of the simulations for a) $We=23$ and b) $We=60$	114
Figure 6-5: Temporal evolution of droplet deformation as predicted by the three models (improved TAB, M-NS and unified) along with the results of the simulations for two We numbers in the sheet-thinning regime (80 and 250).	114
Figure A-1: Droplet shapes at the time instance of $t/t_{sh}=2.1$ from the simulation of a chain of seven droplets arranged in tandem. $We=40$ and $L/D_0=2$	121

List of Tables

Table 1.1: Experimental studies on isolated droplet breakup at low Mach numbers.	5
Table 1.2: Previous numerical studies on isolated droplet breakup at low Mach numbers.....	6
Table 1.3: Experimental studies on isolated droplet breakup at high Mach numbers.	8
Table 1.4: Previous numerical studies on isolated droplet breakup at high Mach numbers.	9
Table 1.5: Experimental studies on cluster droplet breakup.	10
Table 1.6: Numerical studies on cluster droplet breakup.....	11
Table 1.7: Summary of empirical correlations for droplet deformation.	13
Table 1.8: Summary of theoretical and semi-analytical models for droplet breakup.	16
Table 3.1: Properties of liquid Diesel at $T=293.15\text{K}$ and $P=1\text{bar}$ based on [18].	33
Table 3.2: Examined cases for the validation of the low Ma number droplet breakup model.	33
Table 3.3: Droplet diameter and non-dimensional numbers for the 2-D simulation of droplet breakup at high Ma number.	42
Table 4.1: Examined cases for the parametric study of isolated droplet breakup.	47
Table 4.2: Droplet diameter and non-dimensional numbers of the 3-D simulation of droplet breakup at high Ma number.	58
Table 5.1: Representative Diesel engine conditions.	65
Table 5.2: Summary of proposed correlations.....	70
Table 5.3: Drag coefficients of an isolated droplet, the RCD, a droplet in a single-sheet cluster and the RCLD ($We=40$).	97
Table 6.1: Parameters of the original and improved TAB models.	102
Table 6.2: Parameters of the bag-NS and M-NS models.....	106
Table 6.3: Parameters of the unified secondary breakup model to match the various models of the literature.	110
Table 6.4: Examined cases for comparison with the analytical models.....	112

Acknowledgements

First of all, I would like to thank prof. Manolis Gavaises for giving me the opportunity to enroll as a PhD student and come true of one of my goals in life. As early as an undergraduate student I had the desire to perform research and be part of the academia. Probably, I was not determined enough to start a PhD at that time, something that occurred a few years later. Prof. M. Gavaises gave me the opportunity to promote my work and meet interesting people and places through conferences, workshops and project meetings around the world. In addition, he provided a critical review and guidance throughout my thesis and urged me to become better and look at my work from a different perspective.

Secondly, I would like to express my gratitude for Dr. Nikolaos Nikolopoulos for letting me be part of his research team at the Center for Research and Technology Hellas (CERTH) and providing me with the necessary tools and knowledge to perform my research. His managerial skills, persistence and time investment made it possible to perform good quality work withing the given time.

Furthermore, I would like to thank my daily supervisors and members of the CERTH team prof. George Strotos and Dr. Ilias Malgarinos. Both of them transferred their deep knowledge in CFD as well as in scientific writing. In addition, they helped me set realistic short terms goals and overcome obstacles on personal level. My special thanks also to Dr. Foivos Koukouvinis who co-supervised me and helped with my research during my two-month stay at the City University.

My sincere thanks to my colleagues at CERTH and City University as well as my fellows from the HAoS project Stavros Fostiropoulos, Myrtw Zeneli, Theodoros Lyras, Konstantinos Kolovos, Akis Papakonstantinou, Georgia Nukteri, Nikos Bempedelis, Daniel Loureiro and Nikos Chatziarsenis, who helped me both on personal and scientific level.

I will never forget the support from my parents, Despina Tsipi and Gerasimos Stefanitsis, my sister, Anna Stefanitsi, as well as my close friends who helped me overcome psychological barriers and urged me to continue my research.

Finally, I would like to acknowledge the Marie Curie ITN-ETN project HAoS, which provided financial support for my research as well as the opportunity to travel and collaborate with fascinating people. Without its support this journey, which made me a better person both scientifically and personally, would not have been possible.

London, March 2020

Dipl MEng, MSc, Stefanitsis Dionysios

Declaration

I hereby declare that the contents of this dissertation are original and have not been submitted in whole or in part for consideration for any other degree or qualification in this, or any other university. This dissertation is my own work, except where specific reference is made to a joint effort in the text and Acknowledgements accordingly.

I grant powers of discretion to the University Librarian to allow the thesis to be copied in whole or in part without further reference to me. This permission covers only single copies made for study purposes, subject to normal conditions of acknowledgement.

London, March 2020

Dipl MEng, MSc, Stefanitsis Dionysios

Abstract

The current work investigates numerically the breakup of isolated droplets and droplet clusters in representative engine conditions. A CFD model in the commercial software ANSYS FLUENT is utilized to perform 3-D and 2-D axisymmetric simulations, which solves the laminar Navier-Stokes equations coupled with the conservation of the volume fraction. In cases with high Mach (Ma) numbers the energy equation is solved as well, along with two equations of state (EoS) to predict the density variations of the two fluids; in addition, a coupled VOF/Lagrange model is employed to capture the appearance of micro-droplets.

The CFD model is validated against experimental data for the breakup of isolated droplets at Weber (We) numbers ranging from 14 up to 254, density ratios (ϵ) from 79 up to 695, Ma numbers from less than 0.1 up to 1.47 and Ohnesorge (Oh) numbers below 0.1. The validated model is utilized initially to perform a parametric study with isolated Diesel and heavy fuel oil droplets at We numbers ranging from 14 up to 254, Oh numbers from 0.011 up to 1.525, density ratios from 72 up to 816 and $Ma < 0.1$. Conclusions are drawn about the effect of ϵ and Oh on the breakup process, and based on the results correlations are proposed to predict key droplet quantities, such as the breakup time, drag coefficient and surface area, as function of the non-dimensional numbers (We , Oh , ϵ).

As a next step, simulations are performed with droplet clusters, which are more representative of the conditions encountered in fuel sprays, in which droplet proximity becomes relevant. Initially, a chain of four droplets in tandem formation is examined, which represents an “infinite” array of droplets, next, a configuration with an infinite “sheet” of droplets moving in parallel to the air flow, and finally, a combination of the two, in which four droplet “sheets” are moving in parallel to the flow. The simulations are performed at We numbers ranging from 15 up to 64 and non-dimensional streamwise (L/D_0) and cross-stream (H/D_0) distances between the droplets in the range of 1.5 up to 20. A new breakup mode is identified, termed as “shuttlecock”, which is characterized by an oblique peripheral stretching of the droplet and is encountered at droplet distances $L/D_0 \leq 5$ and $H/D_0 \leq 5$. In addition, the effect of L/D_0 and H/D_0 is investigated on droplet quantities, such the critical We number (breakup map), breakup time and drag coefficient, and correlations are provided to predict these quantities as function of We and L/D_0 , for droplets in tandem formation. These correlations along with a developed new analytical droplet deformation and breakup model (unified secondary breakup model) can be utilized in Eulerian-Lagrangian CFD codes simulating the development of sprays consisting of millions of droplets.

Thesis Contribution

The simulations of the current work contributed to the following:

- **Development of new breakup maps for droplets in cluster formations:** the limits of the various breakup modes (bag, multi-mode and shuttlecock) are presented, for the first time, for droplets in cluster formations as function of the Weber (We) number, the non-dimensional streamwise distance between the droplets (L/D_0) as well as the cross-stream one (H/D_0). The maps have been developed based on the results of a series of 2-D axisymmetric and 3-D simulations utilizing a CFD model that solves the laminar incompressible Navier-Stokes equations coupled with the volume of fluid method (VOF) for capturing the interface between the liquid droplet and the surrounding gas. The examined cluster formations are: i) four droplets in tandem (i.e. one behind the other), ii) an infinite sheet of droplets moving in parallel to the gas flow, and iii) a combination of the two, in which four droplet sheets are moving in parallel to the air flow. The examined non-dimensional numbers are: $We=10-64$, $L/D_0=1.25-20$, $H/D_0=1.25-20$, Ohnesorge number (Oh) equal to 0.05 and density ratio (ϵ) equal to 51. The new maps present a more accurate categorization of the various breakup modes encountered in fuel sprays, in which the droplets are influenced by the presence of surrounding droplets, as compared to the existing ones, which have been developed for isolated droplets.
- **Identification of a new breakup mode:** based on the aforementioned simulations a new breakup mode has been identified, termed as shuttlecock, which is characterized by an oblique peripheral stretching of the droplet and is encountered in droplet clusters at distances $L/D_0 \leq 5$ and $H/D_0 \leq 5$.
- **Development of new correlations for the prediction of integral droplet parameters:** for the first time, to the authors best of knowledge, correlations are proposed for predicting integral parameters of droplets in cluster

formations, such as the drag coefficient, surface area and breakup time, as function of the non-dimensional numbers (We , Oh , ε , L/D_0). These correlations can be utilized in Eulerian-Lagrangian codes for the modeling of sprays consisting of millions of droplets, providing a better estimation of the parameters compared to the existing correlations, which have been derived for isolated droplets.

- **Development of a new analytical droplet deformation and breakup model:** a new 0-dimensional deformation and breakup model has been developed for isolated droplets, termed as unified secondary breakup model, which incorporates various existing models of the literature (TAB, DDB, NLTAB and NS) with the use of adjustable coefficients. The new model is capable of predicting the droplet deformation in all the three main breakup modes: i) bag ($We=10-20$), ii) multi-mode ($We=21-65$), and iii) sheet-thinning ($We=66-350$), and can be utilized in Eulerian-Lagrangian codes for the modeling of sprays, providing a wider range of applicable conditions compared to the existing ones.

Nomenclature

Latin characters

Symbol	Description	Unit
A_f	Droplet frontal area	m^2
B	Average dimensionless deformation rate	-
C_d	Drag or viscosity coefficient	-
C_F	Pressure coefficient	-
C_k	Surface tension coefficient	-
CF	Correction factor	-
Cou	Courant number	-
c	Speed of sound	m/s
D	Droplet diameter	m
E	Energy	J
F_{vol}	Volumetric force	N
f	Frequency	Hz
H	Cross-stream droplet distance	m
h	Specific enthalpy or rim thickness	j/kg or m
K	Bulk modulus	N/m^2
L	Streamwise droplet distance or distance travelled	m
m	Mass	kg
Ma	Mach number	-
MW	Molecular Weight	-
N	Viscosity ratio	-
\vec{n}	Free-surface unit normal	-
Oh	Ohnesorge number	-
P or p	Pressure	P
R or r	Droplet radius	m
Re	Reynolds number	-
S	Surface area	m^2
St	Strouhal Number	-

T	Temperature	K
t	Time	s
t_{br}	Breakup initiation time	s
t_{sh}	Shear breakup timescale	-
U or u	Velocity	m/s
V	Volume	m ³
W	Work	J
We	Weber number	m/s
x	Droplet displacement	m
y	Non-dimensional deformation	-

Greek characters

Symbol	Description	Unit
α	Volume fraction or rate of stretching indicator	-
δx	Leading-edge displacement	m
ε	Density ratio	-
κ	Curvature	1/m
μ	Dynamic viscosity	Pa·s
ρ	Density	Kg/m ³
σ	Surface tension coefficient	N/m
τ_r	Droplet relaxation time	s
ϕ	Schlieren function or integral droplet parameter	-

Superscripts and subscripts

Symbol	Description
*	Non-dimensional
∞	Infinite
cell	Computational cell
cl	Cluster
cm	Center of mass
cr	Cross-stream or critical
d	Droplet
def	Deformation
g	Gas
is	Isolated
kin	Kinetic
L or l	Liquid
mag	Magnitude
max	Maximum
o	Initial
press	Pressure
r	Radial
ref	Reference
rel	Relative
sh	Post-shock quantity
str	Streamwise
surf	Surface
viss	Viscous

Abbreviations

Symbol	Description
BTB	Bag-Type Breakup
CFD	Computational Fluid Dynamics
CpR	Cells per Radius
DDB	Droplet Deformation and Breakup model
DMTAB	Double Mass TAB
DNS	Direct Numerical Simulation
DPM	Discrete Phase Model
EoS	Equation of State
EV	Electric vehicles
FIE	Fuel Injection Equipment
FV	Finite Volume
HFO	Heavy Fuel Oil
IC	Internal Combustion
K-H	Kelvin-Helmholtz
LS	Level-Set
M-NS	Modified model based on the Navier-Stokes
NLTAB	Non-Linear TAB
NS	Navier-Stokes
R-T	Rayleigh-Taylor
RCD	Representative Chain Droplet
RCLD	Representative Cluster Droplet
RTP	Rayleigh-Taylor Piercing
SGS	Sub-Grid-Scale
SIE	Shear-Induced Entrainment
TAB	Taylor Analogy Breakup
VOF	Volume of Fluid
CLSVOF	Coupled Level-Set VOF
CSS	Continuum Surface Stress
UDF	User-Defined Function

Chapter 1

Introduction

1.1 Background and Motivation

1.1.1 Motivation

Global energy demand is expected to increase by ~20% up to 2040 [1], mainly due to increasing population and prosperity, especially in the non-OECD countries. Although renewable energy sources are going to play a key role in covering the extra demand, oil and natural gas will continue to supply more than 50% of the global energy [1]. This implies that in order to meet the target of 2°C of the Paris Agreement [2], innovative technology solutions and supportive policies are still needed, despite the increased energy efficiency and shifting to lower carbon energy sources [1]. One sector that plays a significant role in the global energy consumption is the transportation, which accounts for approximately 21-25% of the global energy consumption and ~25% of the global energy related greenhouse gas emissions [1]. Moreover, the demand for energy in the transportation sector is expected to increase by 25% by 2040 [1], mainly due to increased commercial activity (heavy-duty, aviation, marine and rail engines), as also due to personal vehicle ownership (light duty engines) as purchasing power rises. Despite the increase of electrical vehicles (EV), internal combustion (IC) engines will remain predominant for transportation (~92.5% for light duty and ~81% for heavy duty) [1], since the EVs require the use of batteries, which have a significant cost, weight and other limitations [3]. In spite of the 1000-fold decrease in the pollutant levels of IC engines in the past decades, there is still room for improvement with the development of a fuel injection equipment (FIE) able to reduce pollutant emissions from liquid-fueled transportation.

However, this is a challenging task since during the injection of fuel in internal combustion engines various complex multi-phase phenomena occur, as illustrated in Figure 1-1. Initially, cavitation may take place inside the nozzle, which is responsible for the creation of vapor bubbles influencing the atomization of the liquid at the nozzle exit. Following that, the dense liquid zone forms fragments, which are gradually disintegrated into smaller droplets due to their aerodynamic interaction with the ambient air (primary atomization). These droplets move with high velocities resulting in their further breakup downstream, creating the final dilute stage or cloud of the spray (secondary atomization or droplet breakup). This fuel cloud first evaporates and eventually combusts providing the required power of the engine.

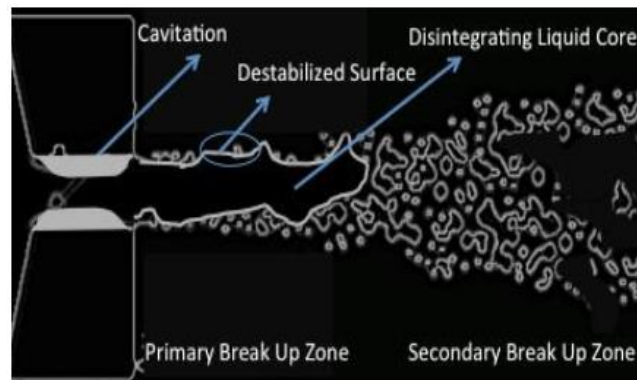


Figure 1-1: Physical phenomena in fuel injection equipment.

The aforementioned phenomena occur at different time and length scales, making it prohibitive to perform direct numerical simulations (DNS) for the whole spray. As a compromise, computational fluid dynamics (CFD) models that utilize closure sub-grid-scale (SGS) models aiming to resolve the smaller scales are widely used. The current work focuses on the secondary droplet breakup, in which variables such as the droplet surface area, drag coefficient, and breakup initiation time are of utmost importance for the development of the SGS models. The goal of the current work is to improve the existing as well as to develop new SGS models, which will include the dependence of the aforementioned variables on the non-dimensional numbers (see section 1.1.2) for various droplet arrangements representative of fuel sprays.

An extensive literature review is performed to record the existing work on the subject of droplet breakup in fuel sprays as well as to identify gaps in the literature and possible advancements.

1.1.2 Non-dimensional numbers

Before proceeding further, it is useful to define the non-dimensional numbers that are important in the secondary atomization, since most of the studies, including this one, use non-dimensional numbers to describe the phenomenon. The relative velocity between the liquid droplet and the surrounding gas is responsible for the aerodynamic forces that tend to deform the droplet, while fluid properties such as viscosity and surface tension induce forces that resist deformation. The most important non-dimensional numbers controlling the aerodynamic droplet breakup are the Weber (We), the Ohnesorge (Oh) and the Reynolds (Re) numbers as well as the density (ε) and viscosity (N) ratios of the two phases [4]. In addition, in flows where the velocity is comparable to the speed of sound the Mach (Ma) number is utilized as well.

$$\begin{aligned}
 We &= \frac{\rho_g U_0^2 D_0}{\sigma} & Oh &= \frac{\mu_L}{\sqrt{\rho_L \sigma D_0}} & Re &= \frac{\rho_g U_0 D_0}{\mu_g} \\
 Ma &= \frac{U_0}{c} & \varepsilon &= \frac{\rho_L}{\rho_g} & N &= \frac{\mu_L}{\mu_g}
 \end{aligned} \tag{1-1}$$

As the breakup process is not instantaneous, the breakup timescale proposed by Nicholls and Ranger [5] can be used as a convenient non-dimensionalisation parameter for understanding the temporal development of the process ($t^*=t/t_{sh}$):

$$t_{sh} = \frac{D_0}{U_{rel,0}} \sqrt{\varepsilon} \tag{1-2}$$

However, in some spray application, such as those of Diesel engines, the droplets are influenced by the presence of other droplets in their proximity. For example, a typical Diesel spray consists of $\sim 10^7$ droplets, occupying a volume of $\sim 250 \text{mm}^3$ [6]; assuming an average droplet size of $10 \mu\text{m}$ [6, 7], the average distance between the droplets can be estimated to be around $2.5 D_0$ but obviously this number will take smaller values closer to the injector nozzle [8]. In these cluster formations the non-dimensional streamwise (L/D_0) and cross-stream (H/D_0) distances between the droplets can be speculated to play a role; the L and H here correspond to distances between the droplet centers.

1.1.3 Breakup modes

It is generally considered [4] that when the Oh number is less than 0.1 and the Ma number is low the droplet breakup is mostly influenced by the We number and based on it five breakup modes are identified as shown in Figure 1-2.

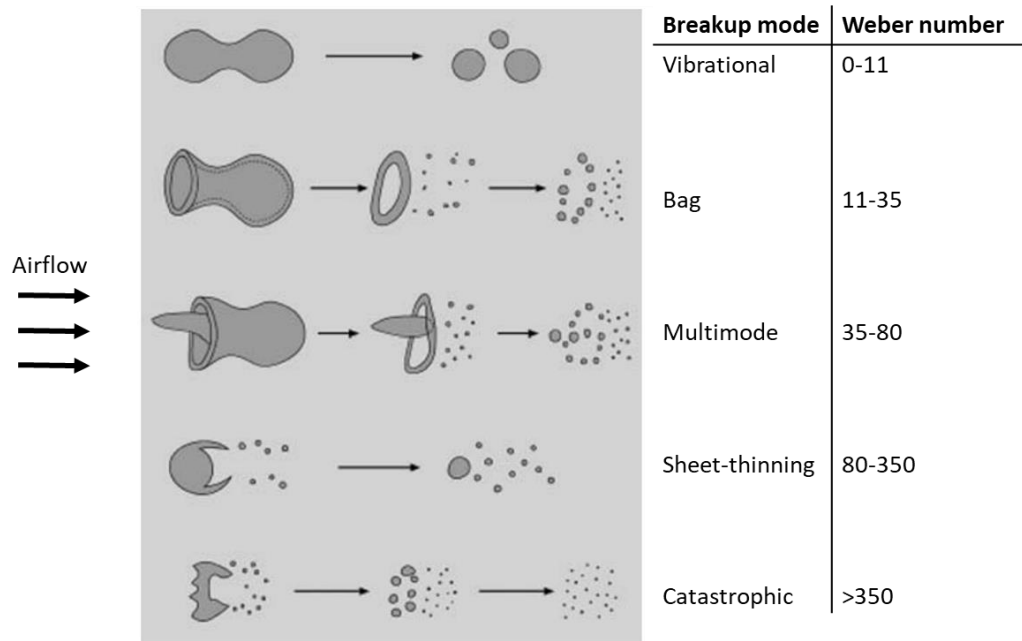


Figure 1-2: Breakup modes as function of the We number [4].

During the vibrational mode ($We < 11$), the droplet oscillates between its initial spherical shape and that of an oblate spheroid. If these oscillations become unstable the droplet breaks into a few smaller fragments. The second breakup mode is called bag breakup ($11 < We < 35$), owing its name to the bag resembling shape that the drop takes during its deformation. As the We number is further increased up to 80 the multimode breakup regime is encountered, which is an intermediate stage between the bag and sheet-thinning breakup modes. In this regime different droplet shapes are encountered with the most dominant ones being the bag-stamen, the dual bag and the plume/shear. During the sheet-thinning breakup mode ($80 < We < 350$) a liquid sheet is formed at the droplet periphery, which initially breaks into ligaments and eventually into small fragments. The final breakup mode ($We > 350$) is called catastrophic and is attributed to instabilities such as the Rayleigh-Taylor (R-T) and Kelvin-Helmholtz (K-H). These instabilities create unstable waves on the leading surface of the droplet, which grow in time and eventually lead to the breakup of the droplet. However, the existence of the

catastrophic regime has been questioned and is attributed to artifacts of the shadowgraphs, while shear-induced entrainment (SIE) mode is believed to occur instead ($We > 1000$) [9, 10]. In addition, for supersonic flows ($Ma > 1$) the Rayleigh-Taylor piercing (RTP) breakup mode is encountered for We in the range of 10-100 [10]. The RTP and SIE breakup modes are attributed to RT and KH instabilities, respectively.

1.2 Literature review

1.2.1 Isolated droplet breakup

1.2.1.1 Breakup at low Mach numbers

Table 1.1 summarizes the experimental studies of the literature regarding the breakup of isolated droplets at low Mach numbers, while Table 1.2 presents the previous numerical studies. It is evident from the tables that although a wide range of non-dimensional numbers has already been examined there is a gap in the literature regarding the specific conditions encountered in Diesel engines operating with Diesel and heavy fuel oil (HFO) as fuels, which are characterized by low ϵ and high Oh numbers (see Figure 1-6 in section 1.3).

Table 1.1: Experimental studies on isolated droplet breakup at low Mach numbers.

Study	Liquids	Non-dimensional numbers	Breakup regimes	Main outcomes
Hinze [11]	Gas oil	$We=13-40$, $Oh=0.01-2$	Bag, multi-mode	Rate of droplet deformation decreases with increasing Oh . For $Oh > 2$ no breakup occurs for the examined conditions.
Hanson et al. [12]	Water, methyl-alcohol, silicon oil	$We=3.6-23.8$, $Re=317-946$	Bag, multi-mode	The air shock wave itself is not the cause of breakup, but rather the air flow stream induced behind it. For $\mu_L > 10\text{mPa}$ the liquid viscosity affects the critical breakup velocity (minimum velocity required for breakup).
Gel'fan d et al. [13]	Water and glycerine	$We=5-25$	-	Empirical correlations for: i) the minimum We number required for breakup, ii) the breakup initiation time, and, iii) the total breakup time as a function of the Laplace number ($La=1/Oh^2$).
Arcoum anis et al. [14]	Diesel, water, non	$We=14-10000$, $Oh=0.027$ and 0.059	Bag, multi-mode, sheet-	Non-dimensional breakup time reaches a constant value of ~ 5.5 for $We=2670-6000$, while it increases for $We=6000-10000$.

	Newtonian fluids		thinning, catastrophic	
Hsiang and Faeth [15-17]	Water, glycerol, n-heptane, ethyl alcohol, mercury	$We=0.5-600$, $Oh<560$, $Re>300$, $\epsilon>580$	Deformation, bag, multi-mode, sheet-thinning	Combined their results with previous studies to construct an $Oh-We$ map where the various breakup regimes are presented. For $Oh>1$ the critical We number for the onset of breakup is roughly proportional to Oh . For $Oh>0.1$ the breakup time for the examined conditions increases with the increase of Oh .
Reitz and co-workers [18-20]	Diesel and water	$We=56-532$, $Re=509-8088$, $\epsilon=79-700$, $Oh<0.065$	Bag, multi-mode, sheet-thinning, catastrophic	Re number does not affect the breakup process, but rather the We number is the controlling parameter. Sheet-thinning breakup regime (formerly known as shear stripping) is not due to viscous stresses but rather due to aerodynamic forces.
Lee and co-workers [21, 22]	Diesel and bio-diesel	$We=4.3-383$	Bag, multi-mode, sheet-thinning, catastrophic	TAB and droplet drag models were modified, as well as a new model was suggested for determining the droplet size after breakup.
Zhao and co-workers [23-25]	Water, ethanol, glycerol	$We=9.4-49$, $Oh=0.0018-0.36$	Bag and bag-stamen	Correlation for the prediction of the critical We number as function of the Oh number, based on the Rayleigh-Taylor instability. The maximum droplet deformation decreases with increasing Oh number, while the mean diameter of the fragments increases.

Table 1.2: Previous numerical studies on isolated droplet breakup at low Mach numbers.

Study	Non-dimensional numbers	Breakup regimes	Numerical methods	Dimensions	Main outcomes
Han and Tryggvason [26]	$We=3.74-93.5$, $Oh<15.8$, $\epsilon=1.15$ and 10 , $Re=60.5-387$	Deformation, bag, multi-mode	Finite difference /front tracking	2-D axisymmetric	The increase of Oh number leads to the decrease of the rate of deformation and the alternation of the droplet shape from forward-facing bag to oblate.
Aalburg [27]	$Re=25-200$, $\epsilon=2-32$, $Oh=0.001-100$	Deformation	Level Set (LS)	2-D axisymmetric	By decreasing ϵ below 32, the We_{cr} increases. For $\epsilon>32$ the breakup outcome is independent of ϵ .
Quan and Schmidt [28]	$We=0.4-40$, $Oh=1.12$ and 2.24 , $\epsilon=10-50$	Deformation	Finite volume, staggered mesh	3-D	The increase of Oh number results in lower deformation and C_d .

Wadhwa et al. [7]	$We=1-100$, $Oh=0.001-0.1$, $\varepsilon=50$, $Re=150$	-	Hybrid compressible-incompressible	2-D axisymmetric	Droplet deformation and drag increase with decreasing Oh number.
Jing and Xu [29]	$We=2.7-275$, $Oh=0.0008-0.831$, $\varepsilon=10-100$	Deformation, bag, sheet-thinning	SIMPLER method, Level set	2-D axisymmetric	Increase of Oh number can result in no breakup.
Kekesi et al. [30]	$We=0.1-20$, $Oh=0.007-1$, $\varepsilon=20-80$, $Re=20-200$	Bag and sheet-thinning	VOF, staggered grid	3-D	Developed a new breakup map in the $Re-N/\sqrt{\varepsilon}$ plane, where the different breakup regimes were presented. They identified 5 new breakup modes (jellyfish shear, thick rim shear, thick rim bag, rim shear and mixed) in the bag breakup regime.
Yang et al. [31, 32]	$We=8-225$, $Oh=0.001-2$, $\varepsilon=10-800$	Bag, multi-mode, sheet-thinning	Coupled LS-VOF	3-D	Theoretical model based on the R-T instability for predicting the We_{cr} . C_d and drop deformation are affected by ε even when it exceeds the value of 32, as opposed to the findings of [27].
Shao et al. [33]	$We=1-10$, $Oh=0.0007-0.1$, $\varepsilon=6.25-40$	-	LS	3-D	The unsteady drag coefficient is influenced mostly by ε , while the change in Oh number has a small effect

1.2.1.2 Breakup at high Mach numbers

Apart from the non-dimensional numbers mentioned in the previous section (We , Oh , ε and Re) another number that plays a key role in the cases where the speed of air is comparable to the speed of sound is the Mach number. Table 1.3 presents the experimental studies on isolated droplet breakup at high Ma numbers, while Table 1.4 illustrates the previous numerical studies. It is interesting to note that different breakup modes than those of section 1.2.1.1 are encountered at high Ma numbers, even for low We numbers (see [10, 34]). The most common are the shear induced entrainment (SIE) ($We > 1000$) and the Rayleigh–Taylor piercing (RTP) ($We = 10-100$), which are dominated by KH and RT instabilities, respectively. On the other hand, bag and bag-and-stamen breakup modes are also encountered but at higher We numbers compared to supersonic flows (see [35-37]). Although some efforts have been made to identify the boundaries of the breakup regimes at high Ma numbers [10, 34-37] more data are needed to create a map similar to that of [38], which will include also the effect of Ma , especially for the transonic region which is relatively unexplored.

Table 1.3: Experimental studies on isolated droplet breakup at high Mach numbers.

Study	Liquids	Non-dimensional numbers	Breakup regimes	Main outcomes
Engel [39]	Water	$Ma=1.3-1.7$	-	Formation of a mist at the periphery of the droplet. Measurement of its breakup time.
Boiko and co-workers [40, 41]	Water, alcohol, glycerine, tridecane	$Ma=0.15-4$, $We>400$	-	The disintegration of the droplets originates from their surface (core or periphery) and it is attributed to RT and KH instabilities
Takaya ma and co-workers [42, 43]	Water	$Ma=1.3-1.56$, $We=600-760$	Stripping (later named as SIE)	Breakup process is divided into four stages: i) disruption of the liquid surface, ii) droplet deformation and initiation of the formation of micro-droplets, iii) continuous stripping of micro-droplets, and iv) parent droplet breaks into large fragments.
Joseph and coworkers [36, 37]	Newtonian and viscoelastic	$Ma=2-3.03$, $We=11700-169000$, $Oh=0.002-82.3$	Bag and bag-and-stamen breakup	Developed a simplified theory to predict the critical wave length and growth rate of the RT instabilities.
Theofanous and coworkers [10, 34]	Water and viscous liquids (silicon oil, glycerol, tri-butyl phosphate)	$Ma=1.1-3.5$, $We=12-2 \cdot 10^5$, $Oh=0.0012-540$	Shear induced entrainment (SIE), Rayleigh–Taylor piercing (RTP)	At $We >1000$ SIE occurs instead of RTP ($We=10-100$). Catastrophic breakup regime is a mirage of the shadowgraph technique. K-H instabilities play an important role in the breakup of viscous liquids.
Yi et al. [44]	Water	$Ma=1.39-1.90$, $We=10^3-10^4$	-	Two mechanisms are responsible for the droplet deformation at the early-stages: i) pressure and ii) shear mechanisms.
Engel [39]	Water	$Ma=1.3-1.7$	-	Formation of a mist at the periphery of the droplet. Measurement of its breakup time.
Boiko and co-workers [40, 41]	Water, alcohol, glycerine, tridecane	$Ma=0.15-4$, $We>400$	-	The disintegration of the droplets originates from their surface (core or periphery) and it is attributed to Taylor and KH instabilities.
Hebert et al. [45]	Water	$Ma=4.2-4.6$, $We>10^5$	Catastrophic	Performed both experiments and numerical simulations in two dimensions using an in-house code called Hesione. The breakup mechanism was divided in 3 steps: i) droplet flattening, ii) fragmentation initiation at the outer rim of the droplet, and iii) droplet takes the shape of a filament aligned with the flow.

Table 1.4: Previous numerical studies on isolated droplet breakup at high Mach numbers.

Study	Non-dimensional numbers	Breakup regimes	Numerical methods	Dimensions	Main outcomes
Surov [46]	$Ma=3-10$	-	Godunov's and MAC methods [47], ideal gas law, incompressible liquid	2-D axisymmetric	An increase in droplet viscosity leads to a slight decrease in its rate of deformation. Liquid density affects substantially the droplet deformation and displacement.
Chang and coworkers [48, 49]	$Ma=0.29-3$, $We=520 - 5.4 \cdot 10^4$, $Oh < 1.9$	RTP and SIE	AUM+-scheme [50], stiffened-gas EoS for both phases	2-D axisymmetric	Attributed the SIE breakup mode to K-H instabilities and the RTP to RT instabilities, similar to [10, 34]
Xiao et al. [35]	$Ma=3$, $\varepsilon=18544-667577$, $We=15-75$	Bag, multi-mode	Ghost fluid method, CLSVOF, compressible gas, incompressible liquid	3-D	The We numbers separating the different breakup modes, as well as the breakup initiation time, are higher in supersonic flows compared to subsonic ones.
Guan et al. [51]	$Ma=1.39-3.9$ and We in the order of 10^3	-	Five equation model (compressible Euler equations) coupled with the stiffened gas EoS	2-D axisymmetric	Identified a saddle point (point of zero velocity) inside the droplet and proposed a model to predict it as a function of the Ma number.
Meng and Colonius [52, 53]	$Ma=1.47$, $We=780$	SIE	Five equation model coupled with the stiffened gas EoS	3-D	Disintegration of the droplet into two liquid sheets, in agreement with [18].
Kaiser et al. [54]	$Ma=1.47$, $We=780$	SIE	LS, five equation model	2-D planar and 3-D	Confirmed the results of [52, 53] for the existence of two liquid sheets during breakup, and also observed a third one.
Liu et al. [55]	$Ma=1.2-1.8$	SIE	Five equation model coupled with the	3-D	Defined three stages of the breakup process in the SIE regime: i) surface instability, ii) droplet flattening, and iii)

			stiffened gas EoS		entrainment from the liquid sheet.
Surov [46]	$Ma=3-10$	-	Godunov's and MAC methods [47], ideal gas law, incompressible liquid	2-D axisymmetric	An increase in droplet viscosity leads to a slight decrease in its rate of deformation. Liquid density affects substantially the droplet deformation and displacement.

1.2.2 Cluster droplet breakup

The aforementioned studies so far refer to isolated droplets, i.e. droplet that are not influenced by the presence of surrounding droplets. Regarding the droplets in cluster formations, Table 1.5 presents the experimental studies of the literature with droplet clusters, while Table 1.4 presents the previous numerical studies. Most of the studies examined either tandem or parallel configurations and only a few of them examined different angles [56, 57], and then only with two droplets. However, in realistic fuel sprays multiple droplets exist in cluster configurations, in which the droplets are influenced by the simultaneous presence of other droplets in both the vertical and horizontal directions; this is something that has not been investigated before and is one of the focuses of the current work.

Table 1.5: Experimental studies on cluster droplet breakup.

Study	Nr. of droplets	Configuration	Non-dimensional numbers	Main outcomes
Liu et al. [58]	Stream	Tandem	$Re=20-100$, $L/D_0=2-12$	C_d of droplet in an infinite chain ($L/D_0=2$) is up to an order of magnitude smaller than the C_d of an isolated droplet.
Mulholland et al. [59]	Stream	Tandem	$Re=90-290$, $L/D_0=1.7-1700$	Empirical model for the computation of C_d , which was able to predict the droplet trajectories with acceptable accuracy.
Temkin and Ecker [60]	2	Tandem, parallel	$Re < 150$, $H/D_0=1.5-11$, $L/D_0=3-6$	The leading droplet is not affected by the trailing in terms of drag force, while the latter experiences reduction in its C_d up to 50% relative to its isolated value. The wake of a droplet affects the drag coefficient of the trailing droplets that lie within a parabolic shape of $15D_0$ length and $1D_0$ width.
Poo and Ashgriz [61]	Stream	Tandem	$Re=17500$ and 27700 , $L/D_0=2.92-4.26$	A decrease in the C_d by a factor of 4 to 5 compared to the C_d of a solid sphere at the same conditions.

Nguyen and Dunn-Rankin [62]	Droplet packets (1-6)	Tandem	$Re=80$, $L/D_0=5.2$	The average drag of the trailing droplet was 25% lower than that of the leading one.
Connon and Dunn-Rankin [63]	Droplet packets (1-10)	Tandem	$Re=77-102$, $L/D_0=2.7-4.8$	An infinite stream influences its surrounding at a horizontal distance of 15 diameters away.
Hollander and Zaripov [64]	Stream	Tandem	$Re=1-10$	Correction for the C_d in the droplet momentum equation, so that the presence of other droplets are taken into account .
Zhao et al. [65]	2	Tandem up to parallel	$Re=2680$, $We=12.3$, $L/D_0<3$, $H/D_0<3$	Identified four breakup modes: i) coalescence, ii) puncture, iii) side-by-side and iv) no direct contact. Fastest mode is the side-by-side, in which the droplets deform into a disk-like shape with their edges touching before the breakup occurs (encountered for $H/D_0\leq 2$).

Table 1.6: Numerical studies on cluster droplet breakup.

Study	Nr. of droplets	Configuration	Non-dimensional numbers	Numerical methods	Dimensions	Main outcomes
Kim et al. [66-68]	2	Parallel	$Re=50-150$, $H/D_0=1.5-25$	Implicit finite difference	3-D	For $H/D_0<9$ the C_d of the droplets is higher than that of an isolated droplet at the same conditions.
Prahl et al. [56]	2	Tandem up to parallel	$Re=100$, $We=0.1$ and 1, $L/D_0=1.5-6$, $H/D_0=1.5$	VOF	3-D	In the parallel arrangement the droplets experience higher drag force compared to the isolated droplet and also a weak attraction.
Quan et al. [69, 70]	2	Tandem	$We=0.4-40$, $Oh=0.1-1.1$, $Re=40$, $\varepsilon=50$, $L/D_0=1.3-6$	FV, moving mesh interface tracking scheme	3-D	The C_d of the trailing droplet is greatly reduced, while that of the leading is less affected, compared to that of the isolated droplet.
Magi and Abraham [71]	2, 4	Tandem	$\varepsilon=5$, $N=5$, $Oh=0.025$, $We=20$ and 50, $L/D_0=1.5$	Lattice-Boltzmann	2-D axisymmetric	For the case of 4 droplets the two trailing ones decelerate slower than the isolated one. The leading droplet breaks up faster than the rest followed by the middle one.
Kekesi et al. [57]	2	Tandem up to parallel	$We=20$, $Re=20$ and 50, $L/D_0=1.5-5$, $H/D_0=1.5-5$	VOF	3-D	Three scenarios were identified for the breakup of the droplets: i) they collide and merge, ii) the secondary drop shoots through the primary drop and iii) the two drops behave independently. For certain parallel configurations the breakup

time is shorter than that of an isolated droplet. This was attributed to the increased velocity in the gap between the droplets, which results in enhanced shear at the droplet periphery.

1.2.3 Analytical models for droplet deformation and breakup

The prediction of the temporal evolution of droplet deformation is an important aspect that is utilized in CFD spray codes following the Lagrangian approach [72]. The droplet deformation is usually qualitatively described by the cross-stream droplet diameter, as shown in Figure 1-3, and various models have been developed for its estimation as a function of time, based both on experimental and theoretical works, as described in the following sections.

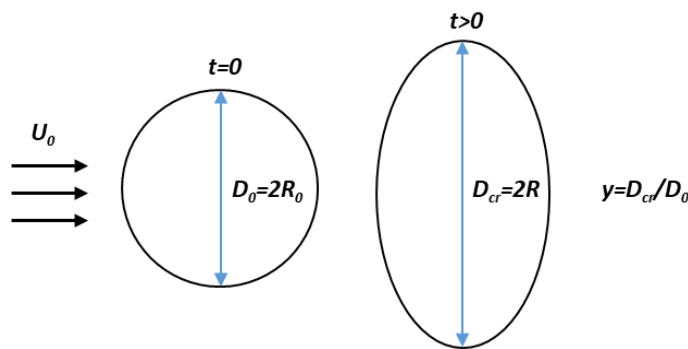


Figure 1-3: Definition of the cross-stream droplet diameter and the non-dimensional droplet deformation.

1.2.3.1 Empirical models

Various studies in the literature conducted experiments of aerodynamic droplet breakup and based on their results they proposed empirical correlations for the prediction of the droplet deformation as a function of the non-dimensional time (t^*). These correlations can be written in the general form of $y = c_0 + c_1(t^*)^{c_2} + c_3(t^*)^2$, where the coefficients c_0 , c_1 , c_2 and c_3 are summarized for each study in Table 1.7, along with their range and conditions of applicability.

Table 1.7: Summary of empirical correlations for droplet deformation.

Study	General equation: $y=c_0+c_1(t^*)^{c_2}+c_3(t^*)^2$				Conditions of applicability*1		
	c_0	c_1	c_2	c_3	Non-dimensional numbers	Breakup mode	Time range
Gel'fand et al. [73]	1	$1 - \frac{We}{We_{cr}}$	1	0	$We=24-180$	Bag, multi-mode, sheet-thinning	$t^* \leq 1.5$
Hsiang and Faeth [16]	1	$0.23We^{1/2}$	1	0	$We=4-105$	Deformation up to sheet-thinning	-
Chou and Faeth [74]	1 1.43 -2.51	0.5 -0.18 1.79	1 1 1	0 0.25 0	$We=13-20,$ $Oh < 0.05$	Bag	$t^* \leq 2$ $2 \leq t^* \leq 4$ $4 \leq t^* \leq 6$
Cao et al. [75]	1 0.59	0 1.34	0 1	0 0	$We=28-41,$ $Oh < 0.003$	Multi-mode	$t^* \leq 0.3$ $0.3 < t^* < 0.99$
Zhao et al. [25]	1	0.54	1.67	0	$We=16-26,$ $Oh < 0.4$	Multi-mode	$t^* \leq 1.5$

*1Refers to the conditions of the experiments that the corresponding model was based upon. The models are generally valid for low Oh numbers.

Moreover, the temporal evolution of droplet deformation as predicted by the various models is presented in Figure 1-4, along with various experimental data found in the literature in three breakup regimes (bag, multi-mode and sheet-thinning) for $We=15$ [16, 74, 76], $We=20$ [74, 77, 78], $We=52.6$ [79] and $We=101$ [79]. It should be noted that the models of [25, 74] are not valid for high We numbers; nevertheless their results are presented as well in order to assess if their range of applicability can be extended. The experiments are plotted up to the breakup initiation time, while those of [79] have been shifted in terms of time based on the results of CFD simulations at the same conditions. In the bag breakup regime ($We=15$ and 20) the model of Chou and Faeth [74] shows the best agreement with the experimental data, while in the multi-mode regime ($We=52.6$) that of Cao et al. [75] is closest to the experiments. Finally, in the sheet-thinning regime ($We=101$) the model of Gel'fand et al. [73] shows the best performance overall, although a deviation with the experimental data is still observed. It should be noted that although some empirical models show good agreement with the experimental data, they do not have a theoretical derivation, but rather they are based on experimental data. This implies that they don't include the dependence of y on other non-dimensional numbers (ϵ , Oh ,

Re), apart from those examined in the experiments, and therefore they are not applicable outside the range of the experimental conditions from which they have been derived.

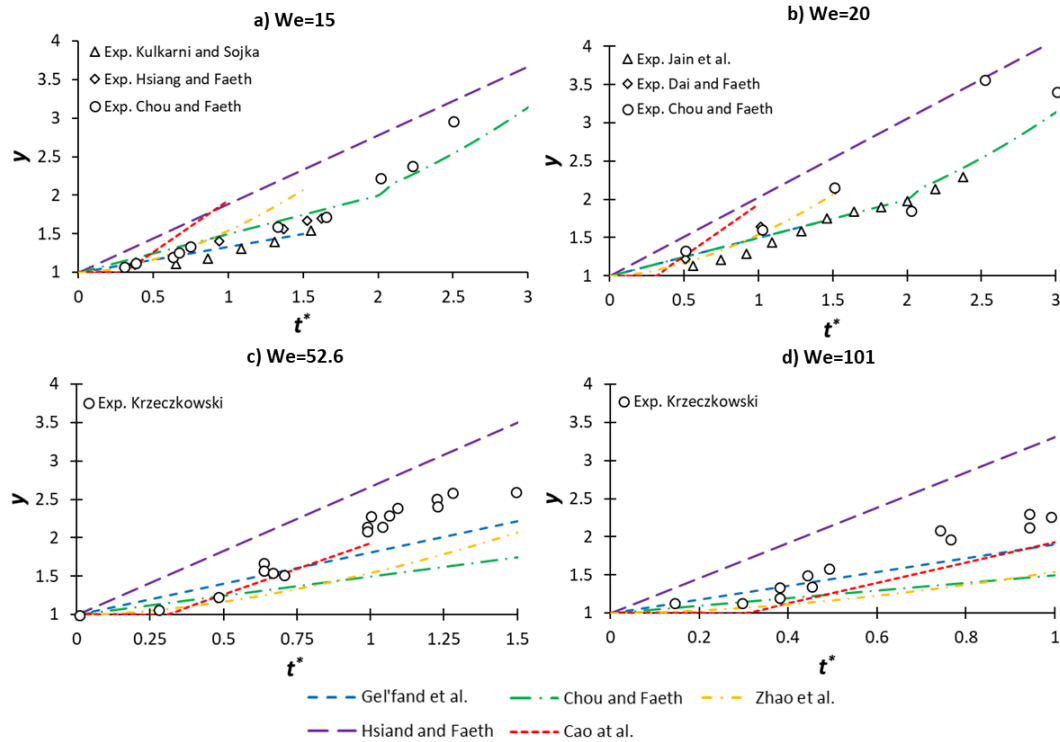


Figure 1-4: Comparison between experimental data and the predictions of the various empirical models for the temporal evolution of droplet deformation for: a) $We=15$, b) $We=20$, c) $We=52.6$ and d) $We=101$.

1.2.3.2 Theoretical and semi-empirical models

Turning now to the theoretical and semi-analytical models of droplet deformation and breakup, the majority of them is based on one of the two basic principles: i) conservation of momentum or ii) conservation of energy. O'Rourke and Amsden [80] proposed the so called Taylor analogy breakup (TAB) model, in which the droplet is assumed to oscillate between its initial spherical shape and that of the deformed oblate shape. The droplet oscillates similarly to a mass-spring-damper system with the surface tension force being the restoring force, the viscosity representing the damping force and the aerodynamic force being the external force acting on the droplet. Lee et al. [81] indicated later that the TAB model shows good agreement with the experiment of Krzeczkowski [79] for the breakup of a water droplet with $We=101$. Later, Kim et al. [22] tuned these coefficients to match the results of their experiments for Diesel droplets at We numbers in the range of 9.6 up to 26.6. Finally, Marek [82] introduced another degree of freedom to the mathematical formulation of TAB, so as to include also the translational motion of the

droplet. A second mass was added to the system, which could move and oscillate independently, and thus the system resembled the system configuration of a double mass-spring-damper giving the name to the model as double mass TAB (DMTAB). The DMTAB is applicable to the deformation and bag breakup regimes and its advantage over the TAB model is that it can treat cases with low density ratios (ϵ) and high Oh numbers, in which the droplet translational velocity changes significantly.

Another approach on the breakup models still based on the momentum balance is that of Villermaux and Bossa [83], in which they utilized the inviscid Navier-Stokes equations in cylindrical coordinates for the liquid droplet, and the quasi-steady conservation of momentum and mass for the gas phase to estimate the temporal variation of the droplet deformation in the bag breakup regime. Opfer et al. [84] used the momentum balance on the droplet as well, which was approximated by a cylinder of the same radius to predict the droplet deformation in the bag breakup regime. Later, Kulkarni and Sojka [76] added the effect of viscosity to the model of [83] and it showed good agreement with their own experimental data for We numbers ranging from 13 up to 15.

Instead of utilizing the momentum balance on the droplet Detkovskii and Frolov [85], and later Wang et al. [86, 87], utilized the equation of the linear strain of the droplet along its cross-stream axis to estimate the droplet deformation. They called the model BTB (bag-type breakup) and its results showed good agreement against the experimental data of [74, 79] in the bag breakup regime.

Regarding the theoretical models based on the conservation of energy, Ibrahim et al. [88] developed the so called deformation and breakup model (DDB), which is applicable to deforming droplets at We numbers greater than 20. Rimbart et al. [89] improved the DDB model by assuming potential flow around the droplet and extensional flow (i.e. with no shear) inside the droplet. The resulting model showed acceptable agreement with the experimental data of [79, 84] for We numbers equal to 11.5, 18.4 and 103.5, while the agreement was not good for the case of $We=13.5$. Schmehl and co-workers [90, 91] utilized the mechanical energy balance on the droplet to derive a non-linear differential equation similar to that of TAB, which they named non-linear TAB (NLTAB). This equation accounts for the modification of the aerodynamic forces imposed by the deformation of the droplet, and it showed good agreement with the experimental data of [77, 92] for the time variation of droplet deformation. Finally, Sichani and Emami [93] utilized the virtual work principle to describe the droplet deformation in the deformation and bag breakup

regimes. The results of the model showed good agreement with the experimental data of [42, 74, 77, 79, 94] for We numbers ranging from 12.5 up to 20.

The aforementioned theoretical models are summarized in Table 1.7 along with their basic characteristics.

Table 1.8: Summary of theoretical and semi-analytical models for droplet breakup.

Model	Basic principle	Droplet shape	Pressure distribution	Internal circulation	Translational motion	Breakup condition	Adjustable parameters	Applicability ^{*1}
TAB [95]	Momentum conservation	Ellipsoid	Uniform	No	No	$y_{cr}=2$	3	-
NLTAB [90, 91]	Energy balance	Ellipsoid	Spatial	Yes	No	$y_{cr}=1.8$ and $\dot{\gamma}=0$ or $y_{cr}=2.1$	1	-
DMTAB [82]	Momentum conservation	Ellipsoid	Uniform	No	Yes	$y_{cr}=2$	3	$We \leq 50$, large and small ε and Oh
DDB [88]	Energy balance	Elliptic cylinder	Uniform	No	No	$y_{cr}=(We/2)/(6\pi)$	0	$We > 20$
Rimbert et al. [89]	Energy balance	Ellipsoid	Spatial (potential flow)	Yes (homothetical deformation)	Yes	$y_{cr}=2$	0	-
BTB [85-87]	Linear strain equation	Ellipsoid	Uniform	No	No	$(B^{-1}+B^5-2B^4)/30 > We$, $B=(3\pi/4)y$	1	$10 < We < 35$, $Oh < 0.1$
Opfer et al. [84]	Momentum conservation	Cylinder	Spatial (parabolic)	No	No	-	2	$11 < We < 25$
Kulkarni and Sojka [76]	Momentum and mass conservation (Navier-Stokes)	Bag	Spatial (stagnation point)	No	No	-	1	$12 < We < 16$
Sichani and Emami [93]	Lagrange-type equations of motion	Bag	Spatial	Yes	No	$\frac{4}{3} \frac{1-K^{*2}}{y_1^2 + y_2^2}$	1	$We \leq 20$, $Re > 100$, $\varepsilon > 500$,

¹Applicability is based on the original paper proposing the model.

² K is a parameter; y_1 and y_2 are the deformations in both axes.

Finally, the performance of selected models: TAB, DDB, NLTAB, Rimbart et al. [89] and Kulkarni and Sojka [76] is evaluated by comparing their results against experimental data in three breakup regimes, similar to the empirical models: i) bag for $We=15$ [16, 74, 76] and $We=20$ [74, 77, 78], multi-mode for $We=52.6$ [79], and sheet-thinning for $We=101$ [79], as presented in Figure 1-5. Again, the applicability of some models has been extended beyond the range presented in Table 1.8 in order to assess their performance outside their suggested range of applicability. Moreover, all models are plotted up to a common time instance, and not up to their breakup condition of Table 1.8, in order to compare their results on a common basis. The experiments are plotted up to the breakup initiation time and also those of [79] have been shifted based on the results of CFD simulations at the same conditions. The TAB, DDB and NLTAB models predict an oscillatory behavior for the droplet deformation, while the models of Rimbart et al. and that of Kulkarni and Sojka predict an exponential behavior. For $We=15$ the model of Kulkarni and Sojka [76] is the only model that agrees well with the experimental data, while for $We=52.6$ and $We=110$ the DDB model gives the best results overall. For $We=20$ all models deviate from the experimental data. The aforementioned observations lead to the conclusion that there is a lack of a single accurate enough model for the prediction of droplet deformation for a wide range of We numbers in the three main breakup modes of low Ma numbers: bag ($We=10-20$), multi-mode ($We=21-65$) and sheet-thinning regimes ($We=66-350$). This occurs due to the dependence of the shape of the deformation curve on the breakup mode: for example, in the bag breakup regime (Figure 1-5a) it has an exponential shape, while in the sheet-thinning (Figure 1-5d) it is close to linear. So far, the TAB model is widely used in spray codes due to its simplicity, since it has an analytic solution. However, it predicts purely oscillatory deformation for all breakup regimes, something that is not realistic. On the other hand, the recently developed model of Kulkarni and Sojka [76] (termed as bag-Navier-Stokes or bag-NS for the remaining of the paper) predicts an exponential growth, which agrees well with experimental observations for the bag breakup mode, but it cannot be used to other breakup modes.

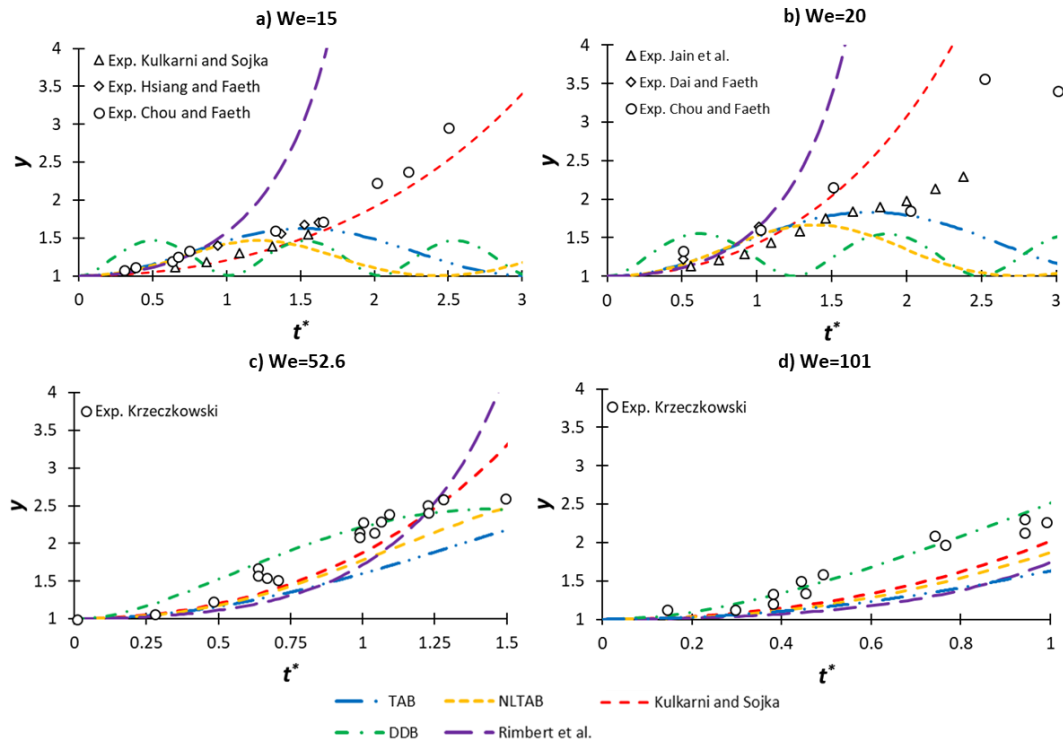


Figure 1-5: Comparison between experimental data and the predictions of the various theoretical models for the temporal evolution of droplet deformation for: a) $We=15$, b) $We=20$, c) $We=52.6$ and d) $We=101$.

1.3 Scope of the PhD thesis - Novelty

The purpose of the current work is, first, to investigate numerically using DNS the phenomena that occur during secondary atomization in fuel sprays and, second, to provide SGS models that can be utilized in CFD codes for the modeling of sprays consisting of millions of droplets.

More specifically, it is the first numerical work, to the author's best of knowledge, that investigates the aerodynamic breakup of isolated droplets for non-dimensional numbers (We , Oh , Re , and ε) representative of Diesel engines operating with Diesel and HFO as fuels. The examined non-dimensional parameters are presented in Figure 1-6, along with those of the aforementioned numerical studies depicted on the $Oh-We$ and $Re-N/\sqrt{\varepsilon}$ planes; both planes are required for the complete description of the physical parameters. The goal is, on the one hand, to validate the numerical model for these conditions, and, on the other, to provide correlations that can predict key droplet quantities, such as the breakup time and drag coefficient, as function of the non-dimensional numbers. Also, apart from the simulations of Figure 1-6, which correspond to low Ma numbers, a simulation with a water droplet exposed to a nitrogen flow of $Ma=1.23$ is simulated, with

the aim of capturing the appearance of micro-droplets at the periphery of the droplet, which has been identified in previous experimental studies but not in numerical ones.

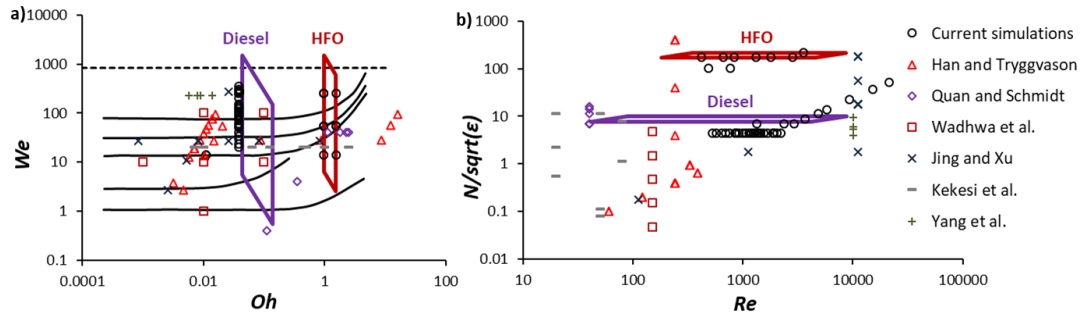


Figure 1-6: Examined parameters of the current and previous numerical studies presented in a) the Oh - We plane and b) the Re - $N/\sqrt{\epsilon}$ plane. The representative Diesel and HFO engine conditions are drawn based on [7, 96, 97].

Moreover, the current thesis investigates the breakup of droplets in cluster formations representative of those encountered in fuel sprays, which is something that has not been examined before. These include formations in which the droplets experience the simultaneous effect of multiple droplets in both the horizontal and vertical directions. To give an idea about the effect of the presence of the surrounding droplets on droplet quantities, Kekesi et al. [57] found that the breakup time of a droplet in tandem formation is up 2 times lower compared to that of an isolated droplet, while for the side-by-side formation it is approximately half.

Initially, the effect of tandem placement is investigated, i.e. one behind the other with respect to the air flow, in which the breakup of four droplets in tandem formation is examined for We and L/D_0 (non-dimensional streamwise distance between the droplets) numbers as presented in Figure 1-7a, along with those of the previous numerical studies. Four droplets are investigated instead of two in order to simulate as much as possible the conditions encountered in fuel sprays, in which streams of “infinite” droplets are present (Appendix A presents a comparison with a simulation of seven droplets). Second, a single-sheet cluster of droplets moving in parallel with respect to the air flow is investigated, which consist of an infinite number of droplets simulated with the use of suitable symmetry boundary conditions, which again resemble the conditions encountered in fuel sprays. The examined We and H/D_0 (non-dimensional cross-stream distance between the droplets) are presented in Figure 1-7b, along with those of the previous numerical studies. As a final step, the two formations are combined resulting in a cluster consisting of four sheets (multi-sheet) moving in parallel to the air flow. These simulations are utilized to

develop correlations that can predict key droplet quantities, such as the drag coefficient and breakup time, as function of the non-dimensional numbers We and L/D_0 (droplets in tandem formation). The proposed correlations provide a better estimation of the aforementioned quantities compared to the correlations derived for isolated droplets. Furthermore, based on the results of the simulations breakup maps are developed, which depict the limits of the encountered breakup regimes in the $We-L/D_0$ and $We-H/D_0$ maps.

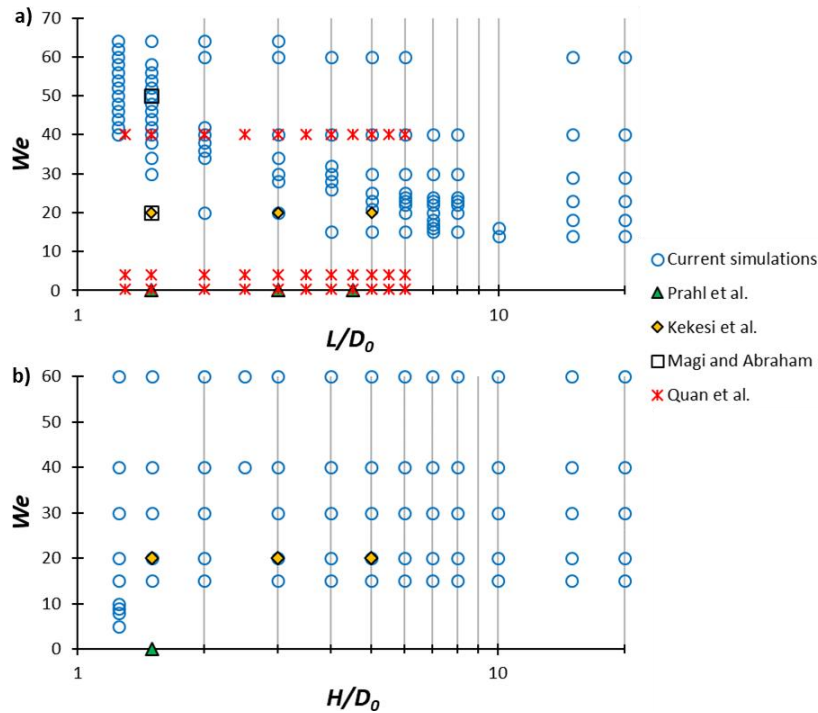


Figure 1-7: Examined We , a) L/D_0 and b) H/D_0 numbers in the current and previous numerical studies.

Finally, a new analytical droplet deformation and breakup model is developed, termed as unified secondary breakup model, which incorporates in a unified way several breakup models of the literature (TAB, DDB, NLTAB and NS). This model along with the existing breakup models TAB and bag-NS [76] (termed as modified-NS or M-NS), which are modified and improved as part of this work, are utilized to predict the droplet deformation in the three main breakup modes: i) bag ($We=10-20$), ii) multi-mode ($We=21-65$) and iii) sheet-thinning ($We=66-350$). These models along with the proposed correlations for the prediction of droplet quantities can be utilized in Eulerian-Lagrangian CFD codes for the simulation of fuel sprays.

1.4 Thesis outline

In Chapter 2, the numerical CFD models for droplet breakup at low and high Mach numbers are presented.

In Chapter 3, the CFD models of the current work are validated against publicly available experimental and numerical data.

In Chapter 4, the results of the 2-D axisymmetric and 3-D simulations of isolated droplet breakup are presented for the description of the flow field along with the parametric studies of Oh and ε numbers.

In Chapter 5, the results of the 2-D axisymmetric and 3-D simulations of droplet clusters are presented for the description of the flow field as well as for the parametric study of We , L/D_0 and H/D_0 . The developed correlations for the prediction of key droplet quantities as function of We and L/D_0 are presented as well.

In Chapter 6, the developed/improved analytical models for droplet deformation and breakup are presented, and their results are compared against those of experimental data and CFD simulations.

In Chapter 7, the main conclusions of the current thesis are presented along with suggestions for future work.

Chapter 2

Numerical models

2.1 Numerical model for droplet breakup

2.1.1 Flow equations and volume of fluid (VOF) method

The CFD model for the aerodynamic breakup of droplets solves the mass and energy conservation equations as well as the Navier-Stokes equations coupled with the Volume of Fluid (VOF) method of Hirt and Nichols (1981) [98], for capturing the interface between liquid and gas.

A single continuity equation is solved for both phases (no mass sources are taken into consideration)

$$\frac{\partial \rho}{\partial t} + \nabla \cdot (\rho \vec{u}) = 0 \quad (2-1)$$

, as also a single momentum equation; the resulting velocity field is shared among the phases:

$$\frac{\partial(\rho \vec{u})}{\partial t} + \nabla \cdot (\rho \vec{u} \vec{u}) = -\nabla P + \nabla \cdot [\mu(\nabla \vec{u} + \nabla \vec{u}^T)] + \rho \vec{g} + \vec{F}_{vol} \quad (2-2)$$

The surface tension forces are included in the momentum equation by using the Continuum Surface Stress (CSS) model of Lafaurie et al. (1994) [99]. In the CSS model the volumetric force is calculated as

$$\vec{F}_{vol} = \nabla \cdot \left[\sigma \left(|\vec{n}| I - \frac{\vec{n} \otimes \vec{n}}{|\vec{n}|} \right) \right], \vec{n} = \nabla \alpha \quad (2-3)$$

The volume fraction α is defined as:

$$\alpha = \frac{\text{Volume of liquid phase}}{\text{Total volume of the control volume}} \quad (2-4)$$

, where the α -function is equal to:

- 1, for a point inside liquid phase.
- 0, for a point inside gas phase.
- $0 < \alpha < 1$, for a point inside the transitional area of the two phases, the interface.

The transport equation for the volume fraction, since no mass sources are taken into consideration, is

$$\frac{\partial \alpha}{\partial t} + \nabla \cdot (\alpha \vec{u}) = 0 \quad (2-5)$$

The values of the density ρ and viscosity μ are calculated using linear interpolation between the two phases weighted with the volume fraction α :

$$\rho = \alpha \rho_l + (1 - \alpha) \rho_g \quad (2-6)$$

$$\mu = \alpha \mu_l + (1 - \alpha) \mu_g \quad (2-7)$$

The energy equation, which is utilized in the high Ma number simulations, where large temperature variations exist, is written for a flow without species and negligible viscous energy dissipation (assumption validated with simulations) as:

$$\frac{\partial(\rho E)}{\partial t} + \nabla \cdot [\vec{u}(\rho E + P)] = \nabla \cdot (k \nabla T) \quad (2-8)$$

, where the energy E is given by

$$E = h - \frac{P}{\rho} + \frac{v^2}{2} \quad (2-9)$$

, with the sensible enthalpy h calculated in its general form [100] by

$$h = \int_{T_{ref}}^T C_p dT + \int_{p_1}^{p_2} \left[v - T \left(\frac{\partial v}{\partial T} \right)_p \right] dp \quad (2-10)$$

, where the specific volume is $v = 1/\rho$. For the ideal gas (air or nitrogen in this work) the second term of the right-hand-side of eq. (2-10) becomes equal to zero, while for the incompressible liquid (water) it becomes equal to $\frac{P-P_{ref}}{\rho}$. When the variations in the liquid pressure are small, such as those encountered in this work, the difference between the incompressible and the compressible calculation of the liquid enthalpy, using for example the Tait EoS, are negligible; preliminary calculations showed that the error is less than 1% for pressures up to 450 bar.

2.1.2 Equations of state (EoS) and rest of fluid properties

For the cases with large density variations, such as those encountered at high Mach numbers, the density of each fluid is given as function of its temperature and pressure using an equation of state for each phase: i) for the gas phase the ideal gas law is utilized ($\rho=PMW_{gas}/RT$), while for the liquid phase the Tait EoS is used (eq. (2-11)):

$$\left(\frac{\rho}{\rho_0} \right)^n = \frac{K}{K_0} \quad (2-11)$$

, where K is the bulk modulus, which is a measure of the compressibility of a liquid, and is given in its general form by:

$$K = V \frac{dP}{dV} \quad (2-12)$$

For the examined conditions of the current work ($T \approx 293.15K$ and P ranges from 1.01325 bar up to ~ 2.8 bar - see sections 3.2.1 and 4.3.1) the bulk modulus can be assumed to vary linearly with pressure [101]: $K=K_0+n\Delta p$, with $\Delta p=p-p_0$ and $n=7.15$ for water [102], with reference values as: $P_0=101325$ Pa, $\rho_0=998.2$ kg/m³, $K_0=2.2 \cdot 10^9$ Pa [103]. It should be noted that for such small changes in the temperature ($\Delta T < 1K$) and pressure ($\Delta P \sim 1.8$) the density of water changes less than 1% and therefore not much difference is

expected in the results with the use of constant density; however, this was not known a priori. For the same reason, the rest of fluid properties (surface tension, viscosity, heat capacity and thermal conductivity) are taken constant for the liquid water at the initial temperature of 293.15 K. For the gas phase (air or nitrogen), which has large variations in the pressure and temperature, the heat capacity and thermal conductivity are taken as functions of temperature, using the polynomial functions of [104]. Finally, the viscosity of gas is found using the Sutherland's law [105].

2.1.3 VOF-to-DPM model

In the cases where a large portion of the droplet is converted into micro-droplets (cases with high Ma numbers), which are smaller than the smallest grid size, a model called VOF-to-DPM (Discrete Phase Model) is utilized that switches from VOF to Lagrange, when certain user-defined criteria are met. In the VOF-to-DPM model of ANSYS FLUENT [106] the liquid volume fraction of a cell is converted into Lagrangian particles (droplets), when certain user-specified criteria are met. In order to avoid spurious momentum sources an equal volume of gas is created in the VOF solution to maintain the volume conservation. The criteria for transition from VOF to DPM in a cell are: i) the volume-equivalent sphere diameter should be within a specified range, which for this work is chosen arbitrarily between zero and the diameter of a particle that would occupy half the volume of an interface cell, and ii) the asphericity should be below 0.5 (the value of zero corresponds to perfect spheres, while the higher it is the more the shape deviates from that of sphere). After the particles-droplets have been created, their trajectory is tracked using the force balance on each of them separately, as given by eq. (2-13):

$$m_d \frac{d\vec{u}_d}{dt} = m_d \frac{\vec{u} - \vec{u}_d}{\tau_r} + m_d \frac{\vec{g}(\rho_d - \rho_g)}{\rho_d} + \vec{F} \quad (2-13)$$

The first term on the right-hand side is the term of the drag force, the second term is the gravity force, which is negligible compared to the aerodynamic force, and the third one includes all other forces (virtual mass, pressure gradient etc), which in the current work of high density ratio ($\rho_p/\rho_g \gg 1$) are considered negligible. τ_r is the droplet relaxation time calculated by:

$$\tau_r = \frac{\rho_d d_d^2}{18\mu} \frac{24}{C_D Re} \quad (2-14)$$

, with Re the relative Reynolds number given by:

$$Re = \frac{\rho_d d_d |\vec{u}_d - \vec{u}|}{\mu} \quad (2-15)$$

, and C_d the drag coefficient, calculated using the spherical drag law as:

$$C_d = a_1 + \frac{a_2}{Re} + \frac{a_3}{Re} \quad (2-16)$$

, where the coefficients α_1 , α_2 and α_3 are given in [107]. It should be noted that the correlations developed as part of this work for the prediction of the C_d (section 4.2.2.3 and 5.2.2.2) provide a better estimation compared to eq. (2-16) for fuel sprays, however, there is no option in the current version of FLUENT (19.2) to implement them as user-defined functions.

2.2 Numerical settings, assumptions and grid

The CFD simulations are carried out using the commercial CFD tool ANSYS FLUENT v16 [108] and v19 [109]. The finite volume method (FVM) [110] is applied for the formulation of the equations, while the resulting system is solved with the PISO algorithm [111] of the segregated pressure-based solver [72]. The pressure equation is spatially discretized using the body force weighted scheme [72], while for the momentum equation the second order upwind scheme [112] is utilized. The temporal discretization of all equations is done with the bounded second order implicit scheme [72], while the time-step is such that the Courant number ($Cou=u\Delta t/\Delta x$) is kept equal to 0.5. The VOF equation is solved implicitly and is spatially discretized with the compressive scheme [72], which is a second order reconstruction scheme based on the slope limiter. The latter is applied to avoid spurious oscillations or wiggles that would otherwise occur with high order spatial discretization schemes due to sharp changes in the solution domain. The value of the volume fraction

at a face of a control volume, which is required by the control-volume formulation of FLUENT, is calculated as:

$$\alpha_f = \alpha_d + \beta \nabla \alpha_d \cdot \vec{dr} \quad (2-17)$$

, where α_f is the face VOF value, α_d is the donor cell VOF value, \vec{dr} is the cell to face distance and β the slope limiter value, which is equal to 2 for the compressive scheme. Preliminary simulations using the modified HRIC scheme, which is the only other scheme that is available in FLUENT with the current numerical settings, have showed that the average droplet velocity, deformation and surface area change less than 1.5%, when the discretization scheme is changed. It should be mentioned that all the presented droplet shapes in the current work have been drawn based on the VOF iso-value of 0.5, while all the examined droplet quantities (velocity, deformation, surface area etc) have been calculated for the liquid region with $\alpha \geq 0.5$. Nevertheless, the selection of the value of 0.5 does not affect much the results, as can be seen in Figure 2-1, which presents a deformed droplet shape drawn using the iso-values of: 0.01 (green line), 0.5 (black line) and 0.99 (red line). This shows how sharp is the interface with the use of the compressive scheme, even at the latter stages of deformation.

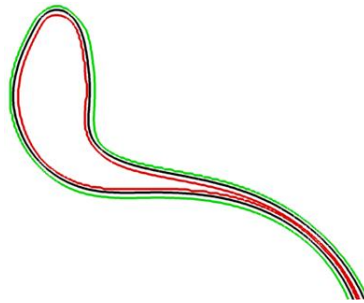


Figure 2-1: Droplet shape depicted with the VOF iso-values of: 0.01 (green line), 0.5 (black line) and 0.99 (red line).

In addition to the aforementioned numerical settings, various user-defined functions (UDFs) have been utilized for: i) the adaptive local grid refinement technique around the liquid-gas interface [113], ii) the adaptive time-step scheme for the implicit VOF solver based on the velocity at the droplet interface [114], iii) the moving mesh technique based on the average velocity of the droplets, iv) the pressure outlet boundary condition, utilized in the high Mach number simulations to patch at the top boundary the value of

the pressure and temperature of the neighboring cell, and v) the fluid properties as a function of temperature for the cases in which the energy equation is solved.

The majority of the simulations has been performed in 2-D axisymmetric computational domains, while also some 3-D simulations are performed as well, when necessary. To give an idea about the resources required with each domain, a 3-D simulation of an isolated half droplet took approximately 15 days using 36 computational cores, while the corresponding 2-D one took 5.5 hours using a single core; this makes it prohibitive with the current numerical tools to utilize only 3-D domains for the parametric studies of this work. Apart from the three-dimensional nature of droplet breakup, which becomes important at the last stages of breakup, limitations of axisymmetric simulations appear in the deformation and breakup of droplets due to turbulence and vortex shedding [78]. Nevertheless, at low Reynolds numbers the axisymmetric approximation has proven to be relatively accurate during deformation stages [115-117]. In addition, in [30, 118] some 3-D simulations show that symmetry is present in the low Reynolds regime. Finally, the axisymmetric simulations do not allow the prediction of the characteristics of the secondary droplets resulting from the breakup of the main droplet, which is not the aim of the current work. To summarize, the selection of the 2-D axisymmetric domain for the parametric studies of this work enables much faster results compared to a 3-D domain, without sacrificing much of the accuracy of the results.

The grid in the simulations comprises of rectangular/hexahedron cells, while systematic runs with 48, 96, 192 and 384cpR have shown that the resolution of 96cpR is adequate as the mean drop velocity and deformation change less than 1% when a finer grid is used. This would require approximately 22.6 billion cells for a 3-D simulation with the domain of Figure 3-1b, which is prohibitive with the current numerical tools. For this reason, a local adaptive refinement technique is utilized, which reduces the required cells to approximately 7 million and the corresponding computational resources (CPU·hours) by approximately 3000 times, while keeping the same resolution at the interface. A base grid resolution of 3 cells per radius (cpR) is utilized, while 6 levels of refinement (or 5 for the 3-D cases) are sequentially applied in order to achieve the desired resolution of 192cpR (or 96cpR for the 3- D cases). In Figure 2-2, the levels of refinement are shown around the liquid-gas interface. The refinement algorithm identifies the cells of the interface (those with a VOF iso-value of 0.5) and then calculates the distance of all computational cells from the interface. Starting with the first refinement level (or the last for coarsening) and continuing with the rest, the cells are refined/coarsened based on the

aforementioned distance and the desired thickness of each refinement level. This procedure is performed every 10-20 timesteps so as the interface lies always in the densest grid region.

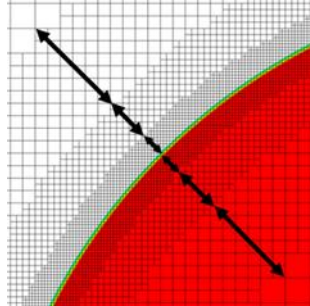


Figure 2-2: Levels of local refinement around the liquid-gas interface.

It should be noted that the energy equation (2-8) is only solved for the cases of high Ma numbers, while for the cases of low Ma numbers the heating and evaporation of the droplets is neglected, since the primary scope of this work lies on the investigation of the aerodynamic breakup process. In view of that, any variations of droplet physical properties with temperature, including that of surface tension, were neglected, as the flow was considered to be isothermal. The justification for this approximation is given using the model of Strotos et al [119] to predict the heating and evaporation of an isolated Diesel droplet for $We=15$ (bag breakup), $We=60$ (multi-bag) and $We=200$ (sheet-thinning). The Diesel and air physical properties are those of Table 5.1 , while the temporal evolution of droplet surface area is calculated based on the CFD simulations. For all cases up to the time of breakup initiation, less than 1% of the droplet mass has been evaporated, while the mean temperature of the droplet increases at maximum 14.5K. This change of liquid temperature results in a decrease in its surface tension and viscosity equal to approximately 5.2% and 19.2%, respectively (properties based on [120] and [121], respectively). An equal change occurs also in the We and Oh numbers, respectively, indicating that the assumption of constant properties does not have a significant effect on the results, while making it possible to perform faster and less complicated simulations (two less equations are solved compared to a case which solves the energy equation coupled with an evaporation model). The aforementioned numerical settings and grid resolution are applied in all the simulations of the current work, unless otherwise stated in the relevant section.

Chapter 3

Model Validation

3.1 Introduction

The CFD model has been developed and validated in previous works for numerous applications, including the free fall of a droplet [113], the droplet impingement on a flat wall [122] or a spherical particle [123-125], the aerodynamic droplet breakup at low pressures and low Ma numbers [114, 117, 119, 126-131], and the droplet evaporation [114, 119, 132]. In the following sections, the model validation is extended to the cases of the aerodynamic breakup of Diesel droplets at high pressure conditions, as well as the breakup of water droplets at high Mach numbers. It should be mentioned that the extension of the model validation for the case of droplet clusters is not possible since, to the author's best of knowledge, there are no experimental studies in the literature with droplet clusters, only a few featuring two droplets [63, 65, 133]. However, even with two droplets a 3-D simulation would require approximately four times more computational resources than the simulation of half droplet, in terms of CPU-hours. For this reason, and since the physical process is the same between the breakup of one and more droplets, we have assumed that the model is considered validated using only the case of the isolated droplet.

3.2 Droplet breakup at low Mach numbers

3.2.1 Computational setup

Both 2-D axisymmetric and 3-D simulations are performed for the simulations of droplet breakup at low Mach numbers, the computational domains of which are shown in Figure 3-1. The 3-D approach (in relevance to the 2-D one), apart from being able to capture the 3-D flow structures, is also able to capture the droplet motion and deformation along the cross-stream direction (X-axis in the 3-D domain). This secondary motion is only present in the experiments of Liu and Reitz [18] and Lee and Reitz [19], and its significance is discussed in a subsequent section. In order to decrease the

computational cost only half of the droplet is simulated, applying symmetry boundary conditions similar to [127]. The incoming gas from the velocity inlet boundary condition is responsible for the droplet deformation and motion in the streamwise deformation (Z-axis). The mesh is moving in the same direction with velocity equal to the average velocity of the droplet calculated using a UDF, in order to ensure that the droplet always lies within it.

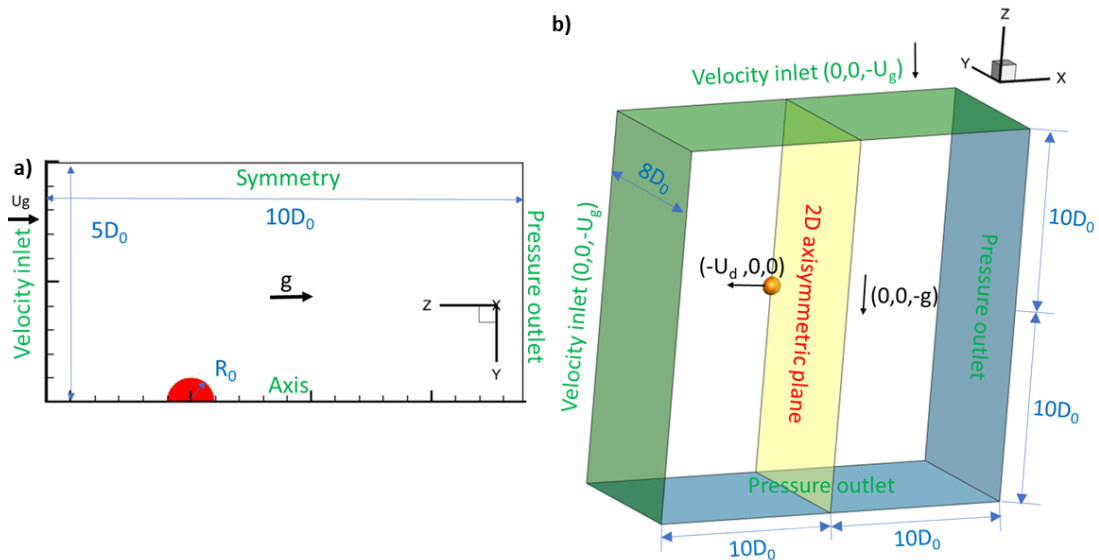


Figure 3-1: Computational domain utilized for the a) 2-D axisymmetric and b) 3-D simulations of droplet breakup at low Mach numbers.

3.2.2 Examined conditions

The liquid droplet is Diesel with properties based on [18], as shown in Table 3.1, while the surrounding gas is air with properties calculated based on the ideal gas law and the Sutherland's law. The droplet diameter and velocity are calculated based on the corresponding experiment used for comparison, as shown in Table 3.2, where the four examined cases are presented along with the correspond non-dimensional numbers. The examined We numbers range from 14 up to 264, covering a wide range of breakup regimes, while the density ratio changes from 695 ($P=1\text{bar}$) down to 79 ($P=9.2\text{bar}$). Since Diesel is incompressible it can be assumed that its properties do not change much at moderately higher pressures, such as those encountered in this work. The Oh number is lower than 0.04 so its effect on the phenomenon is considered to be insignificant [4]. The Ma number is well below 1 for all cases so the effects of compressibility are not considered. In the following sections, the numerical results are compared against the experimental data of Arcoumanis et al. [14], Liu and Reitz [18] and Lee and Reitz [19].

Table 3.1: Properties of liquid Diesel at $T=293.15\text{K}$ and $P=1\text{bar}$ based on [18].

T_L (K)	P_L (bar)	μ_L (kg/m·s)	ρ_L (kg/m ³)	σ (N/m)
293.15	1	0.00217	824	0.02

Table 3.2: Examined cases for the validation of the low Ma number droplet breakup model.

Case	Domain	D_0 [μm]	P [bar]	We	Oh	Re	ε	Ma	Breakup mode	Relevant experiment
1	2-D	2400	1	14	0.011	1540	695	0.03	Bag	[14]
2	2-D/3-D	198	1	54	0.038	864	695	0.20	Multi-bag	[18]
3	2-D	198	1	254	0.038	1867	695	0.43	Sheet-thinning	[18]
4	2-D	184	9.2	264	0.039	5761	79	0.15	Sheet-thinning	[19]

3.2.3 CFD results – comparison against experimental studies

3.2.3.1 Bag breakup mode ($We=14$)

The results from the simulation of case 1 ($We=14$) are compared against the experimental data from the publication of Arcoumanis et al. [14]. Figure 3-2 illustrates the temporal evolution of droplet shape (using the VOF iso-value of 0.5) and the predicted deformation in the two axes. The droplet deforms into an oblate shape up to the time of approximately $1.4t_{sh}$, as it grows in the streamwise direction and thins in the cross-stream one. Then, it takes a bag shape up to $t=1.75t_{sh}$, while throughout this period the deformation increases in both directions. Eventually the bag breaks into small fragments at $t=1.85t_{sh}$. The evolution of droplet shape and the droplet deformation are correctly predicted by the model up to the time of breakup initiation. The main difference between the simulation and the experiment lies on the prediction of the breakup initiation time, which is equal to $1.85t_{sh}$ in the simulation compared to $2.93t_{sh}$ in the experiment. Nonetheless, the predicted breakup time of $1.85t_{sh}$ is located within the proposed boundaries given by Pilch and Erdman [38] and Dai and Faeth [77] (see Figure 3-11 later in this section).

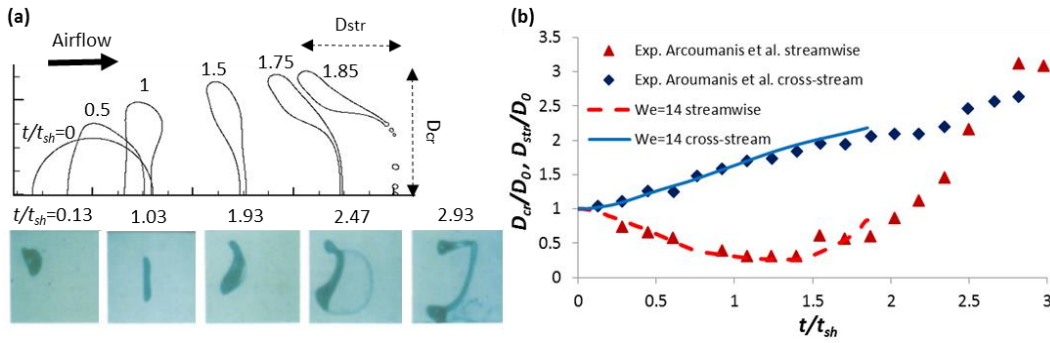


Figure 3-2: Temporal evolution of a) droplet shape and b) deformation, from the simulation of case 1 ($We=14$) and the experiment of Arcoumanis et al. [14].

3.2.3.2 Multi-mode breakup mode ($We=54$)

The droplet shapes for case 2 with the intermediate We number of 54 are presented in Figure 3-3. This includes the predicted droplet shapes for (a) the 2-D axisymmetric, (b) the 3-D simulations (X-Z plane), as well as (c) the corresponding experimental photos of Liu and Reitz [18]. Up to the time of $1.4t_{sh}$ the droplet deforms into an oblate shape, similar to case 1 (bag breakup), followed by the growth of a toroidal bag at the periphery of the drop rather than at its center, as in case 1 ($We=14$). This breakup mode pertains to the multi-bag (multimode) breakup regime instead of the bag reported in the experiment, as shown in Figure 3-3c: the drop takes an oblate shape (droplet no. 3 in image i), followed by the formation of the bag (droplet no. 4 in image i), and the subsequent breakup into small fragments (droplet no.4 in image ii). Nevertheless, the predicted multimode breakup is in accordance with the breakup regions in the $Oh-We$ map of Hsiang and Faeth [15] (Figure 1-6) for the examined We and Oh numbers. In order to further investigate if this discrepancy is ought to 3-D phenomena and also to assess the effect of the cross-stream droplet motion, corresponding 3-D simulations have been conducted and presented in Figure 3-3b. The 3-D simulations reveal a quite similar behaviour with the 2-D ones, apart from a predicted slightly later breakup initiation time ($1.8t_{sh}$ compared to $1.65t_{sh}$ in the 2-D simulation) and a slight tilting of the droplet. The latter is ought to the declination of the relative drop-gas velocity from the vertical direction (Figure 3-3b) and it is not affecting the general model performance. A more representative view of the 3-D simulation is presented in Figure 3-4 showing the formation of two bags instead of the torus predicted by the 2-D simulation.

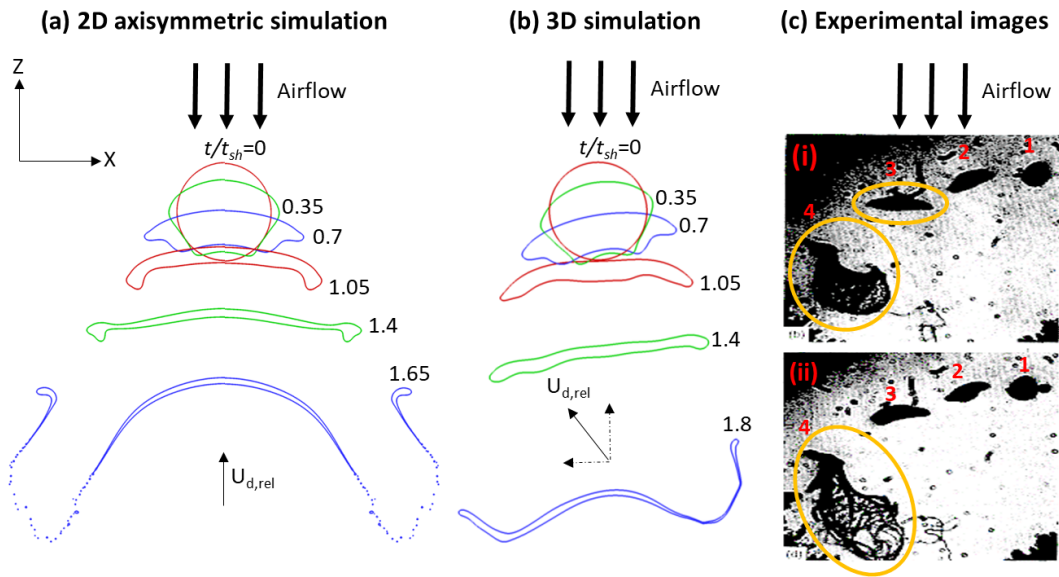


Figure 3-3: Temporal evolution of droplet shape as predicted by: a) the 2-D axisymmetric simulation of case 2 ($We=54$), b) the 3-D simulation of case 2, and c) the experiment of Liu and Reitz [18].

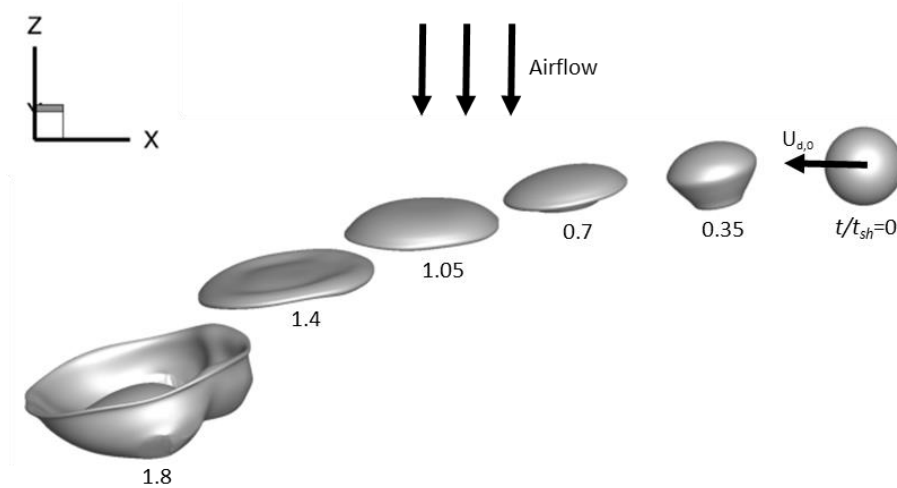


Figure 3-4: Temporal evolution of droplet shape from the 3-D simulation of case 2 ($We=54$).

Regarding the quantitative comparison between the simulation of case 2 and the experiment of Liu and Reitz [18] the graph of the deformation as function of the distance travelled along the cross-stream direction is given in Figure 3-5. The deformation increases gradually with the distance travelled both in the simulation and the experiment, between which good agreement is observed.

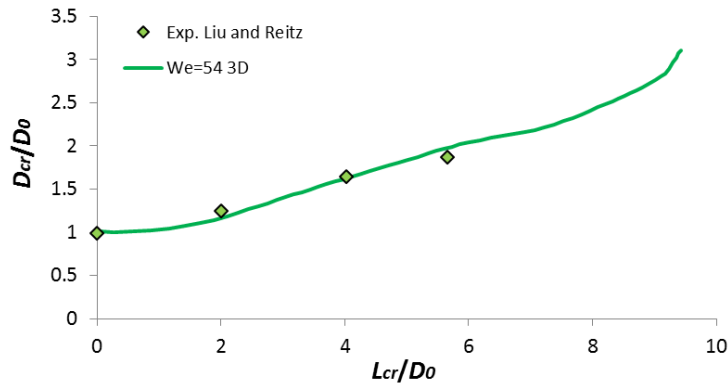


Figure 3-5: Droplet deformation for the simulation of case 2 ($We=54$) and the experiment of Liu and Reitz [18] as function of the distance travelled in the cross-stream direction.

For the examined conditions of case 2 ($Re=864$), vortex shedding behind the droplet should normally be present; for spherical droplets this is observed for Re numbers in the range 400 up to $3.5 \cdot 10^5$ [134]. The frequency f of the vortex detachment is generally expressed through the Strouhal number ($St = fD_0/U_{rel,0}$), which is equal to 0.2 for solid spheres [134] and 0.13 for solid disks [135] based on the Re number of the simulation. This phenomenon can be captured only in the 3-D simulations and it is visualized using the streamlines of relative velocity as presented in Figure 3-6, in which alternating vortices are observed to detach from the droplet surface in the symmetry plane (X-Z). According to Sakamoto and Haniu [136] the vortices in solid spheres with $Re > 480$ are detached periodically from a point at the wake of the droplet that rotates around an axis through the center of the sphere. Achenbach [137] states that there are four detachment points at the wake of the drop in a helical formation and defines the vortex shedding period as the time between two consecutive detachments. Due to the adoption of the symmetry boundary condition, asymmetrically forming vortices cannot be captured with the current setup. Nevertheless, an indication of the vortex shedding period can be estimated to be equal to half the time between the separation of two consecutive vortices in the X-Z plane (at $t=0.7t_{sh}$ and $t=1.1t_{sh}$). This period results in a Strouhal number equal to 0.19, which is a value slightly less than the value of solid spheres. It should be noted that although the symmetry boundary condition is not suitable for predicting the 3-D gas flow structure its effect on the liquid phase deformation is minimal.

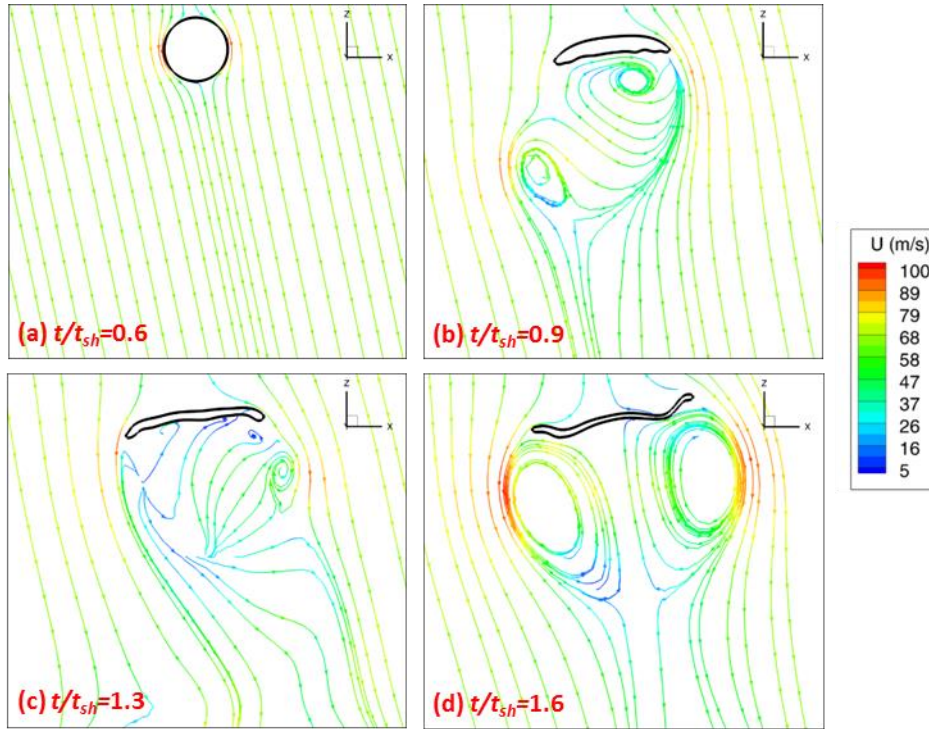


Figure 3-6: Vortex shedding in the 3-D simulation of case 2 at various time instances (streamlines coloured with velocity magnitude).

3.2.3.3 Sheet-thinning breakup mode ($We=254$)

Turning now to the cases subjected to sheet-thinning breakup mode, the temporal evolution of droplet shape for cases 3 and 4, as well as the corresponding experimental photographs of Liu and Reitz [18] and Lee and Reitz [19] are illustrated in Figure 3-8. These cases have similar We numbers (254 compared to 264), but different density ratios (695 compared to 79). The sheet-thinning breakup modes predicted for the two cases are in agreement with the corresponding experimental data. The drop initially deforms into a disk-like shape, which is a common feature for all breakup modes, followed by the formation of a thin liquid sheet at the periphery of the drop. This liquid sheet forms ligaments, which are eventually detached from the droplet during the breakup process, as observed both in the numerical predictions as well as the experimental images (droplet no. 3). The breakup time is lower in the case with $\varepsilon=79$ compared to the one with $\varepsilon=695$, equal to $0.8t_{sh}$ against $0.95t_{sh}$ respectively. It should be mentioned that the breakup time in this case as well as in the rest of the thesis is measured as the time instance that a fragment, even a small one, is detached for the first time from the parent droplet, and is measured manually in the simulations using a visual representation of the process

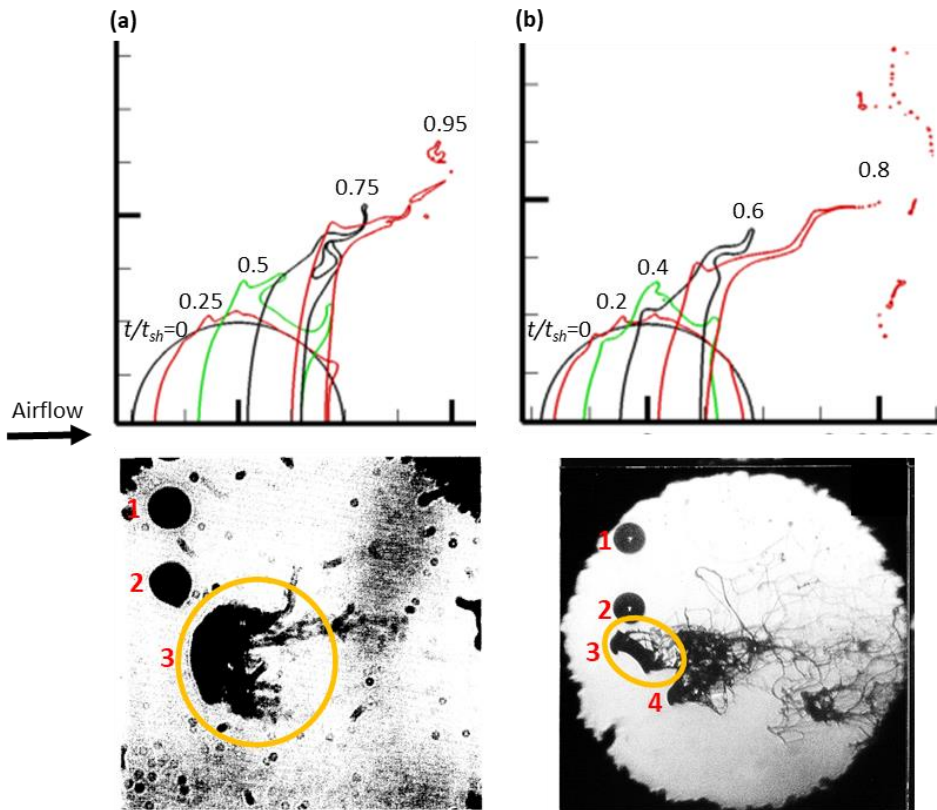


Figure 3-7: Temporal evolution of droplet shape for: a) case 3 ($We=254$, $\epsilon=695$) and the experiment of Liu and Reitz [18], and b) case 4 ($We=264$, $\epsilon=79$) and the experiment of Lee and Reitz [19].

The cross-stream deformation as function of the distance travelled in the cross-stream direction for case 3 ($We=254$) and the corresponding experimental data of Liu and Reitz [18] are shown in Figure 3-8. It should be mentioned at this point that the measurement of the deformation in the simulations does not take into account the small droplets that are detached from the parent droplet (see for example Figure 3-8b at $t^*=0.8$); this occurs in all the examined cases of the thesis. Similar to case 2, it is observed that the deformation increases with the distance, while there is also a very good agreement between the simulation and the experiment.

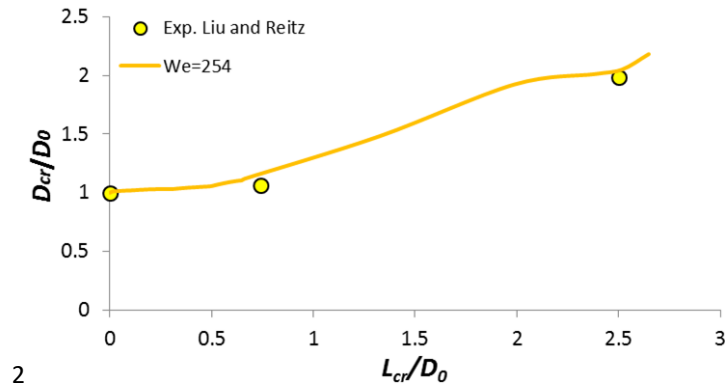


Figure 3-8: Droplet deformation for the simulation of case 3 ($We=254$) and the experiment of Liu and Reitz [18] as function of the distance travelled in the cross-stream direction.

3.2.3.4 Overall assessment of the effect of We number

In this section, the overall effect of the We number for all the four validation cases is addressed. Starting with the temporal evolution of the cross-stream droplet deformation this is presented in Figure 3-9. It is observed that the rate of deformation increases with the We number in agreement with the experiment of [21] and the numerical studies of [26] and [28].

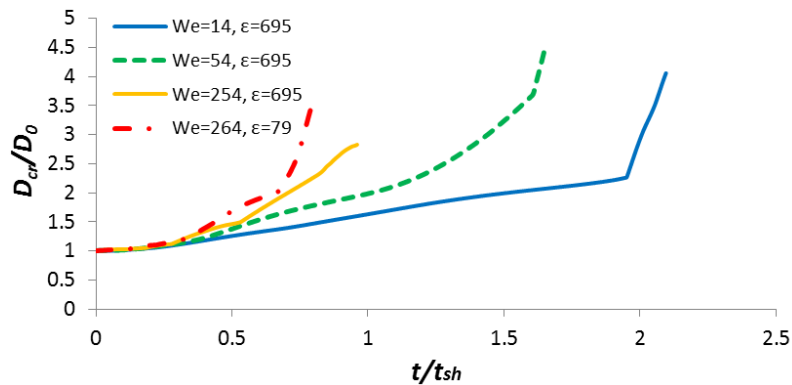


Figure 3-9: Temporal variation of the cross-stream deformation for all validation cases.

The next parameter that is investigated is the non-dimensional droplet velocity $U_d/(U_{g,0}-U_d)$, which is presented in Figure 3-10 along with the experimental results of Dai and Faeth [77] ($We=15-150$ and $\epsilon=680-850$). As seen, the dimensionless character of droplet velocity is confirmed for all examined cases. Only the case with $\epsilon=79$ shows a small deviation from the experimental data probably due to the small density ratio compared to the large density ratios examined in the experiments; the Re numbers between those cases differ also a lot.

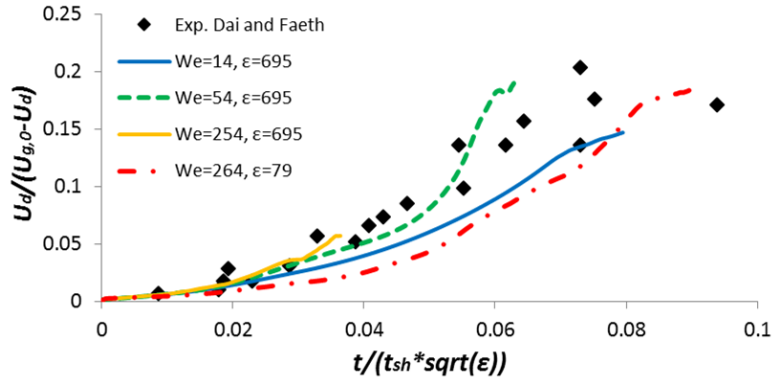


Figure 3-10: Non-dimensional droplet velocity as function of modified time for all validation cases and the experiment of Dai and Faeth [77].

Regarding the non-dimensional breakup initiation time, this is presented in Figure 3-11 as a function of the We number along with the correlations suggested by Pilch and Erdman [38] and Dai and Faeth [77]. The breakup initiation time decreases with increasing We number, while the predicted breakup times are located within the proposed experimental boundaries; the low We number cases (bag and multi-bag) seem to be closer to the correlation of Dai and Faeth [77], whereas the high We number cases (sheet-thinning) are closer to the correlation of Pilch and Erdman [38].

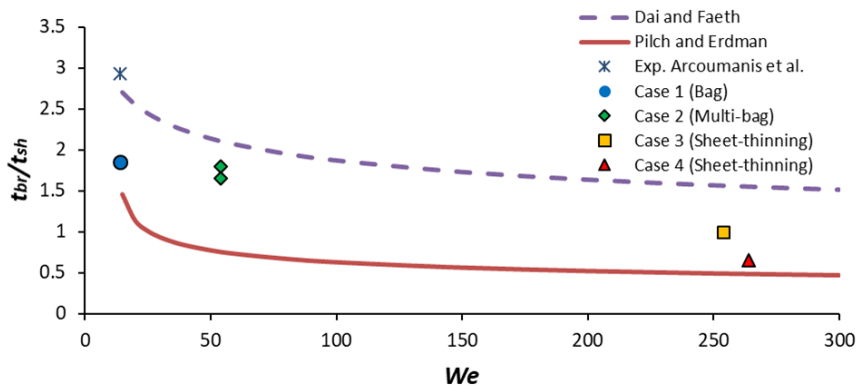


Figure 3-11: Predicted breakup initiation time as function of the We number for the validation cases along with the experimental correlations of Pilch and Erdman [38] and Dai and Faeth [77].

3.2.4 Conclusions

For the validation of the droplet breakup model for low Ma numbers, 2-D axisymmetric and 3-D simulations have been performed with isolated Diesel droplets exposed to an air flow of We ranging from 14 up to 264, density ratio from 79 up to 695, Oh number below 0.04 and Ma number below 0.43. It is proved that the model is capable of predicting with satisfactory accuracy the breakup modes in three breakup regimes, i.e.

a) bag, b) multimode and c) sheet-thinning. In addition, the temporal evolution of droplet deformation and that of the non-dimensional velocity are in agreement with the experimental data of [14, 18, 19], while the predicted breakup initiation times lie within the proposed limits by Pilch and Erdman [38] and Dai and Faeth [77]. Finally, the 3-D simulation of droplet breakup indicates the appearance of vortex shedding simultaneously with the breakup process, with a roughly estimated frequency slightly less than the one for a flow around solid spheres. The validated model is utilized in Chapter 4 to investigate the breakup of isolated droplets at high Oh numbers as well as in Chapter 5 for the simulation of droplet clusters.

3.3 Droplet breakup at high Mach numbers

3.3.1 Computational setup

For the validation of the numerical model for droplet breakup at high Mach numbers a 2-D planar simulation is performed, as shown in Figure 3-12. The shock wave is initialized as a step change in pressure, temperature and velocity (pink color in the figure), which are calculated based on the desired Ma number using a Riemann solver [138]. The liquid droplet (or column in 2 dimensions) is initially stagnant located at a distance equal to $1D_0$ from the shock wave, while the passage of the shock triggers its motion and deformation. The pressure outlet boundary condition at the top of the domain patches the value of the temperature and pressure of the neighboring cell at the boundary, via a UDF, implying transmissive and partially reflective boundary. The computational mesh has increasing cells in the Y-direction, therefore increasing the numerical diffusion when a wave moves towards the boundary, smoothing the gradients and minimizing reflections, thus avoiding the need to move the top boundary at a very large distance. The pressure boundary condition at the right of the domain is non-reflecting, while the one on the left is not in order to avoid discontinuities in the velocity. The grid comprises of rectangular cells applied at two regions of the domain with different grid density (420000 cells in total): i) a rectangle of $8D_0$ length and $3D_0$ height with a resolution of 50 cpR, starting from the front of the shock wave and extending $7D_0$ downstream of the droplet, and, ii) the rest of the domain, in which the cell size increases gradually as the distance from the droplet increases, similar to [139]. The time step is such that the acoustic Courant number is equal to 0.8, i.e. below 1, which is common for flows with shock waves [139, 140]. Moreover,

for the discretization of the VOF equation an equal blending between first and second order schemes is utilized, which gives the best agreement with the results of [139, 141].

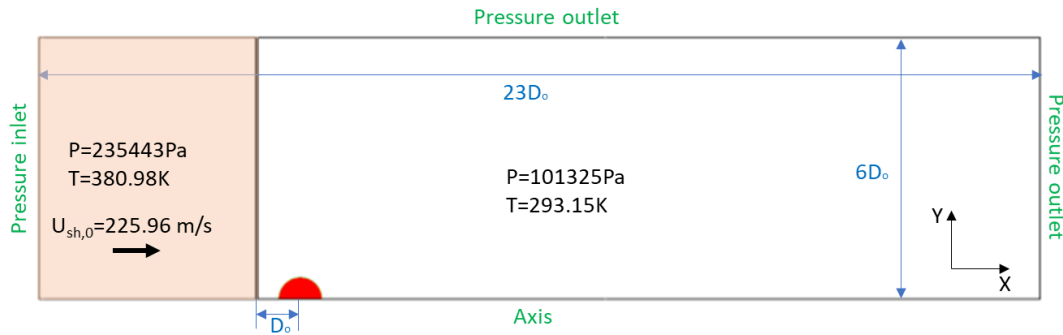


Figure 3-12: 2-D planar computational domain used for the simulation of water droplet breakup at high Ma number.

3.3.2 Examined conditions

The liquid droplet is water with diameter based on [139], while the surrounding gas is air. The properties of both have been described in section 2.1.2 and the resulting non-dimensional numbers are presented in Table 3.3, calculated based on the post-shock properties. In the following sub-sections, the results of the simulation are compared with the experimental data of [141, 142] and the simulation of [139].

Table 3.3: Droplet diameter and non-dimensional numbers for the 2-D simulation of droplet breakup at high Ma number.

D_0 (m)	We	Re	Oh	ε	Ma
$4.8 \cdot 10^{-3}$	7355	107069	0.0017	831	1.47

3.3.3 CFD results – comparison against experimental and numerical studies

3.3.3.1 Description of fluid flow

In the numerical simulations of multiphase flows with shock waves a function called Schlieren is commonly used for visualization of the process [143]. This is given in eq. (3-1).

$$\varphi = \exp \left(-k \frac{|\nabla \rho|}{\max |\nabla \rho|} \right) \quad (3-1)$$

, where k is a scaling parameter equal to 40 for air and 400 for water [144].

The pressure and Schlieren function contours as predicted by the simulation are presented in Figure 3-13 for various time instances. At the time instance of $t^*=0$ the shock wave front touches the surface of the water droplet, while at $t^*=0.008$ it passes over it and part of it is reflected radially. The droplet starts to deform after some time from the passage, at approximately $t^*=0.171$, taking initially a mushroom-like shape ($t^*=0.444$), followed by an ellipsoid one ($t^*=0.808$). Eventually the breakup occurs with liquid stripping from the periphery of the droplet, which is not clearly visible due to the diffusion of the volume fraction, attributed to the selection of the lower order discretization scheme. This scheme, however, gives results closer to those of [139, 141, 142].

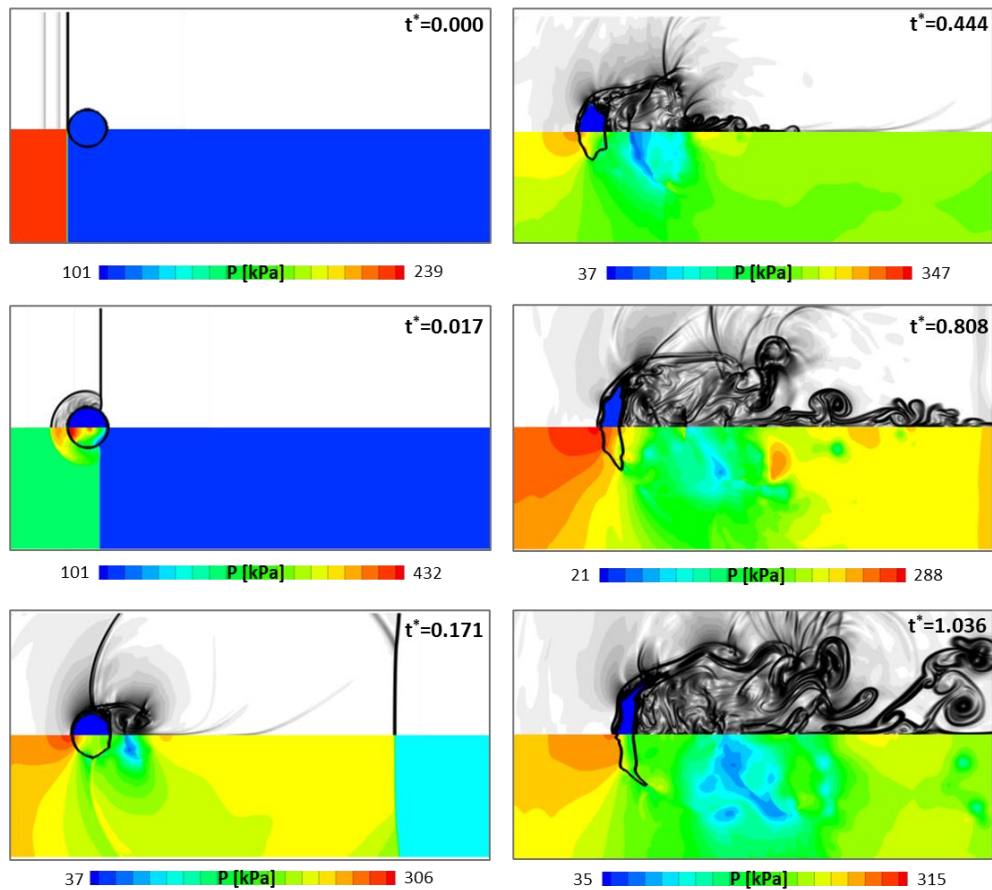


Figure 3-13: Pressure and Schlieren contours from the 2-D simulation of shock-wave induced droplet breakup ($\alpha=0.5$). Flow is from left to right.

The results from the simulation of Meng and Colonius [139], which has been performed at the same conditions, are presented in Figure 3-14 for the same time instances for comparison. The temporal evolution of droplet shape as well as the pressure and Schlieren contours are similar between the two simulations. However, a difference

between them lies in the prediction of a slightly thicker and wavier droplet shape in the simulation of this work compared to that of [139], as it is visible at the time instance of $t^*=1.036$. This might be attributed to the different discretization schemes used in the two simulations (WENO in [145] compared to the blending of first and second order) as well as to the use of the stiffened gas EoS compared to the Tait equation in this work.

Figure 3-15 presents the holographic interferograms from the experiment of Igra and Takayama [142] as well as the Schlieren contours as predicted by the simulation of the current work along with that of [139]. The curved black lines correspond to the reflection (R) of the shock-wave in the droplet as well as its diffraction (D). As it is observed from the figure, the shock wave reflection is very similar in the three works for both time instances. Finally, it should be noted that the time in the experiments is higher compared to both simulations, probably due to a reporting error in [142] or a misunderstanding of the phrase “time after the interaction between the incident shock wave and the water column” of the original work of [142], as already discussed thoroughly in [139].

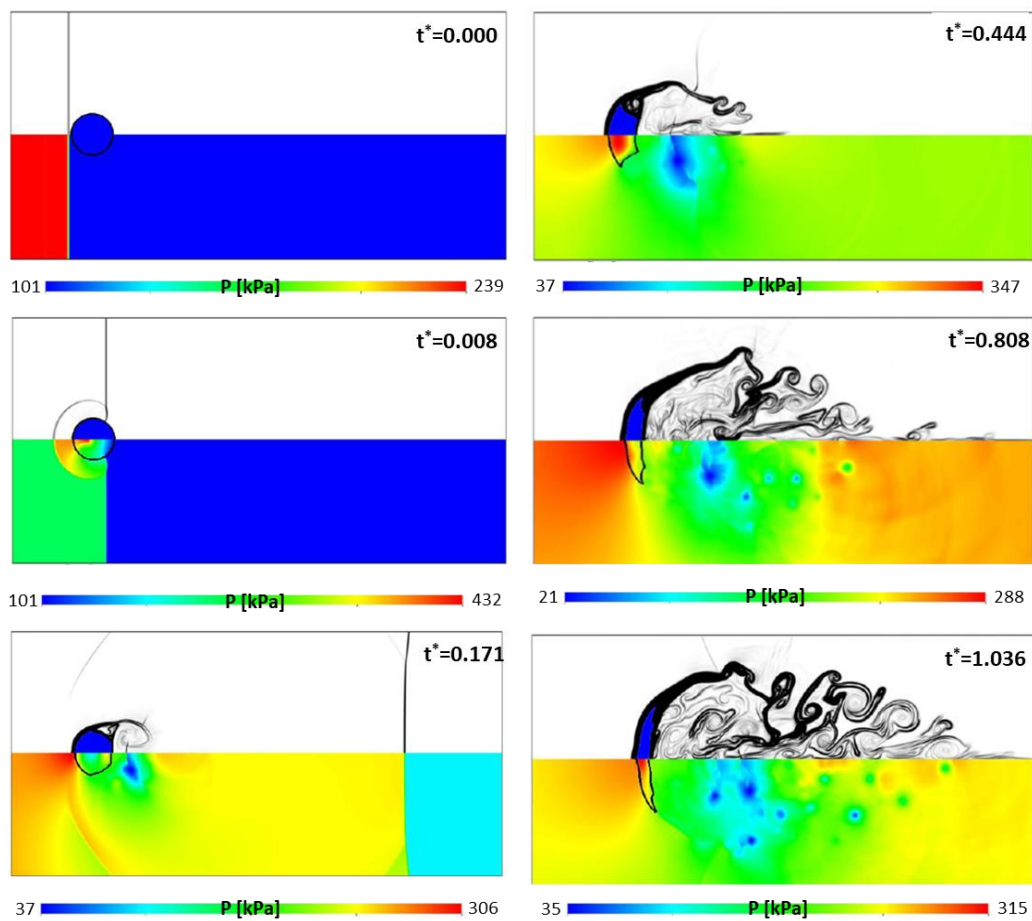


Figure 3-14: Pressure and Schlieren contours as predicted by the simulation of [139] ($\alpha=0.9$). Flow is from left to right.

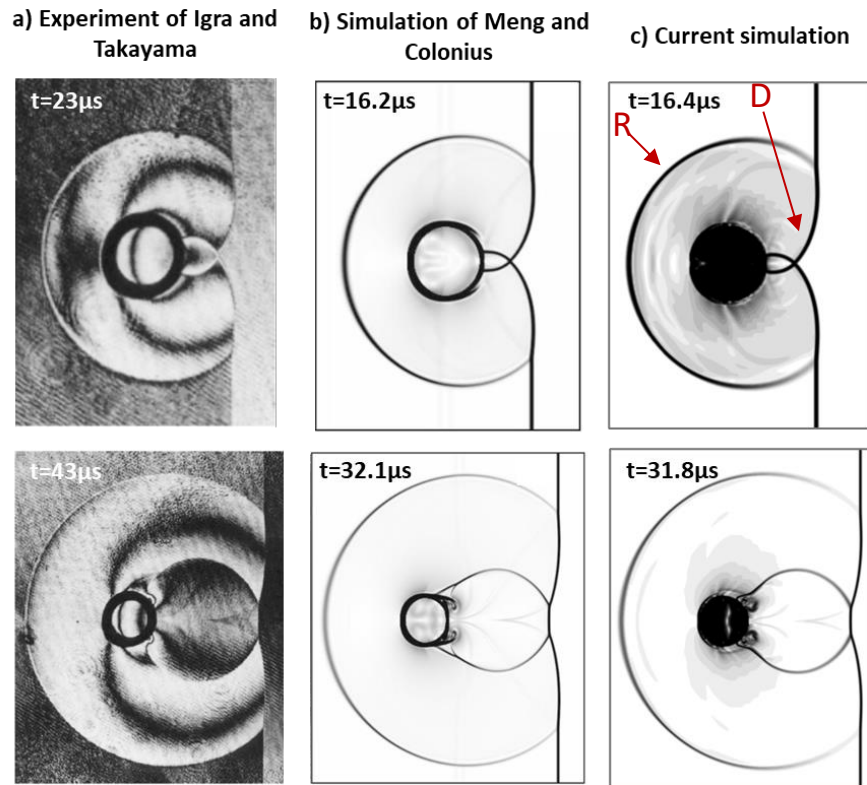


Figure 3-15: a) Holographic interferograms from the experiment of Igra and Takayama [142] and numerical schlieren images from the simulations of b) Meng and Colonius [139] and c) the current study, at two time instances. Flow is from left to right.

3.3.3.2 Results on droplet quantities

Figure 3-16 presents the temporal evolution of the non-dimensional streamwise and cross-stream deformation, as well as the leading-edge displacement of the droplet, as predicted by the experiment of [142], the simulation of [139] and the simulation of the current work ($\sigma=0.5$). As the droplet deforms into an ellipsoid shape, the streamwise deformation gradually decreases with time, while the cross-stream one increases. The leading-edge displacement increases as the droplet moves in the streamwise direction. There is a good agreement between the results of both simulations and the experiment for the streamwise deformation and leading-edge displacement, while a discrepancy is observed with the experiments for the cross-stream deformation.

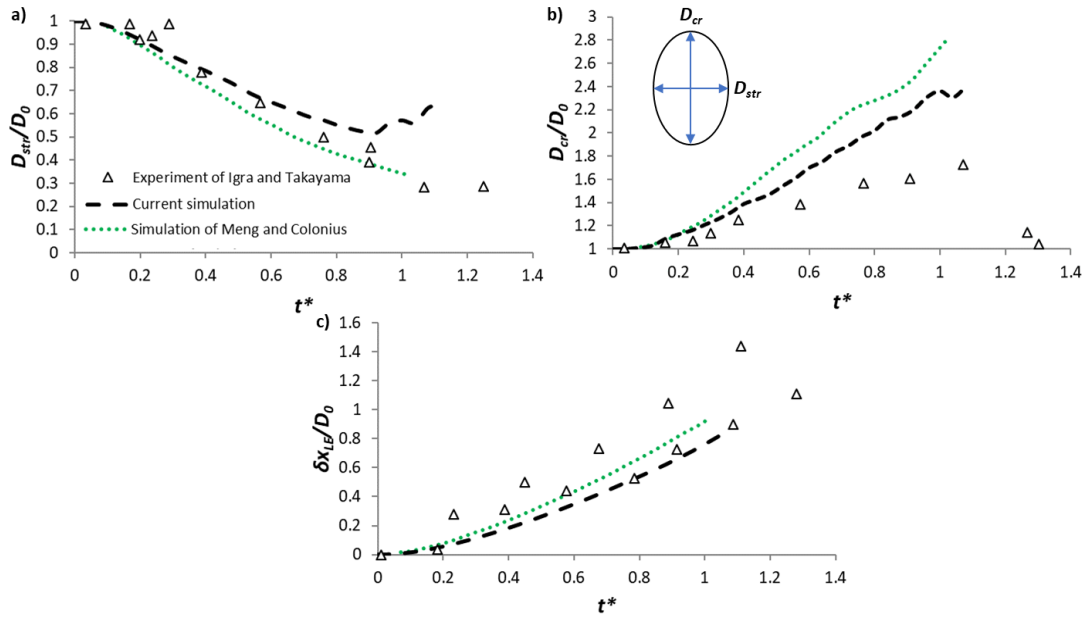


Figure 3-16: Temporal evolution of the non-dimensional a) streamwise deformation, b) cross-stream deformation and c) leading-edge displacement of the droplet, as predicted by the experiment of [142], the simulation of [139] and the simulation of the current work ($a=0.5$).

3.3.4 Conclusions

For the validation of the droplet breakup model for high Ma numbers a 2-D planar simulation has been performed with a water droplet exposed to an air flow of $Ma=1.43$. The results of the simulation are compared against published experimental [142] and numerical [139] data, and good qualitative agreement is observed for the pressure and numerical Schlieren contours. In addition, the quantitative results for the streamwise deformation and the leading-edge displacement are also in good agreement; a discrepancy with the experiments is observed for the cross-stream deformation, which, however, is close to the results from the simulation of [139]. The validated model is utilized in Chapter 4 for the 3-D simulation of a water droplet exposed to an air flow of $Ma=1.23$.

Chapter 4

Isolated droplet breakup

4.1 Introduction

The validated numerical model of droplet breakup is utilized in this chapter to examine the breakup of isolated droplets. Initially, a parametric study of Oh and ε numbers is performed for Diesel and heavy fuel oil (HFO) droplets at low Ma numbers. It follows the breakup of a water droplet exposed to a high Ma number and the results are compared against previous experimental and numerical data.

4.2 Low Mach number simulations

4.2.1 Computational setup and examined conditions

The low Ma number simulations have been performed with the 2-D axisymmetric domain of Figure 3-1a (section 3.2.1). The conditions of the simulated cases are presented in Table 4.1. The fuel properties are based on published experimental data [18, 97], while the ambient gas properties range from atmospheric ($P=1\text{bar}$ and $T=298\text{K}$) up to those encountered in Diesel engines (i.e. $P=30\text{-}10\text{bar}$ and $T_g=780\text{-}1100\text{K}$). The examined We numbers range from 14 up to 279, the Oh numbers from 0.011 to 1.525, the density ratio from 5 to 816 and the Ma number is below 0.3.

Table 4.1: Examined cases for the parametric study of isolated droplet breakup.

Case	Fuel	D_o [μm]	P [bar]	We	Re	Oh	ε	Ma	Breakup mode	Examined parameter
1	Diesel	2324	30	14	2362	0.011	72	0.01	Bag	} Oh at $We=14$
2	HFO	125	30	14	667	0.965	72	0.04	Deformation	
3	HFO	50	30	14	422	1.525	72	0.07	Deformation	
4	Diesel	195	30	54	1343	0.038	72	0.06	Sheet-thinning	} Oh at $We=54$
5	HFO	125	30	54	1310	0.965	72	0.13	Deformation	
6	HFO	50	30	54	828	1.525	72	0.14	Deformation	} Oh at $We=254$
7	Diesel	195	30	254	2912	0.038	72	0.18	Sheet-thinning	
8	HFO	125	30	254	2841	0.965	72	0.29	Sheet-thinning	
9	HFO	50	30	254	1797	1.525	72	0.29	Sheet-thinning	} ε at $We=54$
10	HFO	125	1	54	769	0.965	816	0.45	Bag	
11	HFO	50	1	54	486	1.525	816	0.03	Bag	

12	HFO	125	100	14	830	0.965	30	0.06	Deformation	} ε at $Oh=0.96$
13	HFO	125	100	54	1630	0.965	30	0.12	Deformation	
14	HFO	125	100	254	3536	0.965	30	0.13	Sheet-thinning	
15	Diesel	184	146	270	21503	0.039	5	0.02	Sheet-thinning	} ε at $Oh=0.039$
16	Diesel	184	73	270	15205	0.039	10	0.04	Sheet-thinning	
17	Diesel	184	24	270	9297	0.039	30	0.05	Sheet-thinning	
18	Diesel	184	9.2	264	5761	0.039	79	0.09	Sheet-thinning	
19	Diesel	184	6.4	265	4829	0.039	112	0.18	Sheet-thinning	
20	Diesel	184	3.7	266	3688	0.039	195	0.24	Sheet-thinning	
21	Diesel	184	1	279	1920	0.039	700	0.02	Sheet-thinning	

4.2.2 CFD results

4.2.2.1 Parametric study of Oh number

4.2.2.1.1 Effect of Oh number on the breakup mode

Starting with a low density ratio of 72, the effect of increasing Oh number on the droplet deformation is highlighted for three We numbers (14, 54 and 254). The temporal evolution of droplet shape for these conditions is presented in Figure 4-1. For the We numbers of 14 and 54, the increase of Oh number from less than 0.04 to 0.96, and further to 1.53 leads to the change of the bag breakup mode for low Oh to a non-breakup oscillatory deformation for higher Oh numbers. For the We number of 14, this transition is in accordance with the boundaries proposed by Hsiang and Faeth [15] (Figure 1-6a), while for $We=54$ a bag breakup mode should have been predicted instead of the deformation. Nevertheless, the boundaries between the different breakup modes in Figure 1-6a have been developed for high density ratios (>580), while in the current simulations the density ratio is equal to 72. Such differences are further discussed in the next section, where the effect of density ratio on the breakup mode is investigated. Turning now to the examination of cases with We number equal to 254, it is observed in Figure 4-1 that the increase of Oh number does not affect the breakup mode, which remains sheet-thinning for all the examined Oh numbers, in agreement with Hsiang and Faeth [15]. The temporal evolution of droplet shape for the Oh number of 1.53 shows that before the onset of breakup a portion of the liquid mass is concentrated at the center of the droplet similar to the bag-stamen breakup mode [25], probably due to the high viscosity of HFO.

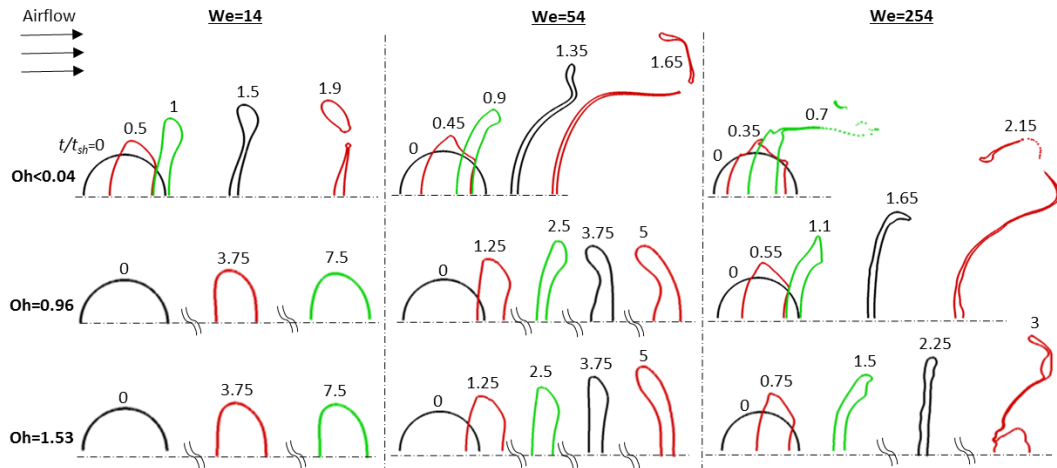


Figure 4-1: Temporal evolution of droplet shape for three We numbers and three Oh numbers ($\epsilon=72$).

4.2.2.1.2 Effect of Oh number on the droplet deformation, liquid surface area and drag coefficient

Turning now to the quantitative effect of Oh number on the breakup process, its effect on the parameters of droplet deformation, drag coefficient and liquid surface area is investigated. Figure 4-2 presents the temporal evolution of the droplet deformation for three Oh numbers (0.038, 0.96 and 1.53) and two We - ϵ combinations, i.e (a) 54-694 and (b) 254-72. The streamwise (D_{str}) and cross-stream (D_{cr}) deformations follow the same trend as in the validation section (3.2.3), i.e. the streamwise deformation initially decreases due to drop flattening, followed by an increase owed to the formation of the bag or sheet, while the cross-stream one increases during the whole duration of the process. The increase of Oh number results in a lower deformation rate, in accordance with the experiments of [11] and the numerical studies of [26], [28], [7] and [30].

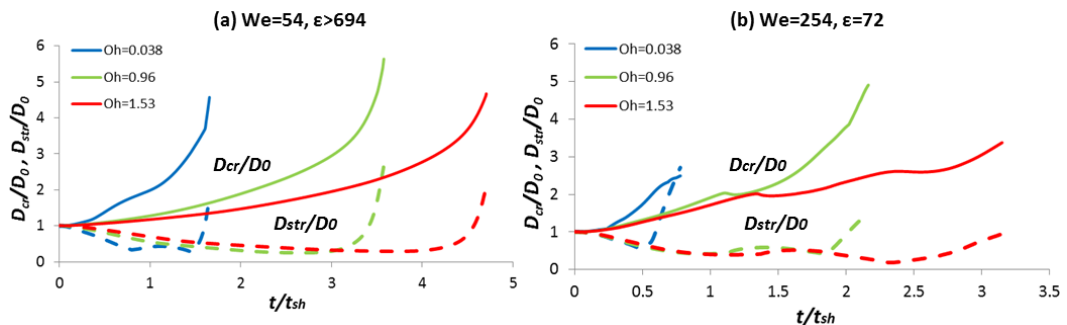


Figure 4-2: Temporal evolution of both main axes deformations (D_{cr} , D_{str}) for three Oh numbers and a) $We=54$ and $\epsilon>694$, and b) $We=254$ and $\epsilon=72$. The solid lines correspond to the cross-stream deformation and the dashed ones to the stream-wise one.

One quantity that is important for spray applications and is difficult to be measured experimentally is the surface area of the droplet. This is calculated in the CFD simulations as $S = \sum_i^{ncells} V_{cell} |\nabla \alpha|$, which has been utilized also in [8, 132, 146, 147] and is derived using the divergence theorem (or Gauss theorem) for the volume fraction at the interface cells. The temporal evolution of the liquid surface area for the conditions of Figure 4-2 is presented in Figure 4-3. Initially, an almost linear increase of the dimensionless liquid surface area is predicted during the drop flattening, followed by a steep increase owed to the formation of the bag. For the higher We number cases, as depicted in Figure 4-3b, a smoother increase rate is observed, as a liquid sheet is formed instead of a bag. Generally, the liquid surface area increases several times by the onset of breakup. Similar to the rate of drop deformation, the increase rate of liquid surface area also decreases with increasing Oh number.

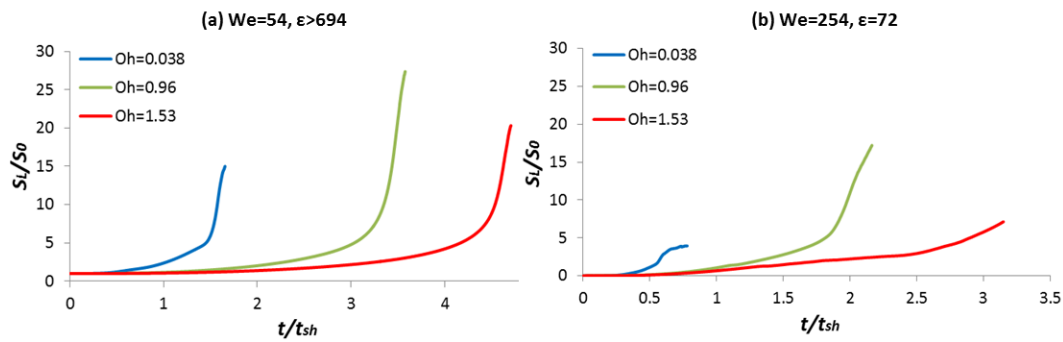


Figure 4-3: Temporal evolution of liquid surface area for three Oh numbers and a) $We=54$ and $\epsilon>694$, and b) $We=254$ and $\epsilon=72$.

Another parameter, that is useful in spray codes following Lagrangian approach to simulate the spray evolution, is the droplet's drag coefficient (C_d); this can be calculated with the aid of the droplet momentum equation:

$$m \frac{d}{dt} (U_d(t)) = \frac{1}{2} C_d(t) \rho_g U_{rel}^2(t) A_f(t) \quad (4-1)$$

The left hand side of eq.(4-1) is the rate of droplet momentum change and the right hand side is the drag force exerted on it. The terms representing the effect of gravity, virtual mass, pressure and stress forces have been neglected (since $\rho_g/\rho_l \ll 1$) [72], while the effect of Basset force has been incorporated into the drag coefficient (pertaining to an effective drag coefficient), similar to previous numerical studies [28, 31, 33, 148]. The

droplet velocity is the volumetric averaged one. By rearranging equation (4-1) and using the expressions for droplet mass m and relative velocity U_{rel} , as well as the definition of density ratio (eq. (1-1)), we get the final expression for C_d in eq. (4-2):

$$C_d(t) = \frac{\frac{4}{3} D_0 \varepsilon \frac{dU_d(t)}{dt} \frac{A_f(0)}{A_f(t)}}{(U_g - U_d(t))^2} \quad (4-2)$$

The drag coefficient changes in time as the droplet-gas relative velocity decreases and the droplet shape changes from spherical to a disk-like. The temporal variation of the drag coefficient is presented in Figure 4-4 for three cases with $We=54$, $\varepsilon>694$ and Oh numbers equal to 0.038, 0.96 and 1.53. In all cases the C_d at the beginning of the simulation reaches very high values, owed to the highly unstable flow field during this period, followed by a steep decrease similar to the findings of [7, 30]. During the rest of the process the drag coefficient increases steadily due to droplet acceleration up to the point of breakup initiation, where it decreases abruptly as also found in [30]. Moreover, from the same figure it is observed that as the Oh number increases the drag coefficient decreases, in agreement with the findings of [7, 28]. Given that the breakup mode is the same for all cases (bag breakup) and that the rate of deformation is higher for lower Oh numbers, the cases with smaller Oh numbers deform faster into oblate shapes (disk-like); these shapes result in higher accelerations and drag coefficients.

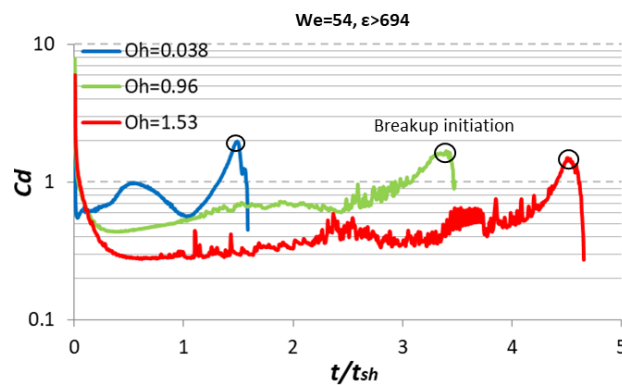


Figure 4-4: Temporal evolution of drag coefficient for three cases with $We=54$, $\varepsilon>694$ and three Oh numbers.

The parametric study of Oh number reveals that the less viscous fuels (e.g. Diesel over HFO in this study) promote the breakup process as the rate of deformation, liquid surface area and drag coefficient are larger than those of the viscous fuels (e.g. HFO).

4.2.2.2 Parametric study of ϵ

4.2.2.2.1 Effect of ϵ on the breakup mode

For the We number of 54 the breakup of HFO droplets is further investigated under atmospheric conditions in order to examine the effect of density ratio on the breakup mode. In Figure 4-5 the temporal evolution of droplet shape is presented for $Oh=0.96$ and two density ratios of 72 and 816. It is observed that the single change in density ratio from 72 to 816 resulted in the change of the breakup mode from deformation to multi-bag. This is in accordance with the findings of Aalburg [27], who stated that the critical We number increases with decreasing density ratio. Although Aalburg [27] found that the change of the critical We number is significant when the density ratio is below 32, the examined cases are very close to the boundaries of the breakup regime and this can affect the breakup mode.

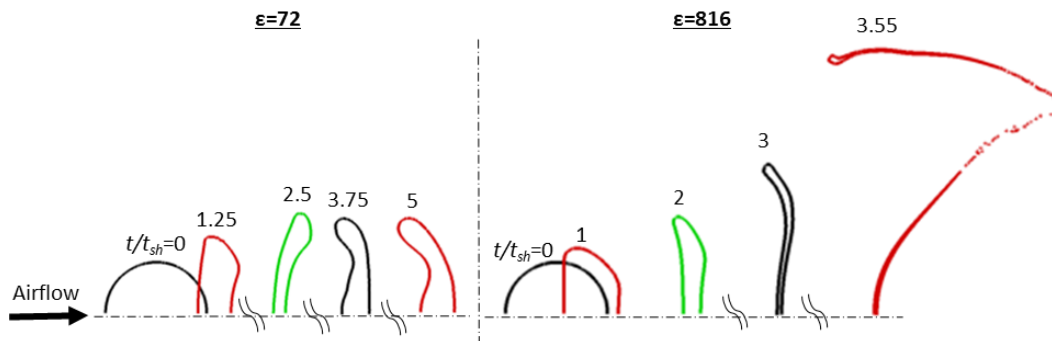


Figure 4-5: Temporal evolution of droplet shape for $We=54$, $Oh=0.96$ and two density ratios.

4.2.2.2.2 Effect of ϵ on the liquid surface area and drag coefficient

Figure 4-6 presents the temporal evolution of liquid surface area for seven cases with density ratios ranging from 5 up to 700 and close We numbers (264 up to 279). After a short non-deforming period ($0.25t_{ref}$), the liquid surface area starts to increase. Up to the point of breakup initiation the liquid surface is not affected much by the density ratio, while after that point a small deviation appears; nevertheless, the 2-D axisymmetric solution is not reliable after the breakup initiation, since 3-D effects become important.

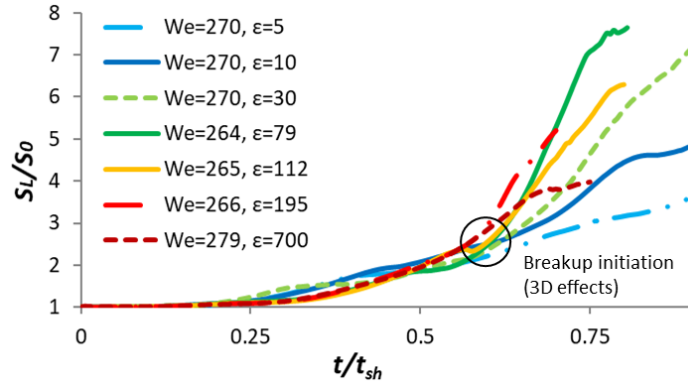


Figure 4-6: Temporal evolution of liquid surface area for seven cases with density ratios ranging from 5 up to 700 and close We numbers (264 up to 279).

In order to assess the effect of density ratio on the drag coefficient the temporal evolution of drag coefficient, calculated using eq. (4-2), is presented in Figure 4-7a for three cases with $\epsilon=10$ (representative case for low density ratios), $\epsilon=112$ (representative case for moderate density ratios) and $\epsilon=700$ (representative case for high density ratios); their We numbers are close in the range of 265 to 279. The drag coefficient starts from a value close to 0.4, which is the drag coefficient of solid spheres with Re number in the range 2000-20000 [134], and increases with time reaching values close to 1.17, which is the drag coefficient of solid disks with $Re>100$ [134]. In addition, it is observed that the overall drag coefficient increases with decreasing density ratio. This trend can be explained by examining each term of eq. (4-2) separately: D_o is the same for all cases, $A_{f,o}/A_f$ is almost constant in all cases due to similar droplet shape, and the term U_d is small compared to U_g for high We numbers, so it can be ignored. Therefore, the ratio $\epsilon/U_g=\rho_l/(\rho_g U_g^2)$ appearing in the equation, which is constant for constant We number, results in making the term $dU_d(t)/dt$ for droplet acceleration the one that is the most influential among all, when changing the density ratio. The droplet acceleration is larger for lower density ratios (relatively lighter drops accelerate faster), thus making the drag coefficient higher as well. This is in agreement with the numerical study of [31], in which they state that generally a lower density ratio results in a higher drag coefficient.

Due to the short duration of the phenomenon it is interesting to examine the time-averaged drag coefficient for each case (calculated as the area under the curve of Figure 4-7a divided by the breakup time). This is shown as a function of the Re number in Figure 4-7b for selected cases of Table 3.2 and Table 4.1 in the three breakup modes: bag, multi-bag and sheet-thinning. The drag coefficient for all cases lies within the one of disk (purple

dotted line) and the one of sphere (blue line) as taken from [134]. Again, we notice the same trend for the drag coefficient, which increases with decreasing density ratio.

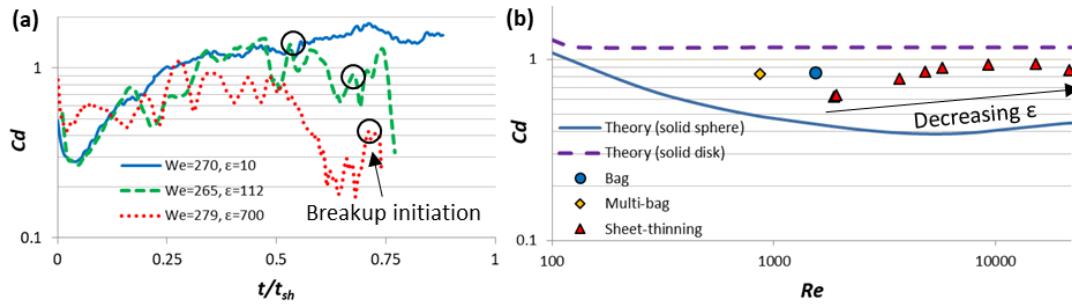


Figure 4-7: a) Temporal evolution of drag coefficient for three cases with $\epsilon=10$, 112 and 700, and b) time-averaged drag coefficient as function of Re for various cases in the three breakup modes: bag, multi-bag and sheet-thinning.

4.2.2.3 Correlations for the prediction of droplet quantities

In all examined cases the increase of Oh number resulted in an increase of the breakup initiation time (or even ceased breakup) in agreement with the experimental study of Hirahara and Kawahashi [149]. In Strotos et al. [119] the breakup initiation time was correlated as a function of We and Re numbers (valid for low Oh and high ϵ numbers). Based on the results of the present parametric study, two additional correction factors are proposed, which account also for the effect of ϵ and Oh numbers, apart from those of We and Re ; the resulting equation is eq.(4-3). The term of Oh was inspired by the correlations of Gel'fand et al. [13] and Pilch and Erdman [38], and is extracted following a best-fitting procedure for the conditions of cases presented in Table 3.2 and Table 4.1, and two additional cases (with $Oh=0.2$ and $Oh=3$ which are not presented in the current work). The predicted term has the same general form as in Gel'fand et al. [13] i.e. $(1+A \cdot Oh^B)$, with A and B constants. An updated version of this correlation can be found in [150].

$$\frac{t_{init}}{t_{sh}} = 8.95 \cdot (We^{-0.352} Re^{-0.086}) \cdot \left(\frac{1}{1 + \epsilon^{-0.5}} \right) \cdot (1 + 2.36 Oh^{0.93}) \quad (4-3)$$

The predicted breakup initiation times from equation (4-3) are shown in Figure 4-8 along with the actual times calculated from the simulations for the whole range of examined conditions in this paper and the publications of [128] (Diesel), [114] (n-heptane) and [119] (n-decane). In addition, the lines for $\pm 20\%$ deviation are also presented. In

almost all cases the predicted breakup initiation times from equation (4-3) lie within a maximum deviation of 20% from the corresponding ones of the simulations.

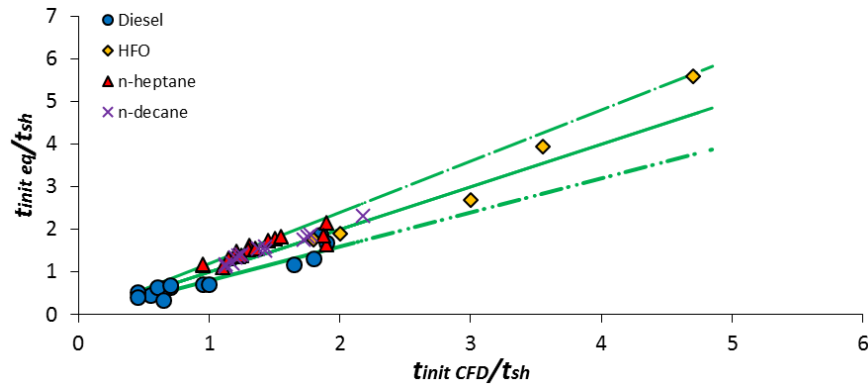


Figure 4-8: Breakup initiation time as predicted by eq. (4-3) (data points) and the simulations (straight lines).

Turning now to the drag coefficient of an isolated droplet, this can be estimated as function of the We number using equation (4-4), similar to [148]. In the current simulations the Re number is a unilateral function of We (for a single We there is only one existing Re) so equation (2-6) can be written also as function of Re .

$$\overline{C_d} = c_1 \cdot We^{-c_2} \quad (4-4)$$

, with $c_1=4$ and $c_2=0.41$ found by fitting the results of the simulations of section 5.2 (isolated droplets) with a mean absolute error equal to 8.6%.

In Figure 4-9, the drag coefficient is presented as function of the Re number for the solid disk [134], solid sphere [134] as well as for deforming droplets calculated by the CFD simulations and correlation (4-4). The predicted drag coefficients lie within the one of solid sphere (initial droplet shape) and the one of solid disk (deformed droplet shape) for the majority of the examined cases. In addition, both decrease with the Re number in agreement with that of solid sphere.

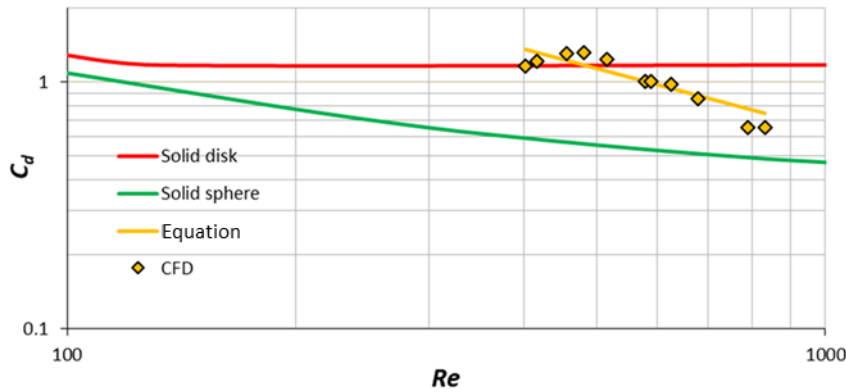


Figure 4-9: Drag coefficient as function of Re number for solid sphere, solid disk and for deforming droplets calculated by the CFD simulations and correlation (2-6).

Finally, regarding the prediction of liquid surface area and critical We number correlations were proposed in [119] and [150], respectively, and the reader is referred to these works for more details.

4.2.2.4 Conclusions

The breakup of isolated Diesel and HFO droplets exposed to an air flow was investigated for We numbers in the range of 15 up to 350, Oh numbers up to 1.525 and density ratios from 5 up to 816. With the increase of Oh number from 0.04 to 1.53 the bag and multi-bag breakup modes were altered into oscillatory deformation without breakup, while the sheet-thinning regime remained unchanged. In addition, the increase of Oh number resulted in a decrease in the rate of deformation, liquid surface area and drag coefficient, while the breakup initiation time increases, meaning that the breakup process is hindered when using high viscous fuels such as HFO. Regarding the parametric study of ϵ , it was observed that changing the density ratio from 72 to 816 resulted in the alternation of the breakup mode from deformation to bag breakup. Moreover, the temporal evolution of liquid surface area remained unaffected by the change of ϵ , while the drag coefficient decreased with the increase of ϵ . Based on these results, correlations were proposed for the prediction of breakup initiation time and drag coefficient of an isolated droplet as function of the non-dimensional numbers.

4.3 High Mach number simulation

4.3.1 Computational setup and examined conditions

Apart from the well-known 3-D flow features appearing in the aerobreakup of droplets, such as surface instabilities, vortex shedding and formation of liquid sheets [52, 54, 55], a 3-D simulation is necessary in order to apply the VOF-to-DPM model of FLUENT, which tracks the particles in 3-dimensions following the Lagrangian approach [106]. Figure 4-10 illustrates the 3-D computational domain that is utilized for the simulation of droplet breakup at high Ma number. At the top and right of the domain pressure outlet boundary conditions are applied, while at its left there is a pressure inlet. Only $1/8$ of the droplet is simulated (45°), while periodic boundary conditions are applied at the front and back of the domain to simulate the whole droplet. The shock wave is initialized as a step change in the temperature and pressure located at a distance of $1D_0$ from the center of the droplet. In order to introduce some necessary randomness in the process, the field is initialized with a small “random” instantaneous velocity ($<1/100U_{sh}$), which is calculated based on the turbulent kinetic energy estimated from the κ - ϵ model of FLUENT. The grid cell have a wedge like shape (similar to that of the domain) and is created using the 2-D grid of section 3.3 revolved around the X axis (36 partitions in total); this gives a resolution at the interface close to 50cpR and a total cell number equal to 11.34 million cells. The convective Courant number is equal to 0.5, while the acoustic is 7.85; preliminary 2-D runs have shown that the temporal evolution of droplet shape and velocity do not change much when a smaller time step is used ($Cou_{acoustic}<1$), therefore saving a lot of computational time in the current 3-D simulation. The spatial discretization of the VOF equation is done using the geo-reconstruct scheme (sharp interface) in contrast to the more diffusive schemes used in the simulation of water column, due to restrictions of the VOF-to-DPM model of FLUENT [106].

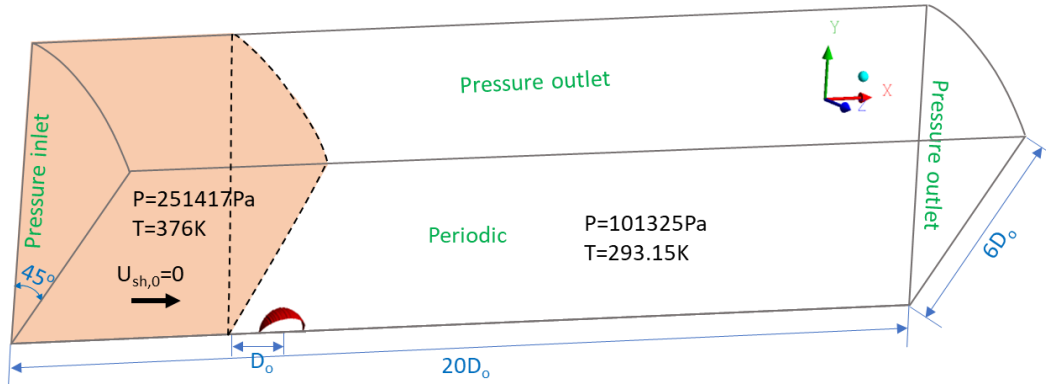


Figure 4-10: 3-D computational domain utilized for the simulation of droplet breakup at high Ma number.

The liquid droplet is water, while the surrounding gas is nitrogen with properties calculated as described in section 2.1.2; the diameter of the droplet is based on [34]. The resulting non-dimensional numbers are calculated based on the post-shock properties and are presented in Table 4.2.

Table 4.2: Droplet diameter and non-dimensional numbers of the 3-D simulation of droplet breakup at high Ma number.

D_0 (m)	We	Re	Oh	ϵ	Ma
$2.4 \cdot 10^{-3}$	780	191169	0.0024	617	1.24

4.3.2 CFD results

4.3.2.1 Description of fluid flow

Figure 4-11 illustrates the temporal evolution of droplet deformation as predicted by the experiment of Theofanous et al. [34], the simulation of Meng and Colonius [52] and the simulation of the current work. It should be noted that the conditions of this work and those of the experiment are identical, while in the simulation of [52], the Ma is equal to 1.47 instead of 1.23. Also, the shape in the simulation of [52] corresponds to the VOF iso-value of 0.01, while in the current work the iso-value of 0.5 is presented. The exact time of the experimental images is not known since they originate from a video, while the corresponding ones from the simulations have been chosen to best match those of the experiments.

Similar to the 2-D simulations (section 3.3.3.1), the droplet initially deforms into a mushroom-like shape ($t^*=0.274$ and $t^*=0.314$ in the simulation of this work), followed by a disk-like shape ($t^*=0.634$). However, their main difference lies in the breakup initiation

time, which is much faster for the 3-D simulation, since micro-droplets are stripped from its periphery as early as $t^*=0.274$. This is attributed to the high velocities at the periphery of the droplet, as shown in Figure 4-12, which presents in the X-Y plane ($Z=0$) the contour of non-dimensional velocity magnitude ($U_{mag}^*=U_{mag}/U_{sh}$) and pressure ($P^*=P/P_{sh}$) at different time instances. The maximum value of the velocity is equal to 1.5, in agreement with the potential flow theory and the simulation of [52]. The liquid stripping continues until a large part of the parent droplet has been converted into micro-mist ($t^*=0.634$), something that is also visible in the experiment of [34], while it is not present in the simulation of [52]. The diameter of these micro-droplets ranges from approximately 25 μm up to 52 μm , which corresponds to the volume equivalent droplet diameter of an interface cell, and it is an input for the model. Nevertheless, in the simulation micro-droplets appear also at the core of the droplet, owing to a cyclical protuberance at the front of the droplet, appearing at $t^*=0.234$ and remaining up to $t^*=0.634$. The latter is attributed to the waves that appear at the surface of the droplet, due to the interaction with the shock wave (Kelvin-Helmholtz and Rayleigh-Taylor instabilities [34]), as shown in the pressure contour of Figure 4-12: at the time instance of $t^*=0.234$, the pressure is higher at the outer part of the droplet compared to its core, which is the case for the rest of the images, therefore creating the aforementioned protuberance. This is also present in the experiments, starting from the image corresponding to $t^*=0.314$ simulation time and being more visible at $t^*=0.634$, but to a lesser extent. Finally, “wrinkles” appear at the surface of the droplet visible in the simulation at the time instance of $t^*=0.234$, which are also present in the experiments, but, again, to a lesser extent.

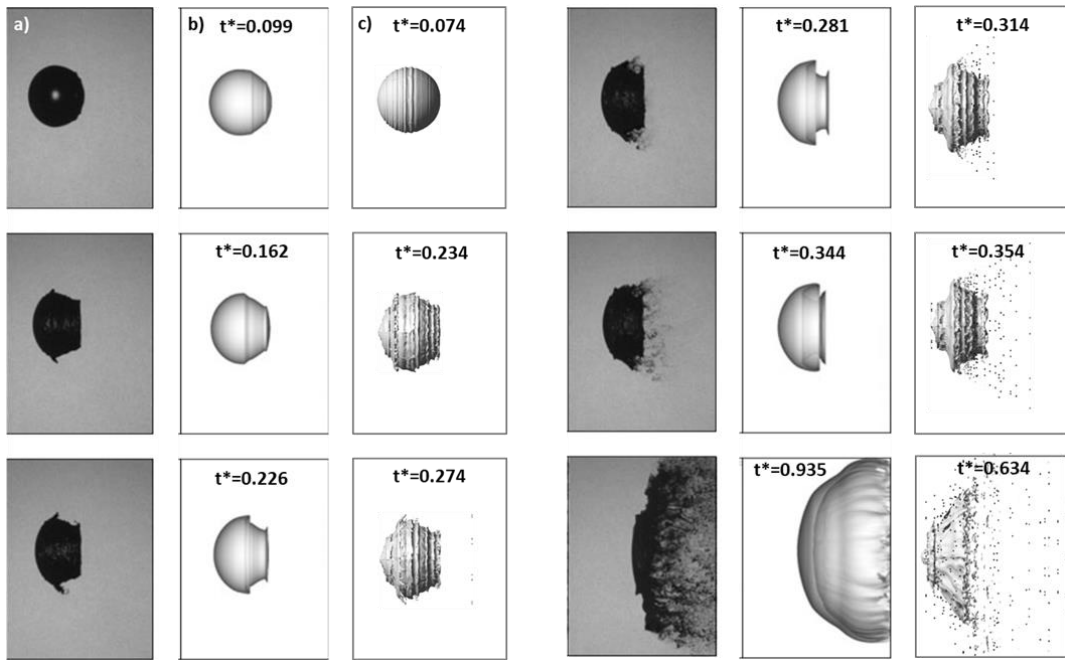


Figure 4-11: Temporal evolution of droplet deformation as predicted by a) the experiment of [34], b) the simulation of [52] ($\alpha=0.01$) and c) the simulation of the current work ($\alpha=0.5$). Flow is from left to right.

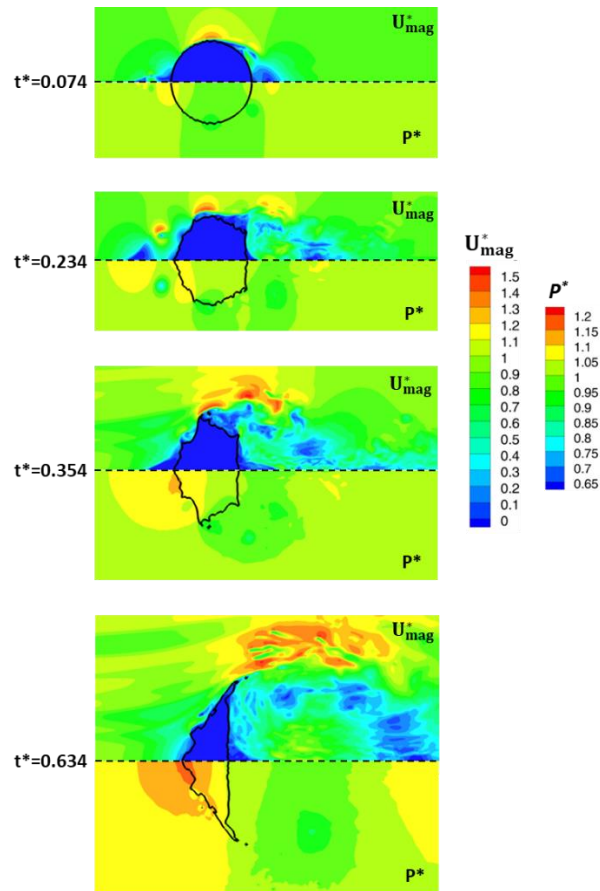


Figure 4-12: Contours in the X-Y plane ($Z=0$) of the non-dimensional velocity (top) and pressure (bottom) from the simulation of shock-wave induced droplet breakup. Flow is from left to right.

4.3.2.2 Results on droplet quantities

Figure 4-14 illustrates the temporal evolution of the dimensionless droplet velocity, displacement and acceleration, as well as the unsteady drag coefficient, as calculated in the current work and in the simulation of [52]. The unsteady drag coefficient is calculated using the momentum balance on the droplet and is given in equation (4-5). The droplet frontal area is calculated by assuming a circular area based on the droplet's deformed diameter D_{cr} (assumed equal to D_z), similar to [52].

$$C_d(t) = \frac{\frac{4}{3} D_0 \varepsilon \frac{dU_d(t)}{dt} \frac{A_f(0)}{A_f(t)}}{(U_{sh} - U_d(t))^2} \quad (4-5)$$

Both the velocity and the displacement of the droplet increase with an exponential fashion as the shock wave and the gas flow behind it crosses the droplet and causes it to move. The droplet acceleration starts from a high value and decreases abruptly at the initial stages of the simulation due to the unsteady flow field, while it increases gradually as the droplet accelerates. The drag coefficient experiences a similar decline at the initial stages of the simulation; however, it increases only slightly followed by a decrease at the later stages of the simulation. This is attributed to the increase of the frontal area of the droplet ($A_f(t)/A_f(0)$) as it deforms in the cross-stream direction. The results from the simulation of [52] follow a similar trend, while being slightly higher compared to the simulations of this study, probably due to the higher Ma number (1.47 compared to 1.23).

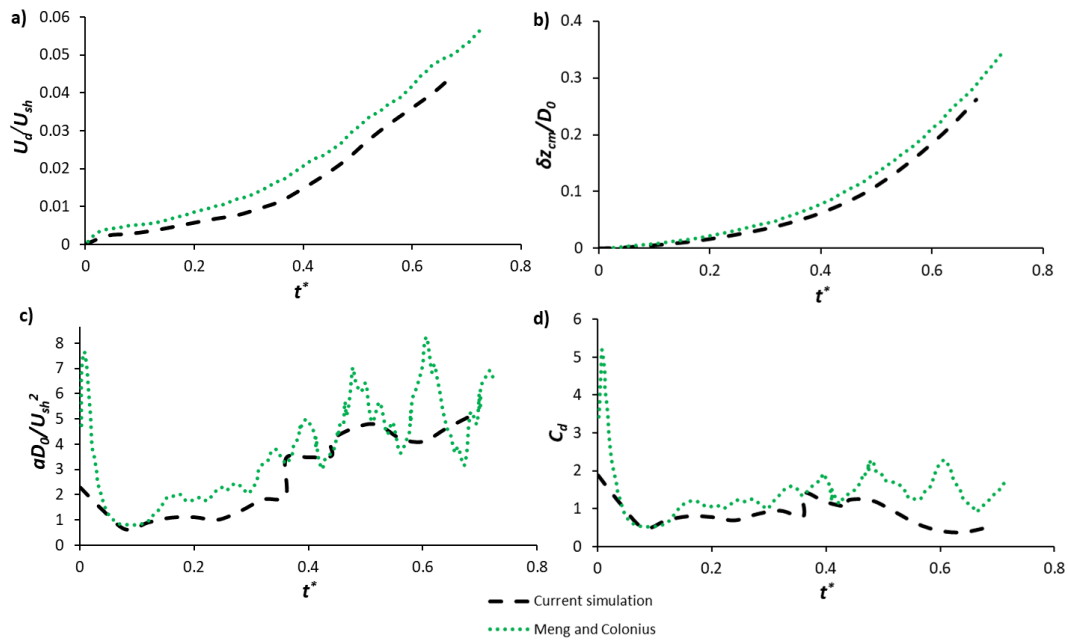


Figure 4-13: Temporal evolution of the dimensionless droplet a) velocity, b) displacement and c) acceleration, as well as d) the unsteady drag coefficient, as calculated in the current work and in the simulation of [52].

Finally, the temporal evolution of droplet deformation in both axes (streamwise and cross-stream) and surface area are presented in Figure 4-14. The cross-stream deformation and surface area increase as the droplet takes an ellipsoid shape, while the streamwise deformation decreases followed by a slight increase at the final stages of the simulation; this is attributed to the liquid sheets formed at the periphery of the droplet (Figure 4-11 at $t^*=0.634$), which are also reported in the works of [52, 54]. The fluctuation in the value of cross-stream deformation at the time instance of approximately 0.5 is attributed to the stripping of the micro-droplets from its periphery, something that results in the decrease of the size of the parent droplet.

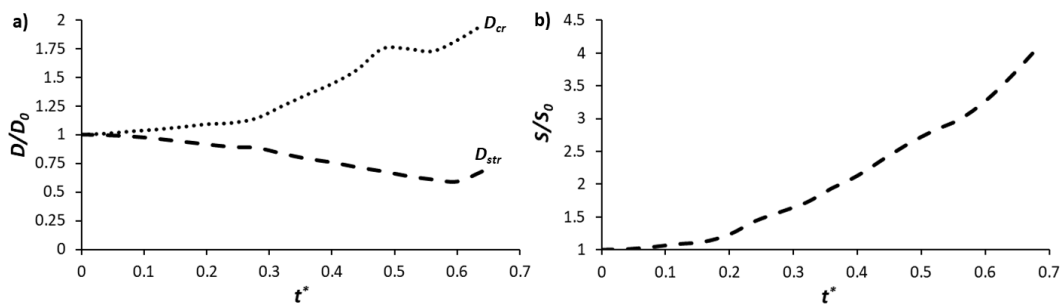


Figure 4-14: Temporal evolution of droplet a) deformation in both axes (streamwise and cross-stream) and b) surface area.

4.3.2.3 Conclusions

A 3-D simulation was performed with a water droplet exposed to an air flow of $Ma=1.23$, using the VOF-to-DPM model of FLUENT [106], to model the micro-droplets that are stripped from the main droplet. This model converts the VOF solution to Lagrangian particles, when certain user-defined criteria are met. The predicted temporal evolution of droplet shape was similar to that predicted by the simulation of [52] and the experiments of [34]. The appearance of micro-droplets is observed for the first time in CFD simulations, according to the authors' best knowledge, which are present also in the experiment of [34]. Nevertheless, the diameter of these droplets is affected by the user-defined inputs and is not a product of the solution process. Moreover, close results between the two simulations were observed also for the droplet quantities of displacement, velocity, acceleration and drag coefficient. Finally, results for the droplet deformation and surface area were presented for the first time in the current study; a steady increase in the surface area and cross-stream deformation was observed, as the drop takes an ellipsoid shape, while the streamwise deformation initially decreases followed by an increase at the later stages of the simulations, due to the formation of liquid sheets at the periphery of the droplet.

Chapter 5

Cluster droplet breakup

5.1 Introduction

This chapter focuses on the investigation of droplet clusters in various formations. First, four droplets in tandem formation are examined, i.e. one behind the other with respect to the air flow, it follows the investigation of an infinite sheet of droplets moving in parallel to the air flow, called single-sheet cluster, and, finally, a combination of the two is investigated, called multi-sheet cluster, in which four infinite droplet sheets are moving in parallel to the air flow. Results are presented for the effect of distance between the droplets at various We numbers on the breakup mode and on key droplet quantities, such as the breakup time and drag coefficient. Finally, correlations are proposed to predict these quantities as function of the We number and the non-dimensional distance between the droplets for the case of tandem formation.

5.2 Tandem formation

5.2.1 Computational setup and examined conditions

The simulations of droplet clusters have been performed at conditions representative for Diesel engines, as shown in Table 5.1, along with the corresponding references used for their estimation. The resulting non-dimensional numbers from these conditions are: $Oh=0.05$, $\varepsilon=51$ and $N=37$.

Table 5.1: Representative Diesel engine conditions.

	D_o (μm)	P (bar)	T_g (K)	μ_g (kg/s·m)	ρ_g (kg/m ³)	T_L (K)	μ_L (kg/m·s)	ρ_L (kg/m ³)	σ (N/m)
Value	50	40	900	4E-05	15.48	335	0.0015	788.6	0.024
Reference	[7]	[151]	[151]	[105]	Ideal gas law	[151]	[152]	[152]	[120]

The 2-D axisymmetric domain that is utilized in the simulations of tandem droplet breakup is presented in Figure 5-1. The four droplets have an initial velocity $U_{d,0}$, while the air is stagnant (boundary condition for velocity inlet $U=0$); the mesh is moving with a

velocity equal to the average velocity of the droplets in order to ensure that they always lie within it. Preliminary CFD runs have shown that the movement of droplets in stagnant air is equivalent to the movement of air with initially still droplets. The droplets have been placed at an initial equal non-dimensional distance $L/D_0=2$, measured from the droplet centers; this distance changes between the runs in order to examine its effect on the process. The mesh is wide enough ($35D_0$) to accommodate all the examined distances. Focus is given on the third droplet of the row, which is called representative chain droplet (RCD). Preliminary runs with seven droplets ($L/D_0=2$, $We=40$) have shown that the quantities of the RCD in a seven-droplet chain differ less than 14% from those of the RCD in the four-droplet chain (Appendix A). These differences are expected to decrease at higher We numbers and larger L/D_0 . The simulation of four droplets is chosen in the current study instead of seven, because it is more suitable for parametric studies, since the computational cost for the simulation of seven droplets is increased by approximately 75% compared to that of four.

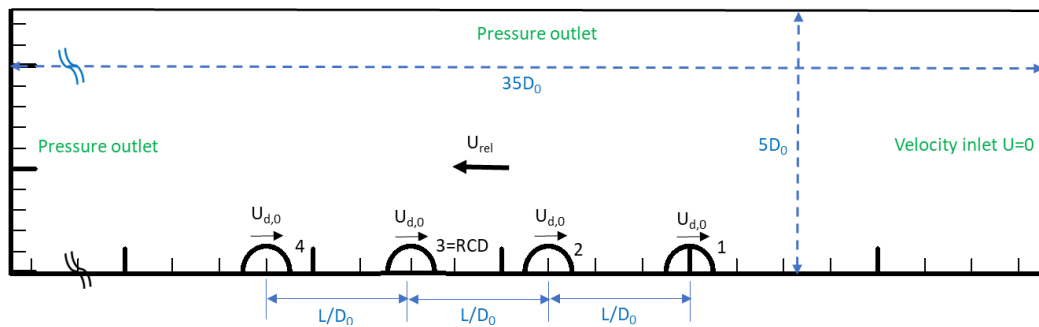


Figure 5-1: 2-D axisymmetric domain utilized in the simulations of tandem droplet breakup ($L/D_0=2$).

By changing the initial droplet velocity, the obtained We numbers range from 15 up to 64, while the Re number lies in the range of 402 to 860; it is to be noted that these conditions correspond to bag and multi-mode breakup modes for isolated droplets. The examined non-dimensional distances (L/D_0) range from 1.25 up to 20, resulting in 96 examined cases in total (see Figure 1-7). Finally, simulations have been performed also for an isolated droplet using the same computational domain and conditions in order to compare the results (11 simulations in total in the range of $We=15-64$). These simulations are utilized in section 5.2.2.3 to calculate the quantities of the isolated droplet, which are compared with those of the droplet in tandem formation.

5.2.2 CFD results

5.2.2.1 Droplet shapes

In Figure 5-2 the temporal evolution of the droplets' shape (denoted with the VOF iso-value of 0.5) is presented at different time instances for a representative case of droplet chain ($We=40$, $L/D_0=2$) along with the one of an isolated droplet at the same We number. The first observation is that the leading and isolated droplets exhibit a quite similar evolution of droplet shape and experience the same breakup mode (multi-bag), something that holds true for all the examined cases, as expected. Nevertheless, despite the similarity in droplet shapes, for small L/D_0 the drag coefficient of the leading droplet decreases up to 30% compared to the corresponding value of the isolated droplet, while the breakup initiation time and maximum surface area are slightly lower.

On the other hand, the shapes of the trailing droplets (no. 2, 3 and 4) after $t/t_{sh}=1.0$ start to deviate from those of the isolated droplet, as they are influenced by the presence of their upstream droplets. More specifically, their shapes are more deformed in the streamwise direction, which is due to the faster air flow (in terms of relative velocity) and higher pressure observed at their periphery compared to their center after $t/t_{sh}=1.0$, as indicated by the streamlines of Figure 5-2 and the contour of dimensionless pressure ($= (P - P_\infty)/\frac{1}{2}\rho_g U_{d,0}^2$) in Figure 5-3 ($We=40$, $L/D_0=2$). As a result, an oblique pressure gradient is developing, which tends to stretch the droplet towards a 45deg downstream direction; this alters their breakup mode in relevance to the one of the isolated droplet (multi-bag). This breakup mode has not been reported so far in the literature and it is termed here as "shuttlecock", as its shape resembles that of a shuttlecock ball used in Badminton. This was observed for We numbers in the range of 16 to 64 and droplet distances ranging from 1.25 to 4 (see Figure 5-6). When the distance between the droplets becomes large enough ($L/D_0>5$ for $We=40$) their shapes and breakup modes become similar to those of the isolated droplet (multi-bag), as it is shown in Figure 5-4. In addition, the trailing droplets move faster than the leading one (due to lower drag) and therefore get closer to it (especially evident for the first two droplets), which might result in their collision at subsequent time instances.

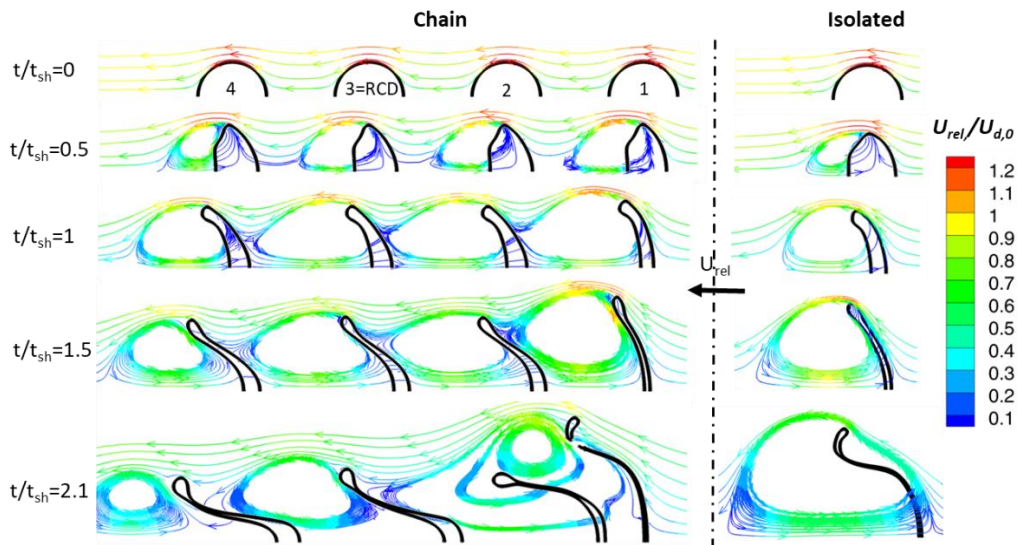


Figure 5-2: Temporal evolution of droplet shape for chain ($We=40$, $L/D_0=2$) and isolated ($We=40$) droplets (streamlines colored with the non-dimensional relative velocity magnitude).

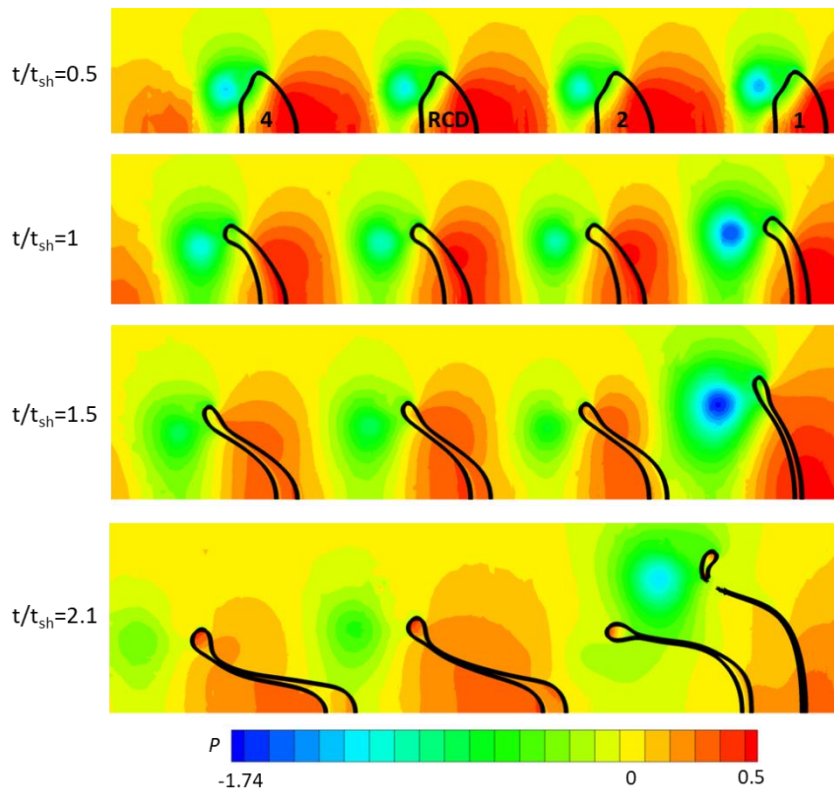


Figure 5-3: Dimensionless pressure contour for $We=40$ and $L/D_0=2$.

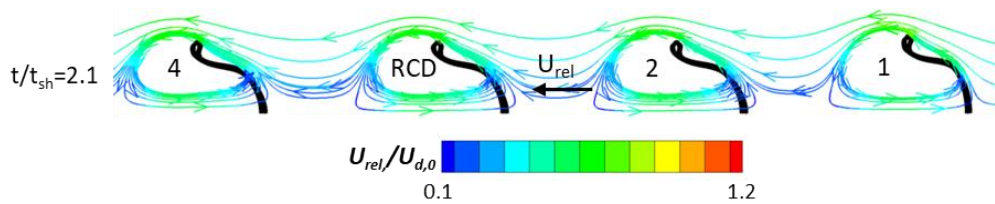


Figure 5-4: Snapshot of droplet shapes for $We=40$ and $L/D_0=5$.

For the same distance between the droplets ($L/D_0=2$), Figure 5-5 presents the temporal evolution of droplet shape of the representative chain and the isolated droplets for two We numbers (20 and 60). It is observed that for the low We of 20 the representative chain droplet deforms up to a maximum point and then reaches an elongated spheroid shape without breaking (Figure 5-5a). This elongated spheroid shape differs from the spherical shape reported in the literature for low We (oscillatory deformation) [4], since it is affected by the presence of the upstream droplets, which hinder the incoming air flow. For the same We number the isolated droplet experiences bag breakup mode. On the other hand, when the We number increases to 60, both the representative chain and the isolated droplets experience multi-bag breakup mode, as shown in Figure 5-5b, indicating that for high We numbers the effect of distance between the droplets is minimized and thus their deformation rates and shapes become independent.

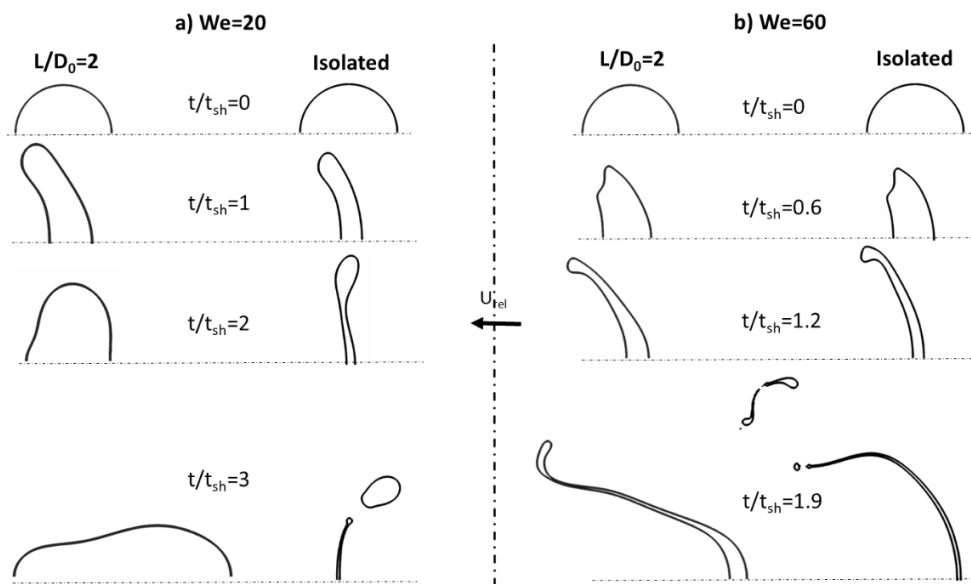


Figure 5-5: Temporal evolution of droplet shape for chain ($L/D_0=2$) and isolated droplets with a) $We=20$ and b) $We=60$.

5.2.2.2 Proposed correlations for the prediction of droplet quantities

The different quantities of the representative chain droplet (critical We , maximum surface area, breakup initiation time, drag coefficient and average deformation rate (see section 5.2.2.3.4)) can be calculated as a product of two terms: i) the value of the corresponding quantity of an isolated droplet at the same conditions (section 4.2.2.3), and ii) a correction factor that accounts for the interaction between the droplets. The

correction factor is a function of We and L/D_0 and is given in its general form in equation (5-1). The symbol φ denotes the respective examined quantity (S_{max}/S_0 , t_{br} , C_d) and the subscripts “ is ” and “ RCD ” stand for the isolated and representative chain droplets, respectively. The plus sign is used for the quantities that are higher compared to the corresponding values of an isolated droplet (such as t_{br}), while the minus one for those that are lower (such as S_{max}/S_0 and C_d). Only the correlation for the critical We is slightly different, as shown in (5-2). When the We and L/D_0 are large enough, the correction factor approaches unity, i.e. the two droplets have a similar behavior. Conversely, when the We and L/D_0 are small enough the correction factor approaches zero, i.e. the representative chain droplet is totally covered by its upstream droplet. The equation for the drag reduction due to L/D_0 is in agreement with the correlation proposed by [64], in which the ratio $C_{d,RCD}/C_{d,is}$ decreases with the inverse exponential of L/D_0 .

$$CF_{\varphi} = \frac{\varphi_{RCD}}{\varphi_{is}} = 1 \pm e^{-f(We, \frac{L}{D_0})} \quad (5-1)$$

With

$$f\left(We, \frac{L}{D_0}\right) = c_1 \cdot We^{c_2} \cdot \left(\frac{L}{D_0} - 1\right)^{c_3} \quad (5-1b)$$

$$CF_{We_{cr}} = \frac{We_{cr,RCD}}{We_{cr,is}} = 1 + c_1 \cdot \left(\frac{L}{D_0}\right)^{-c_2} \quad (5-2)$$

The coefficients c_1 , c_2 and c_3 appearing in equation (5-1) are found by fitting to the results of the simulations for the corresponding quantity and are summarized in Table 5.2, along with those of the isolated droplet (section 4.2.2.3).

Table 5.2: Summary of proposed correlations.

	Isolated droplet	Representative chain droplet	Correction factor
We_{cr}	[150]	$We_{cr,RCD} = We_{cr,is} \cdot CF_{We_{cr}}$	$CF_{We_{cr}} = 1 + 5.5 \cdot \left(\frac{L}{D_0}\right)^{-2.2}$
$\frac{S_{max}}{S_0}$	[119]	$\frac{S_{max,RCD}}{S_0} = \frac{S_{max,is}}{S_0} \cdot CF_{S_{max}}$	$CF_{S_{max}} = 1 - e^{-0.21 \cdot We^{0.35} \cdot \left(\frac{L}{D_0} - 1\right)^{0.79}}$
t_{br}	[13, 38, 117, 150]	$t_{br,RCD} = t_{br,is} \cdot CF_{t_{br}}$	$CF_{t_{br}} = 1 + e^{-0.1 \cdot We^{0.64} \cdot \left(\frac{L}{D_0} - 1\right)^{0.71}}$

C_d	$\overline{C_{d,ts}} = 4 \cdot We^{-0.41}$	$\overline{C_{d,RCD}} = \overline{C_{d,ts}} \cdot CF_{C_d}$	CF_{C_d} $= 1 - e^{-0.038 \cdot We^{1.1} \cdot (\frac{L}{D_0} - 1)^{0.53}}$
B	B_{is} $= 1 + 0.016 \cdot We^{1.5}$	$B_{RCD} = B_{is} \cdot CF_B$	CF_B $= 1 - e^{-1.2 \cdot We^{-0.21} \cdot (\frac{L}{D_0} - 1)^{0.88}}$

The equation for the prediction of the S_{max}/S_0 of the RCD shows a mean absolute error equal to 6.6% compared to the CFD simulations, that of the t_{br} equal to 3.7%, while that of the C_d equal to 6.8%. Sensitivity analysis regarding the proposed coefficients showed that when the coefficient c_1 is increased by 10% the mean absolute error compared to the results of the simulations becomes equal to 7.3% for the S_{max} , equal to 3.5% for the t_{br} and equal to 6.9% for the C_d . For a 10% increase in the coefficient c_2 the errors are calculated as 7.6% (S_{max}), 3.8% (t_{br}) and 8.1% (C_d), while for the c_3 they are equal to 6.4% (S_{max}), 3.5% (t_{br}) and 7% (C_d).

5.2.2.3 Parametric study

5.2.2.3.1 Breakup map

Figure 5-6 presents the simulated cases of tandem droplet breakup in the L/D_0 - We map: the blue circles correspond to the cases that the representative chain droplet deforms without breaking up (Figure 5-5a), the red triangles to the cases that the droplets are clearly breaking up (Figure 5-5b), and finally the yellow diamonds correspond to the cases that the droplets become very thin without breaking (Figure 5-2 for $t/t_{sh}=2.1$). For the latter case it is quite likely that a 3-D simulation would predict breakup and therefore in the current work they are considered as transition points between breakup and no-breakup. It is apparent from Figure 5-6 that as the droplet distance L/D_0 decreases, the minimum We number required for the breakup to occur (critical We) is increasing rapidly as the representative chain droplet is greatly influenced by the upstream one. On the other hand, at large L/D_0 the value of the critical We number approaches the value of the isolated droplet, which is found equal to 14 from the simulation of an isolated droplet at the same conditions (Oh , Re , ε). Finally, Figure 5-6 presents the regions of the different breakup regimes encountered in the simulations (bag, shuttlecock and multi-bag). The bag breakup regime is encountered at We numbers in the range of 15 to 25 and droplet distances L/D_0 higher than 4, the multi-bag regime from $We=26$ up to 64 and for L/D_0 higher than 1.5, and the shuttlecock regime from $We=16$ up to 64 and L/D_0 less than 5.

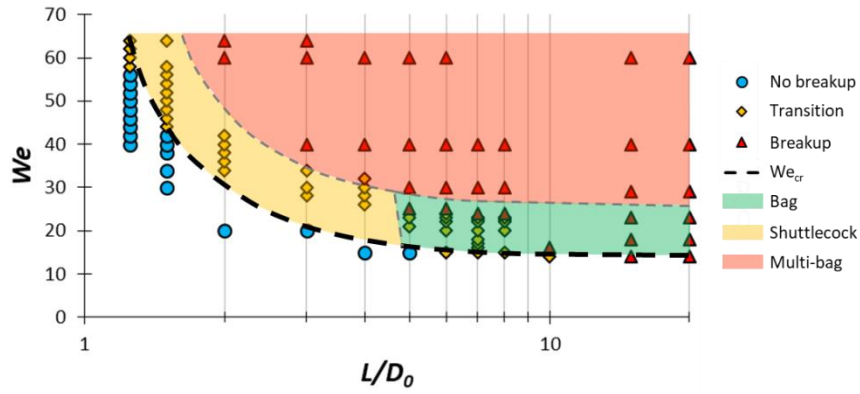


Figure 5-6: L/D_0 - We map with the simulated cases of tandem droplet breakup, along with the regions of the various breakup regimes ($Oh=0.05$, $\varepsilon=51$ and $N=37$).

5.2.2.3.2 Droplet surface area

The ratio of the maximum surface area of the representative chain to the isolated droplet $S_{max,RCD}/S_{max,is}$ is presented in Figure 5-7 as a function of We and L/D_0 . The colored dots correspond to the results of the CFD simulations, while the iso-lines (0.3, 0.6, 0.9 and 0.99) to the predictions of the proposed correlation of Table 5.2. For instance, the iso-line 0.6 corresponds to a 40% reduction in maximum surface area, relative to the one of an isolated droplet. It is observed that as the L/D_0 decreases the ratio $S_{max,RCD}/S_{max,is}$ also decreases, since the representative chain droplet is affected by the wake of its upstream droplet, reaching values as low as 0.21, indicating a strong influence of the maximum surface area on the droplet distance. Conversely, as the L/D_0 increases, the ratio $S_{max,RCD}/S_{max,is}$ approaches unity and the maximum liquid surface area of the representative chain droplet approaches the corresponding value of the isolated one. Finally, the dependence of the ratio on the We number is weak, as indicated by the almost vertical iso-lines.

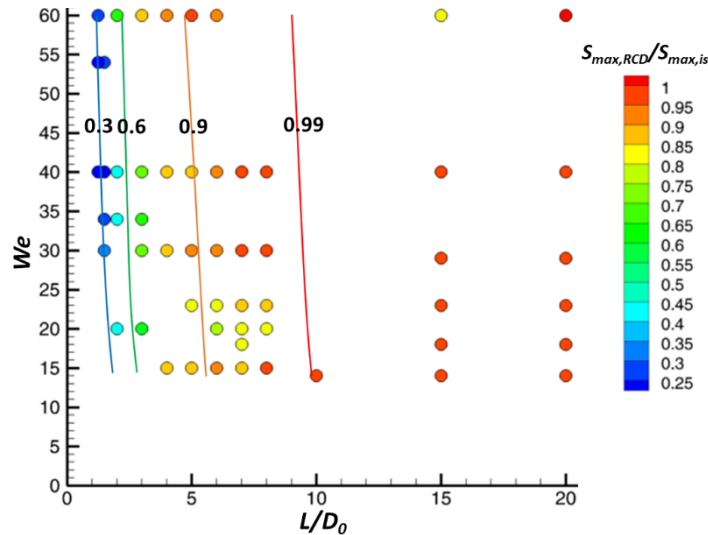


Figure 5-7: Ratio $S_{max,RCD}/S_{max,is}$ as function of We and L/D_0 (scatter: CFD, lines: correlation of Table 5.2).

5.2.2.3.3 Breakup initiation time

Similar to the droplet surface area, the breakup initiation time of the representative chain droplet is also different from that of the isolated one for the same conditions. By looking back at Figure 5-2 for $t/t_{sh}=2.1$ we observe that the trailing droplets break up later than the isolated one. Figure 5-8 presents the ratio $t_{br,RCD}/t_{br,is}$ as a function of We and L/D_0 , as predicted by the CFD simulations (colored dots) and the proposed correlation of Table 5.2 (iso-lines); only the cases that actually break up are taken into account, i.e. the red triangles of Figure 5-6. We notice that for large L/D_0 the ratio $t_{br,RCD}/t_{br,is}$ approaches unity (similar to $S_{max,RCD}/S_{max,is}$), while as the L/D_0 decreases the breakup time of the representative droplet increases. The effect of L/D_0 on this ratio is larger at lower We numbers, while for the examined cases the breakup time is not increasing more than 23% compared to that of an isolated droplet.

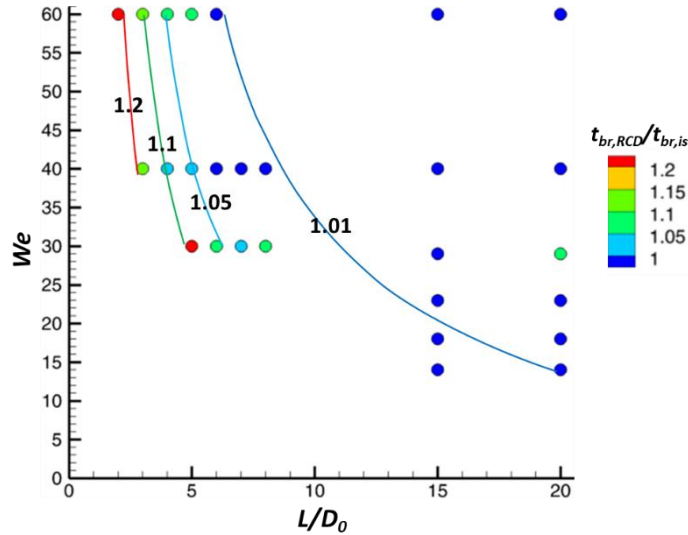


Figure 5-8: Ratio $t_{br,RCD}/t_{br,is}$ as function of We and L/D_0 (scatter: CFD, lines: correlation of Table 5.2).

5.2.2.3.4 Drag coefficient

The drag coefficient can be found from the droplet force balance in the streamwise direction [153], similar to section 4.2.2.1.2, which is given for a decelerating droplet in equation (5-3) (particle motion equation).

$$\frac{dU_d(t)}{dt} = -C_d(t) \cdot \frac{A_f(t)}{A_{f,0}} \cdot \frac{3}{4D_0\varepsilon} \cdot U_d^2 \quad (5-3)$$

As seen from equation (5-3), an estimation of the droplet frontal area variation ($A_f(t)/A_{f,0}$) is needed in order to calculate the drag coefficient of a deforming droplet. Pilch and Erdman [38] excluded the frontal area term from equation (5-3) and its effect was incorporated into the drag coefficient. This method was later utilized by [114] and [33] for the calculation of the average drag coefficient of a deforming droplet as function of the Re number. Another method, proposed initially by [90, 154] and utilized later by [72, 92], assumes that the drag coefficient of a deforming droplet can be estimated as a linear interpolation between the drag coefficient of a spherical object (initial droplet shape) and that of disk (deformed droplet shape) for the same Re number, depending on the droplet deformation. This geometrical estimation of the drag coefficient requires the solution of an additional equation for the prediction of droplet deformation as a function of time, which might be computationally costly when applied to spray models for a very large number of droplets. In this section a method is proposed in which the droplet frontal area

is assumed to vary linearly with time (equation (5-4), where $t^*=t/t_{sh}$), in an attempt to simplify as much as possible the calculations. This is a first step towards the estimation of the temporal variation of droplet frontal area, whereas more accurate and complex models can be later utilized such as those presented in section 1.2.3. The linear approach followed in the current study applies only to droplets experiencing breakup and therefore is utilized only for the cases corresponding to the breakup and transition points of Figure 5-6.

$$\frac{A_f(t^*)}{A_{f,0}} = 1 + B \cdot t^* \quad (5-4)$$

The factor B represents the average dimensionless deformation rate given by equation (5-5), where t_{max}^* is the time instance corresponding to $S=S_{max}$ up to which the drag coefficient is calculated. This time instance is chosen instead of the actual breakup time because in some cases droplets do not clearly break (transition points in Figure 5-6).

$$B = \frac{\frac{A_f(t_{max}^*)}{A_{f,0}} - 1}{t_{max}^*} \quad (5-5)$$

By substituting equations (5-4) and (5-5) into equation (5-3) and integrating for t^* we get equation (5-6), which gives the temporal evolution of droplet velocity; note that an average drag coefficient $\overline{C_d}$ is used instead of $C_d(t)$. By fitting equation (5-6) to the results of the simulations ($U_d - t^*$) the average drag coefficient of each case is calculated.

$$U_d(t^*) = \frac{U_{d,0}}{\overline{C_d} \cdot \frac{3}{4\sqrt{\varepsilon}} \cdot (t^* + \frac{B \cdot (t^*)^2}{2}) + 1} \quad (5-6)$$

The results of the ratio $\overline{C_{d,RCD}}/\overline{C_{d,IS}}$ are shown in Figure 5-9 as a function of We and L/D_0 as calculated by the CFD simulations (colored circles) along with the predictions of the correlation from Table 5.2. The ratio $\overline{C_{d,RCD}}/\overline{C_{d,IS}}$ decreases when the ratio L/D_0 is decreasing, in agreement with previous studies [56, 66-70], reaching values down to 0.75. A strong dependence of the ratio on the We number is observed as depicted by the iso-

lines, something that is attributed to the dependence of the frontal area on the We number as well.

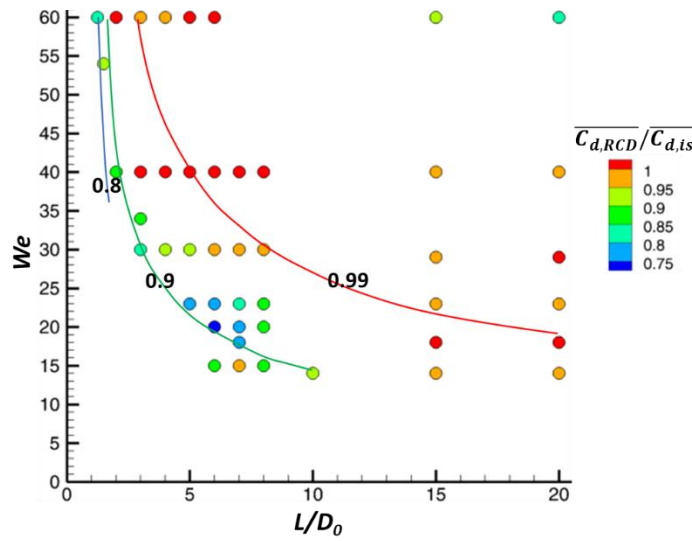


Figure 5-9: Ratio $\overline{C_{d,RCD}}/\overline{C_{d,IS}}$ as function of We and L/D_0 (scatter: CFD, lines: correlation of Table 5.2).

Finally, equation (5-6) predicts the temporal evolution of droplet velocity, using C_d and B from Table 5.2. Figure 5-10 presents the temporal evolution of droplet velocity of a representative chain droplet for two We numbers (40 and 60) and $L/D_0=2$ as predicted by the equation and the CFD simulations, up to the point of breakup initiation. As it is observed from the figure there is a good agreement between the simulations and the predictions from the equation for both We numbers up to approximately $t/t_{sh}=1.6$, while after that point a deviation is observed. The velocity as predicted by the CFD simulations seems to approach a constant value, while that of the equation continues to decrease. This observed trend in the simulations is due to the low air velocity (in terms of the relative one) appearing in the upstream of the representative chain droplet, which is attributed to the wake induced by the upstream droplet (see Figure 5-2 for $t/t_{sh}=2.1$). For the cases characterized by larger L/D_0 , the results resemble those of an isolated droplet at the same conditions.

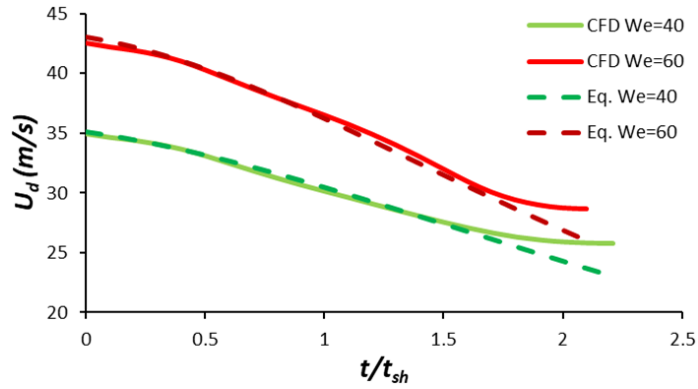


Figure 5-10: Temporal evolution of droplet velocity for two We numbers (40 and 60) and $L/D_0=2$ as predicted by the CFD simulations and the correlation (5-6).

5.2.2.4 Overall assessment of the effect of streamwise distance between the droplets

In order to summarize the effect of the droplet distance L/D_0 on the deformation of a representative chain droplet, a marked area is identified in the map L/D_0-We , where the effect of L/D_0 can be considered significant, as shown in Figure 5-11. In this marked area either the maximum surface area, the breakup initiation time or the drag coefficient of the representative chain droplet differs more than 5% from those of an isolated droplet at the same conditions. As it is observed from the figure, the distance between the droplets is important when L/D_0 is less than 9 (or higher for low We). This indicates that most of the analytical models used for isolated droplets, when applied to droplet chains, are valid for L/D_0 and We numbers higher than 9 and 20, correspondingly.

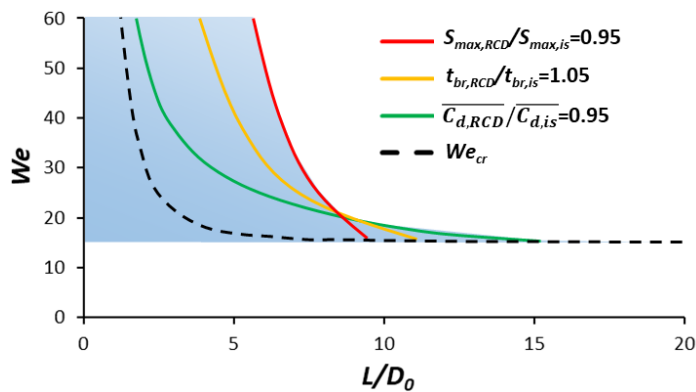


Figure 5-11: Area of influence of the distance between the droplets depicted in the L/D_0-We map along with the iso-lines of $S_{max,RCD}/S_{max,is}$, $t_{br,RCD}/t_{br,is}$, $\overline{C_{d,RCD}}/\overline{C_{d,is}}$ and the critical We .

5.3 Single-sheet clusters

5.3.1 Computational setup and examined conditions

Figure 5-12 presents an infinite cluster of droplets arranged in parallel to the air flow along with the computational domains utilized for its simulation: i) a 3-D domain with four droplet quarters (abbreviated as 3-D-4), ii) a 3-D domain of a single droplet quarter (abbreviated as 3-D-1), and iii) a 2-D axisymmetric domain. In all cases symmetry boundary conditions are utilized to reflect the presence of surrounding droplets. In the following section (5.3.1.1) it is shown that the two examined 3-D configurations are equivalent, since they give similar results for a simulation at the same conditions. On the other hand, for the case of the 2-D axisymmetric simulations, the adoption of a symmetry boundary condition does not strictly reflect the effect of the neighbor droplets at a 45° direction (diagonal). However, the results using the 2-D domain are close to those of the 3-D simulations, even for very low values of $H/D_0 (=2)$ (see section 5.3.1.1). For this reason, the 2-D approach is utilized in the parametric study since it is much more computationally efficient, therefore making it possible to simulate the 67 examined cases within a reasonable time.

The droplet is initially stagnant, while air flows from the right boundary forcing it to move and deform. In Figure 5-12c and d, the distance measured from the center of the droplet to the symmetry boundary conditions is equal to half the distance between the droplets ($H/2D_0$). In the depicted cases of Figure 5-12 this is equal to 1, and therefore $H/D_0=2$, while for a different H/D_0 the height of the domain should be adjusted accordingly, resulting in a new computational domain.

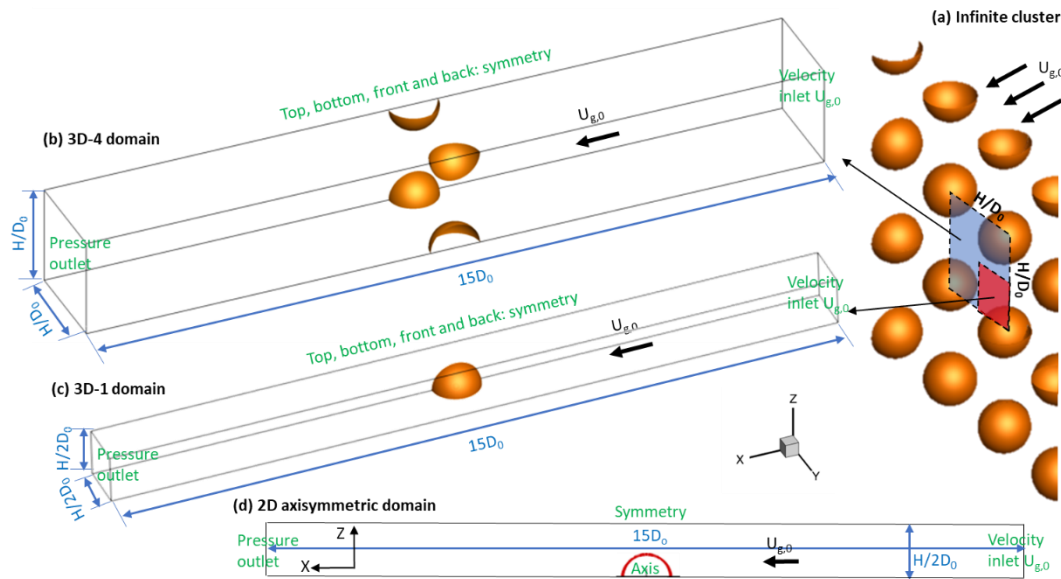


Figure 5-12: a) Actual configuration with an infinite cluster of droplets along with the computational domains and boundary conditions used in the simulations: b) 3-D-4 domain, c) 3-D-1 domain, and d) 2-D axisymmetric domain.

The air and liquid properties are those of Table 5.1, while by changing the air velocity the obtained We numbers range from 5 up to 60; the Re number lies in the range of 240 to 832. The examined non-dimensional distances measured from the droplet centers (H/D_0) range from 1.25 up to 20, resulting in 69 examined cases in total (two of which are in 3 dimensions with $We=40$ and $H/D_0=2$) (see Figure 1-7). Finally, ten 2-D axisymmetric simulations of isolated droplets are utilized for comparison, the same as in the previous section (5.2) ($We=15-60$). These simulations are utilized in section 5.3.2.2 to calculate the quantities of the isolated droplet, which are compared with those of the droplet in a cluster.

5.3.1.1 Comparison between the computational domains

Before proceeding to the discussion of the results, a comparison is made between the computational domains of Figure 5-12 in order to justify their selection for the corresponding simulations. Figure 5-13 presents the temporal evolution of droplets' shape as predicted by the simulation of a case with $We=40$ and $H/D_0=2$ using the 3-D-4 and 3-D-1 computational domains. As it is observed, the droplet shapes of the four droplets are identical between them as also with that of the single droplet (3-D-1 domain). This is further justified by looking at Figure 5-14, which presents the temporal evolution of droplet deformation in both axes (cross-stream and streamwise) as well as the droplet velocity. The results of the 3-D-4 and 3-D-1 domains are identical for the droplet velocity,

while a small deviation is observed for the droplet deformation after $t/t_{sh}=1.1$, which is attributed to the micro-droplets that are detached from the parent droplet. In the following sections, only the results of the 3-D-1 configuration are presented for simplicity. Moreover, the same configuration is used in the next section (5.4). It should be noted that the cross-stream deformation in the 3-D simulations varies in the Y-Z plane (see Figure 5-13). For reasons of simplicity, it is assumed that $D_{cr}=0.5*(D_y+D_z)$, without accounting for any disturbances in the diagonal direction of the Y-Z plane.

Turning now to the results of the 2-D-axisymmetric simulation, these are presented in Figure 5-14 as well. As it can be seen, they are close to those of the 3-D simulations for the droplet deformation, while for the droplet velocity a small deviation is observed, up to approximately $t/t_{sh}=1$. Nevertheless, these differences are expected to decrease at higher droplet distances H/D_0 , as the droplets in cluster formation tend to approach the behavior of an isolated droplet. The results of the 2-D axisymmetric simulations are utilized mainly for the parametric study of this work, since they require approximately 160 times less computational resources than the 3-D-1 domain, in terms of CPU-hours.

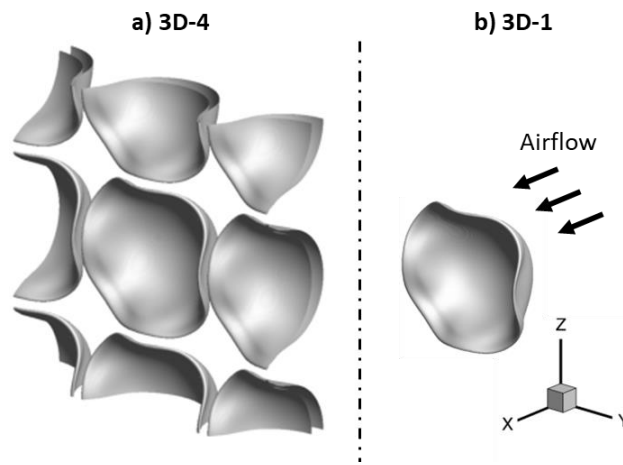


Figure 5-13: Droplet shape at the time instance of $t/t_{sh}=1$ as predicted by the simulation of a case with $We=40$ and $H/D_0=2$ using a) the 3-D-4 and b) the 3-D-1 computational domains.

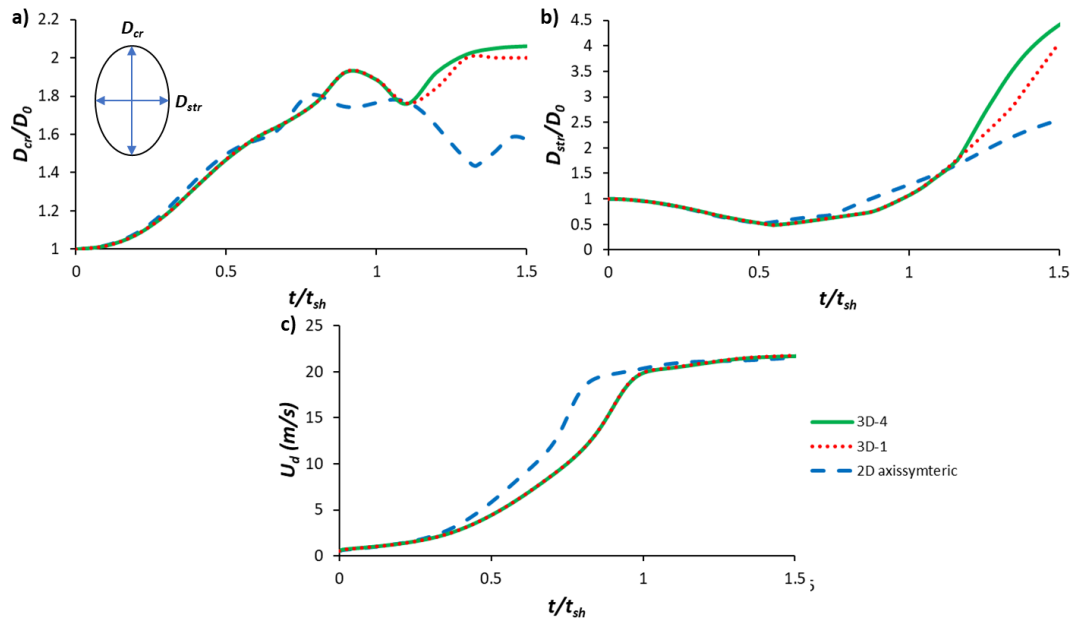


Figure 5-14: Temporal evolution of a) cross-stream droplet deformation, b) streamwise droplet deformation, and c) droplet velocity, as calculated by a simulation with $We=40$ and $H/D_0=2$ using the three computational domains: i) 3-D-4, ii) 3-D-1 and iii) the 2-D axisymmetric.

5.3.2 CFD Results

5.3.2.1 Droplet shapes

Figure 5-15 illustrates the temporal evolution of droplet shape as predicted both by the 3-D and the 2-D axisymmetric simulations (shape drawn with 3-D rotation around the x-axis) of a case with $We=40$ and $H/D_0=2$, as well as from the simulation of an isolated droplet at the same We number (2-D axisymmetric with 3-D rotation). As it is observed, the droplet in the cluster formation initially deforms into a disk-like shape ($t/t_{sh}=0.4$), followed by a semi-spherical shape ($t/t_{sh}=0.8$); breakup occurs with stripping of liquid from its periphery ($t/t_{sh}=1.5$). This breakup mode is the same as the one experienced in tandem droplet breakup (section 5.2.2.1), called shuttlecock. Turning now to the isolated droplet, it experiences the well-known multi-bag breakup regime, in which the droplet gradually deforms into a disk-like shape followed by the creation of a bag at its periphery (not shown here). In addition, its breakup occurs much slower compared to the cluster arrangement, at approximately $t/t_{sh}=2.3$ compared to $t/t_{sh}=1.4$ (and 1.2 in the 3-D simulation); this observation was also reported in the work of [57].

Regarding the comparison between the 2-D and 3-D simulations, they both predict similar droplet shapes up to $t/t_{sh}=0.8$, while after $t/t_{sh}=1$ a deviation is observed. At that time instance, the 3-D simulation predicts a wavy shape for the ring formed around the

droplet, as shown in Figure 5-15 ($t/t_{sh}=1$). This is attributed, on the one hand, to the Kelvin-Helmholtz instabilities [9, 19], and on the other, to the bigger gap between the droplets in the diagonal direction compared to the vertical one. This causes non-uniform pressure and velocity distributions along the periphery of the droplet, as shown in Figure 5-16, where the Y-Z slices are presented for the dimensionless pressure $((P - P_\infty)/\frac{1}{2}\rho_g U_{g,0}^2)$ and relative velocity ($t/t_{sh}=0.9$). Eventually, at $t/t_{sh}=1.5$ the waves turn into ligaments, since most of the liquid is concentrated at the corners of the droplet rather than its center.

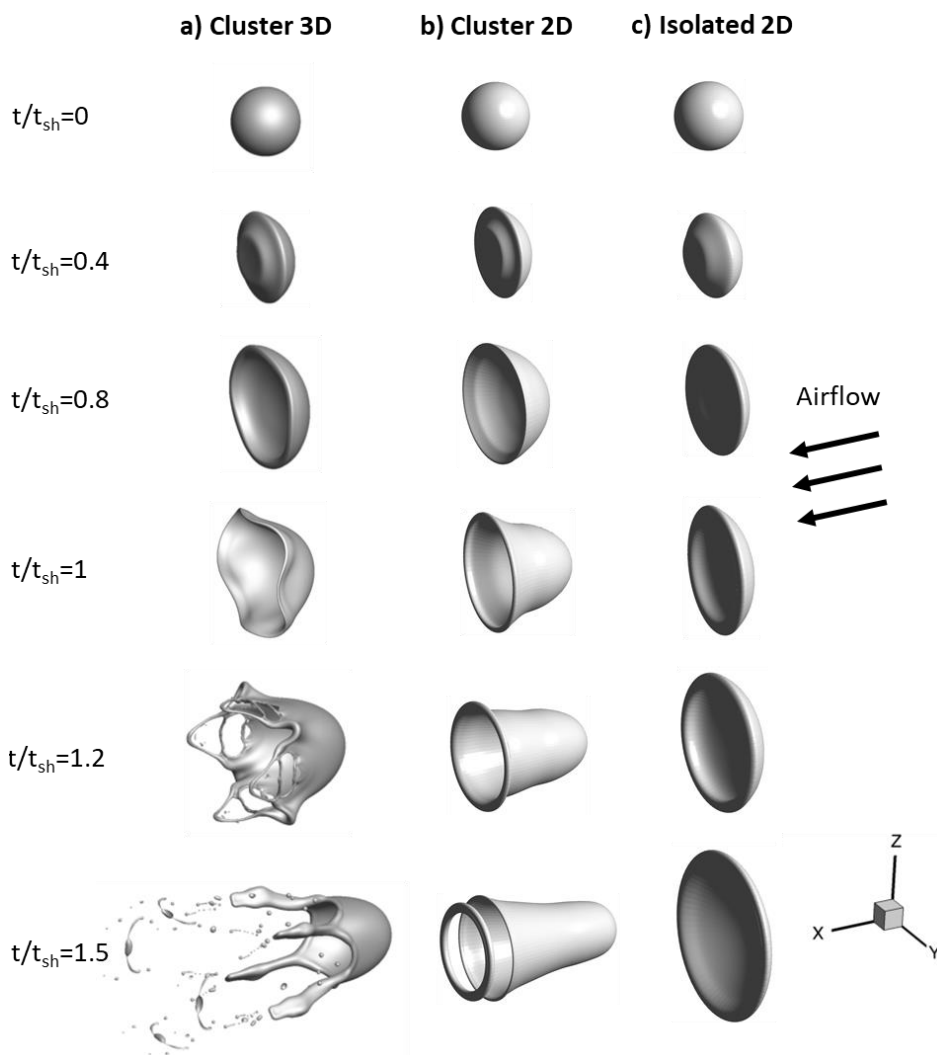


Figure 5-15: Temporal evolution of droplet shape as predicted by a) the 3-D simulation and b) the 2-D axisymmetric (3-D rotation) of a droplet in a single-sheet cluster with $H/D_0=2$ and $We=40$, as well as an isolated droplet at the same We number (2-D axisymmetric).

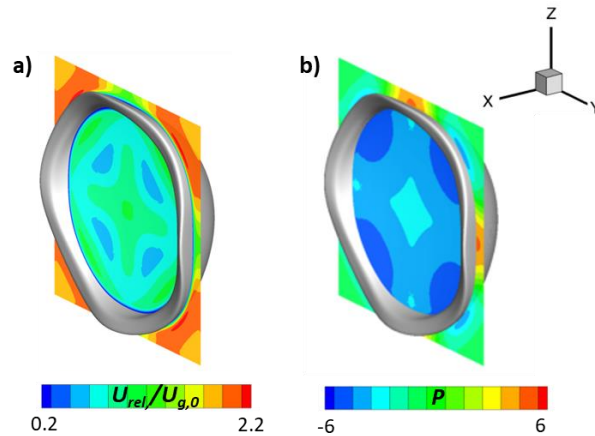


Figure 5-16: Y-Z slices of the dimensionless a) velocity and b) pressure as predicted by the 3-D simulation of a case with $H/D_0=2$ and $We=40$ ($t/t_{sh}=0.9$).

The differences in the shape and breakup modes of the isolated and cluster droplet arrangements are better explained by looking at Figure 5-17, which presents the contour of non-dimensional relative velocity for the same cases as those of Figure 5-15. In the cluster formation, the air accelerates in the narrow gap between the droplets (red color in the contour), causing the droplet to deform more at its periphery rather than its core. This results in the shifting of the breakup mode from multi-bag in the isolated droplet to shuttlecock in the case of cluster arrangement.

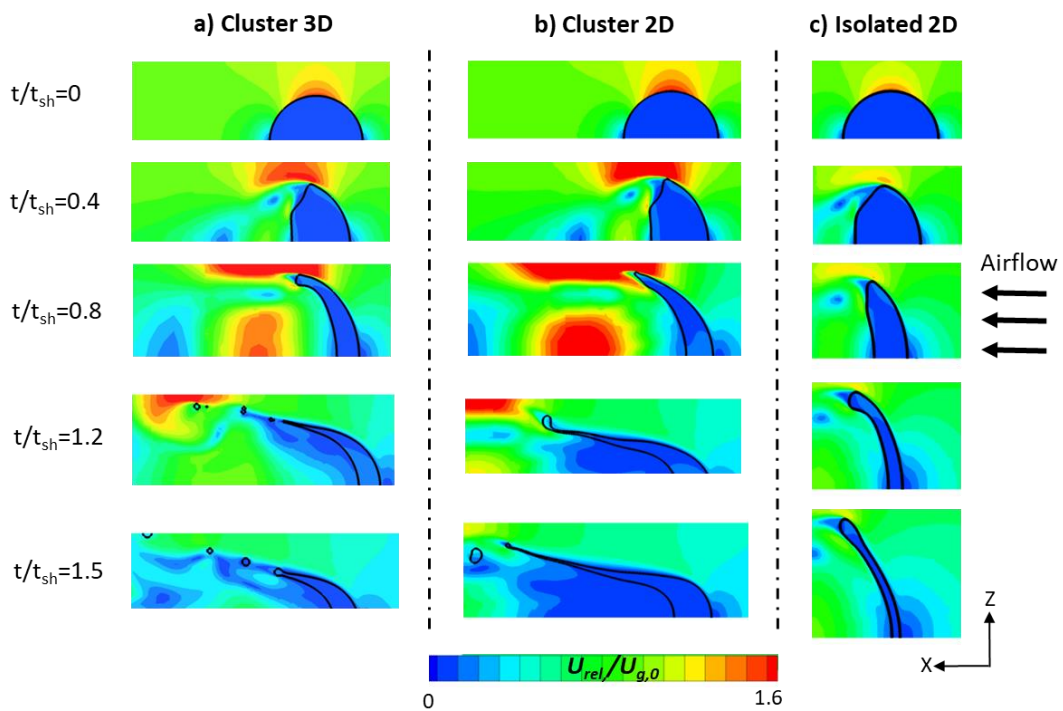


Figure 5-17: Non-dimensional relative velocity contour (X-Z plane) for a case of a droplet in a cluster (3-D and 2-D axisymmetric) with $We=40$ and $H/D_0=2$, as well as an isolated droplet at the same We number.

In order to investigate the effect of distance between the droplets on the breakup mode, Figure 5-18 shows the temporal evolution of droplet shape for three cases corresponding to $H/D_0=4$, $H/D_0=2$ and $H/D_0=1.25$ (2-D axisymmetric domain). For large droplet distances and depending on the We number, the effect of the surrounding droplets is weak and the breakup mode becomes identical to that of the isolated droplet (bag breakup mode of Figure 5-18a). When the distance decreases, the breakup mode shifts from bag to deformation without breakup (Figure 5-18b), since the air flow is directed towards the periphery of the droplet, but without being intense enough to cause liquid stripping from its periphery. However, when the distance is further decreased, the air velocity becomes high enough to cause the breakup of the droplet, and the breakup mode shifts to shuttlecock (Figure 5-18c). This non-monotonic behavior is better understood by looking at Figure 5-19, which presents a highlight of the dimensionless pressure contour $((P - P_\infty)/(\frac{1}{2}\rho_g U_{g,0}^2))$ for the three cases. For the larger droplet distances ($H/D_0=4$ in the figure), the pressure is higher at the core of droplet and lower at its periphery, causing the formation of the bag. At smaller distances ($H/D_0=2$), the peripheral pressure increases and becomes equal to the central, therefore preventing the creation of the bag. Finally, at even smaller distances ($H/D_0=1.25$), the peripheral pressure increases further causing the shuttlecock breakup mode.

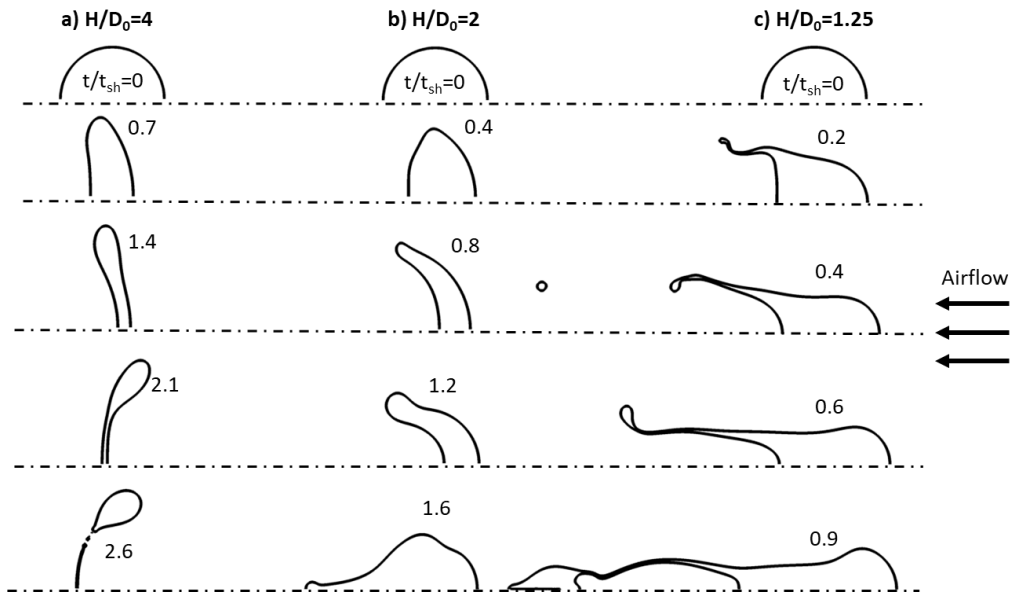


Figure 5-18: Temporal evolution of droplet shape for three cases with $We=15$ and: a) $H/D_0=4$, b) $H/D_0=2$ and c) $H/D_0=1.25$.

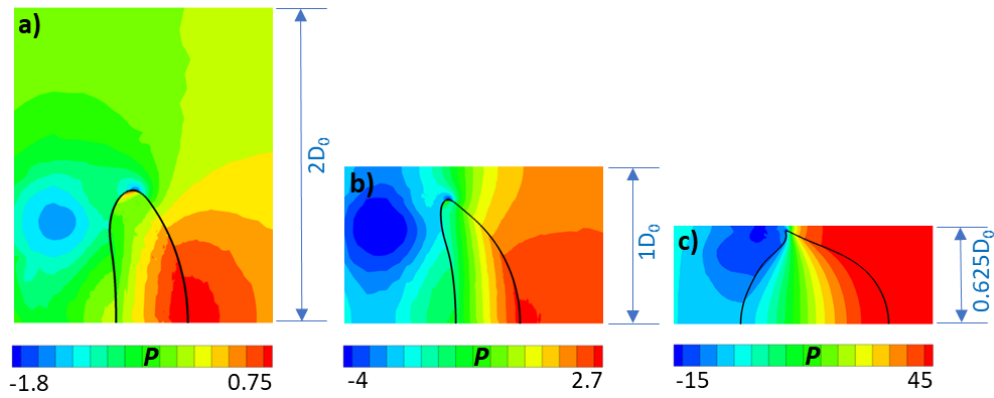


Figure 5-19: Dimensionless pressure contour for three cases with $We=15$ and: a) $H/D_0=4$ ($t/t_{sh}=0.7$), b) $H/D_0=2$ ($t/t_{sh}=0.6$) and c) $H/D_0=1.25$ ($t/t_{sh}=0.1$).

5.3.2.2 Parametric study

5.3.2.2.1 Breakup map

Figure 5-20 presents in the H/D_0 - We map the simulated cases of single-sheet droplet clusters along with the encountered breakup regimes. For $H/D_0 \geq 4$ the droplets behave as being isolated, i.e. the bag breakup regime is encountered for $We \leq 20$, while for $We > 20$ they experience the multi-bag mode. For lower values of H/D_0 (< 4) and low We numbers (≤ 30), the breakup mode shifts to deformation without breakup (Figure 5-18b). Finally, when the distance becomes even smaller ($H/D_0 \leq 2.5$), the shuttlecock breakup regime is encountered, even for values of We number as low as 9, which is smaller than the value of the critical We number of an isolated droplet at the same conditions ($We_{cr, is} = 14$).

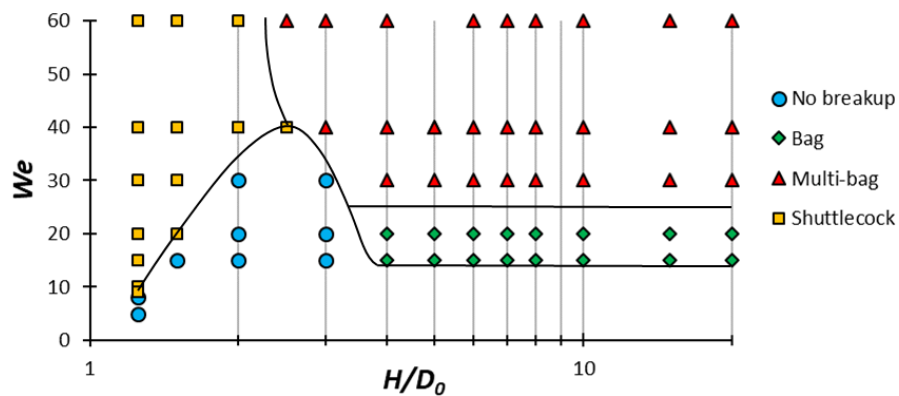


Figure 5-20: H/D_0 - We map with the simulated cases of single-sheet clusters, along with the encountered breakup regimes ($Oh=0.05$, $\epsilon=51$ and $N=37$); the lines that separate the various breakup regimes are also presented.

5.3.2.2.2 Droplet surface area

The ratio of the maximum surface area of a droplet in a single-sheet cluster to the maximum surface area of an isolated droplet ($S_{max,cl}/S_{max,is}$) is presented in Figure 5-21, as function of the We number and the H/D_0 . The ratio $S_{max,cl}/S_{max,is}$ takes very low values at high We and low H/D_0 , reaching values as low as 0.22, which corresponds to a 78% reduction in the maximum surface area of a droplet in cluster formation, relative to the one of an isolated droplet at the same We . This is attributed to the very fast breakup occurring at these conditions with liquid stripped from its periphery, while its core remains relatively non-deformed. On the other hand, at low We and H/D_0 the ratio $S_{max,cl}/S_{max,is}$ is greater than 1, reaching values as high as 1.29, owing to the very large streamwise droplet deformation (Figure 5-18c). Finally, the solid line of Figure 5-21 defines the region of influence of the maximum surface area of a droplet in cluster formation; this occurs for droplet distances of approximately $H/D_0 \leq 5$.

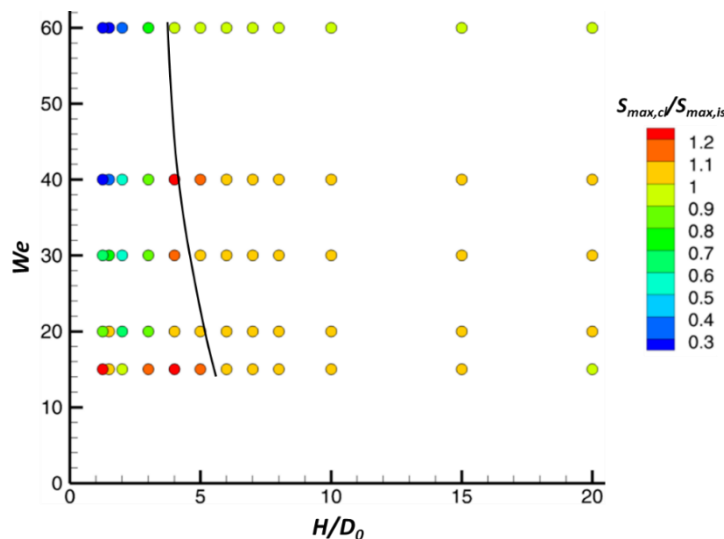


Figure 5-21: Ratio $S_{max,cl}/S_{max,is}$ as function of We and H/D_0 . The black line defines the region of influence of the maximum surface area of a droplet in a single-sheet cluster.

5.3.2.2.3 Breakup initiation time

As already mentioned in section 5.3.2.1, a droplet inside a cluster breaks up faster than an isolated droplet. The ratio $t_{br,cl}/t_{br,is}$ is presented in Figure 5-22 as function of the We number and the H/D_0 . The ratio $t_{br,cl}/t_{br,is}$ decreases with decreasing H/D_0 , reaching values as low as 0.1. As can be seen from the figure, the breakup time of the cluster formation differs from that of the isolated at distances $H/D_0 \leq 3$.

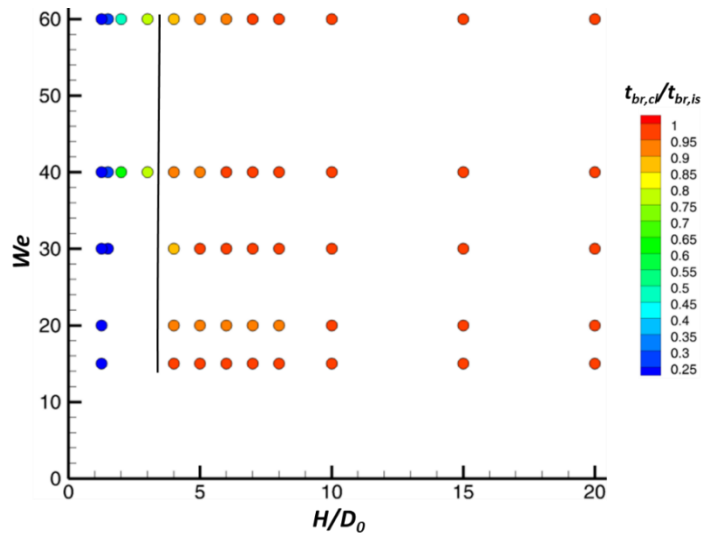


Figure 5-22: Ratio $t_{br,cl}/t_{br,is}$ as function of We and H/D_0 . The black line defines the region of influence of the breakup time of a droplet a single-sheet cluster.

5.3.2.2.4 Drag coefficient

The average drag coefficient is found for each simulated case using the same procedure as the one described in section 5.2.2.3.4, and the ratio $C_{d,cl}/C_{d,is}$ is presented in Figure 5-23, as function of the We number and the H/D_0 . The ratio $C_{d,cl}/C_{d,is}$ increases with decreasing H/D_0 , reaching values as high as 29; this trend is in agreement with the works of [6, 56, 63, 66, 67]. Overall, the drag coefficient of droplets in cluster formations differs from that of the isolated droplet for distances $H/D_0 \leq 2$.

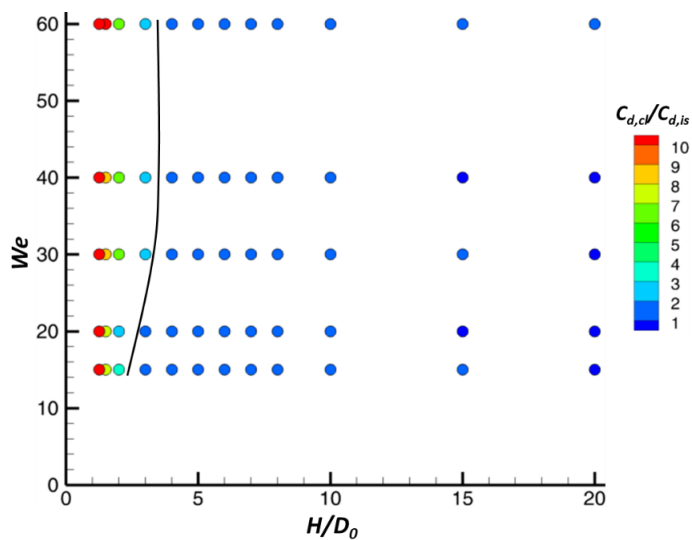


Figure 5-23: Ratio $C_{d,cl}/C_{d,is}$ as function of We and H/D_0 . The black line defines the region of influence of the drag coefficient of a droplet a single-sheet cluster.

5.4 Multi-sheet clusters

5.4.1 Computational setup and examined conditions

Similar to section 5.3, Figure 5-24 presents an infinite cluster of droplets arranged parallel to the air flow, along with the 2-D axisymmetric and 3-D domains utilized for its simulation. Four droplets are simulated instead of one, in accordance with section 5.2, while the third droplet of the row is called representative cluster droplet (RCLD), similar to the RCD (section 5.2). The comparison of the 2-D axisymmetric and 3-D domains has been presented in section 5.3.1.1 for a single droplet, while a similar accuracy has been observed for the RCLD. In Figure 5-24 the non-dimensional streamwise (L/D_0) and cross-stream (H/D_0) distances between the droplets are equal to 2. The examined L/D_0 numbers range from 1.25 up to 9, while the H/D_0 from 1.25 up to 5; these numbers are selected based on the results of tandem breakup (section 5.2.2) and those of single-sheet clusters (section 5.3.2). The liquid and air properties are those of Table 5.1, while the We number ranges from 10 up to 60, for a total of 56 examined cases; the resulting Re numbers range from 340 up to 832.

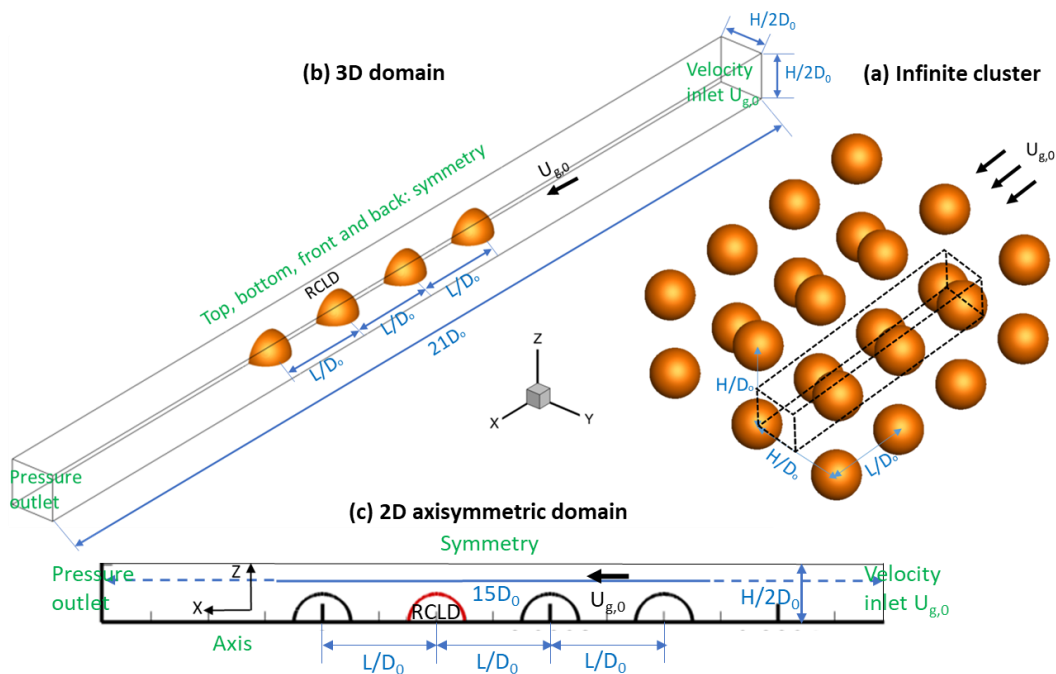


Figure 5-24: a) Actual configuration with an infinite cluster of droplets along with the computational domains and boundary conditions used in the simulations: b) 3-D-domain and c) 2-D axisymmetric domain.

5.4.2 CFD Results

5.4.2.1 Droplet shapes

Figure 5-25 presents the temporal evolution of droplet shape of the RCLD, as predicted by the 3-D simulation with $H/D_0=2$, $L/D_0=2$ and $We=40$. Similar to the droplet in a single-sheet cluster (Figure 5-15), the RCLD deforms into a disk-like shape ($t/t_{sh}=0.4$), followed by a semi-spherical shape ($t/t_{sh}=0.7$), then a wavy shape is formed in the ring around the droplet ($t/t_{sh}=1$), and eventually shuttlecock breakup occurs with liquid stripping from the periphery of the droplet (ligament formation at $t/t_{sh}=1.3$). The latter is attributed, on the one hand, to the Kelvin-Helmholtz instabilities [9, 19], and on the other to the bigger gap between the droplets in the diagonal direction compared to the vertical one. This causes non-uniform pressure and velocity distributions along the periphery of the droplet, as shown in Figure 5-26, where the Y-Z slices are presented for the dimensionless pressure $((P - P_\infty)/\frac{1}{2}\rho_g U_{g,0}^2)$ and relative velocity ($t/t_{sh}=1$). Regarding the differences in the shape between the single- and multi-sheet clusters, the RCLD shows a larger streamwise deformation compared to the droplet in a single-sheet cluster (Figure 5-15), due to the presence of the upstream droplets, as shown in Figure 5-27. These result in an even higher velocity at the droplet periphery compared to its core, as presented in Figure 5-28, where the temporal evolution of the non-dimensional velocity is presented for the same case ($t/t_{sh}=0.8$ and 1.2).

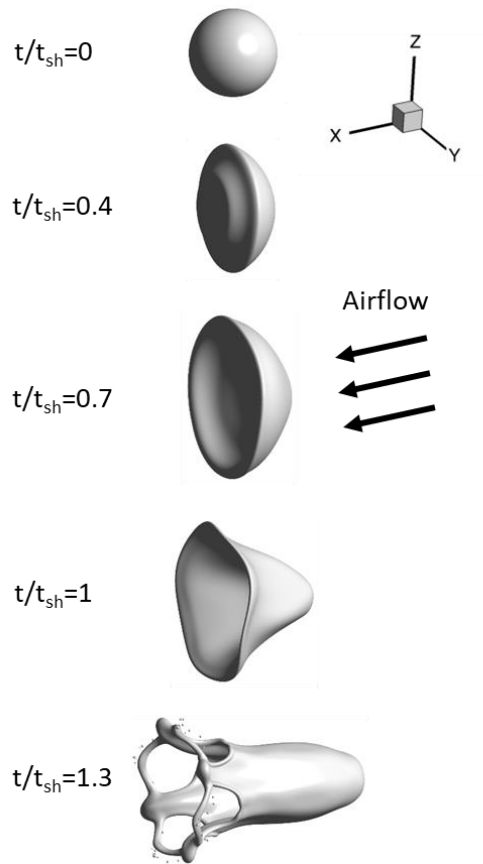


Figure 5-25: Temporal evolution of droplet shape of the RCLD, as predicted by the 3-D simulation with $H/D_0=2$, $L/D_0=2$ and $We=40$.

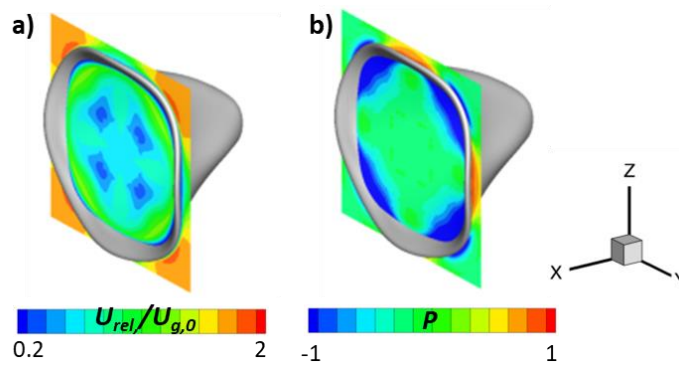


Figure 5-26: Y-Z slices of the dimensionless a) velocity and b) pressure as predicted by the 3-D simulation of a case with $H/D_0=2$, $L/D_0=2$ and $We=40$ ($t/t_{sh}=1$).

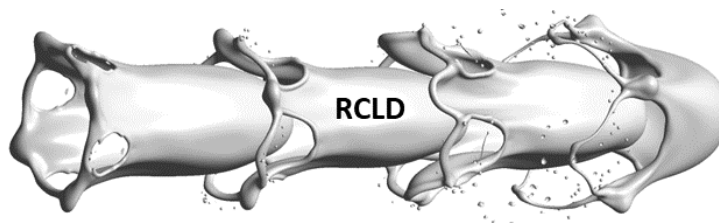


Figure 5-27: Droplet shapes at $t/t_{sh}=1.3$, as predicted the 3-D simulation of a multi-sheet cluster with $H/D_0=2$, $L/D_0=2$ and $We=40$.

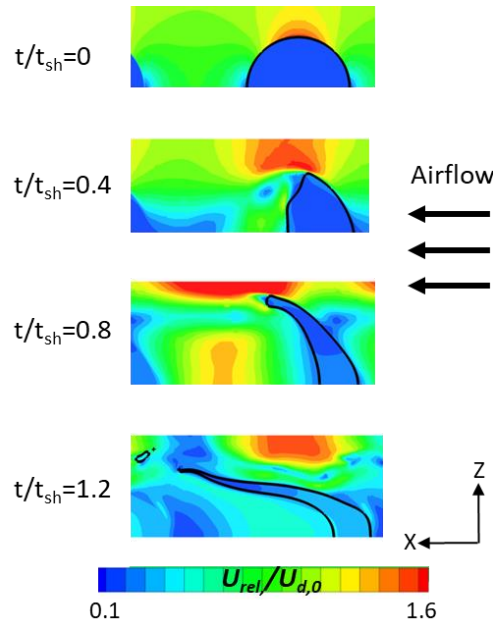


Figure 5-28: Non-dimensional relative velocity contour (X-Z plane) of the RCLD as predicted by the 3-D simulations ($H/D_0=2$, $L/D_0=2$ and $We=40$).

5.4.2.2 Parametric study

5.4.2.2.1 Breakup maps

Figure 5-29 presents in the H/D_0 - We map the simulated cases of multi-sheet clusters (RCLD) for two streamwise droplet distances: a) $L/D_0=9$ and b) $L/D_0=1.25$. For the large droplet distance ($L/D_0=9$), the droplets behave similar to the single-sheet clusters (Figure 5-20), since they are far enough in the streamwise direction. Breakup occurs at $We=10$, which is smaller than the value of the critical We number of an isolated droplet at the same conditions ($We_{cr, is}=14$). Moreover, the line of We_{cr} shows a non-monotonic behavior with the H/D_0 , for the same reason as in the single-sheet clusters (Figure 5-18 and Figure 5-19). Turning now to the small streamwise droplet distance ($L/D_0=1.25$), only the shuttlecock breakup regime is encountered, while the cases with $H/D_0=5$ and $We \leq 45$ do not experience breakup, in contrast with the cases with the larger distance ($L/D_0=9$). This is attributed to the presence of the upstream droplets, which hinder the incoming air flow, similar to the droplets in tandem formation (Figure 5-5 and Figure 5-6).

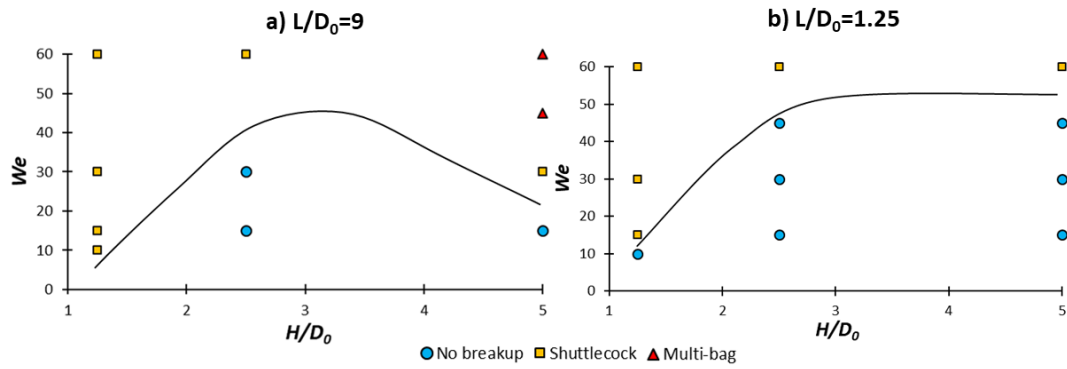


Figure 5-29: H/D_0 - We maps with the simulated cases of multi-sheet clusters (RCLD) for two streamwise droplet distances: a) $L/D_0=9$ and b) $L/D_0=1.25$ ($Oh=0.05$, $\varepsilon=51$ and $N=37$); the lines that separate the cases with breakup from those without breakup are also presented.

5.4.2.2.2 Droplet surface area

The ratio of the maximum surface area of the RCLD to the maximum surface area of an isolated droplet ($S_{max,RCLD}/S_{max,is}$) is presented in Figure 5-30, as function of the We number, the H/D_0 and the L/D_0 . Similar to the droplets in tandem formation (Figure 5-7), the ratio $S_{max,RCLD}/S_{max,is}$ increases with L/D_0 in most cases, while its dependence on H/D_0 depends on the We : for low We numbers the ratio decreases with the increase of H/D_0 , while it increases at high We numbers, similar to the single-sheet clusters (Figure 5-21). The maximum value of the ratio is equal to 1.35 and is encountered at $L/D_0=3$, $H/D_0=1.25$ and $We=15$, while the minimum is equal to 0.21 at $L/D_0=9$, $H/D_0=1.25$ and $We=60$.

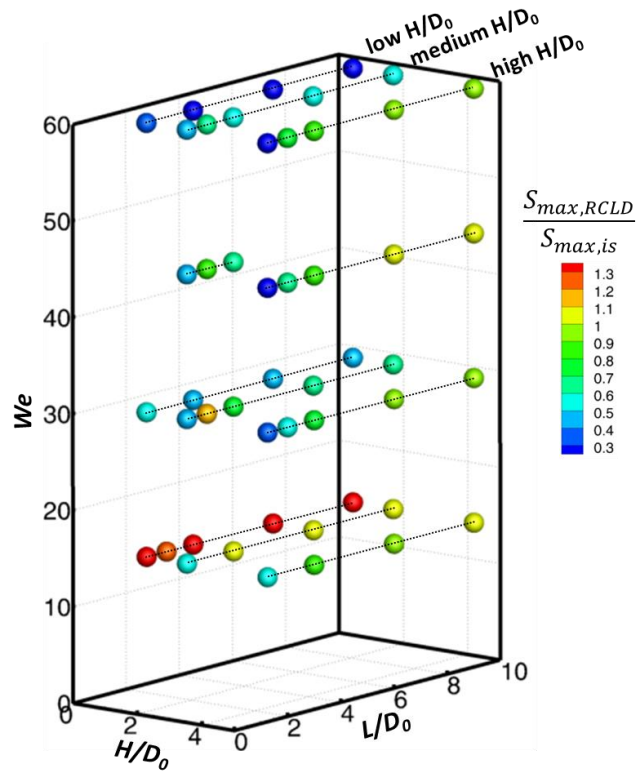


Figure 5-30: Ratio $S_{max,RCLD}/S_{max,is}$ as function of We , H/D_0 and L/D_0 .

5.4.2.2.3 Breakup initiation time

Figure 5-31 presents the ratio $t_{br,RCLD}/t_{br,is}$ as function of We , H/D_0 and L/D_0 (only the cases that actually breakup are presented). The ratio decreases with the decrease of H/D_0 , similar to the cases in single-sheet clusters (Figure 5-22), while the dependence on L/D_0 is non-monotonic (the ratio fluctuates), something that shows that the H/D_0 plays a more important role on the breakup initiation time compared to the L/D_0 . The maximum ratio is equal to 1.19 and is encountered at $L/D_0=2$, $H/D_0=5$ and $We=45$, while the minimum is equal to 0.07 at $L/D_0=1.25$, $H/D_0=1.25$, $We=30$ and at $L/D_0=6$, $H/D_0=1.25$ and $We=30$.

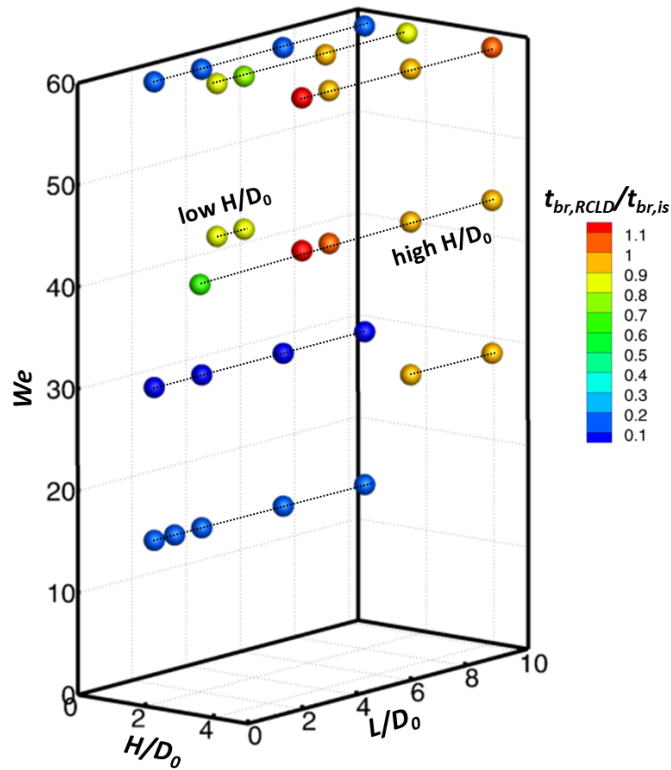


Figure 5-31: Ratio $t_{br,RCLD}/t_{br,is}$ as function of We , H/D_0 and L/D_0 .

5.4.2.2.4 Drag coefficient

The average drag coefficient is found for each simulated case using the same procedure as the one described in section 5.2.2.3.4, and the ratio $C_{d,RCLD}/C_{d,is}$ is presented in Figure 5-32, as function of We , H/D_0 and L/D_0 . The ratio increases with the decrease of H/D_0 , similar to the cases in single-sheet clusters (Figure 5-23), while for most cases it decreases with the decrease of L/D_0 , similar to the droplets in tandem formation (Figure 5-9). The maximum ratio is equal to 30.8 and is encountered at $L/D_0=9$, $H/D_0=1.25$ and $We=60$, while the minimum is equal to 0.62 at $L/D_0=1.25$, $H/D_0=5$ and $We=15$.

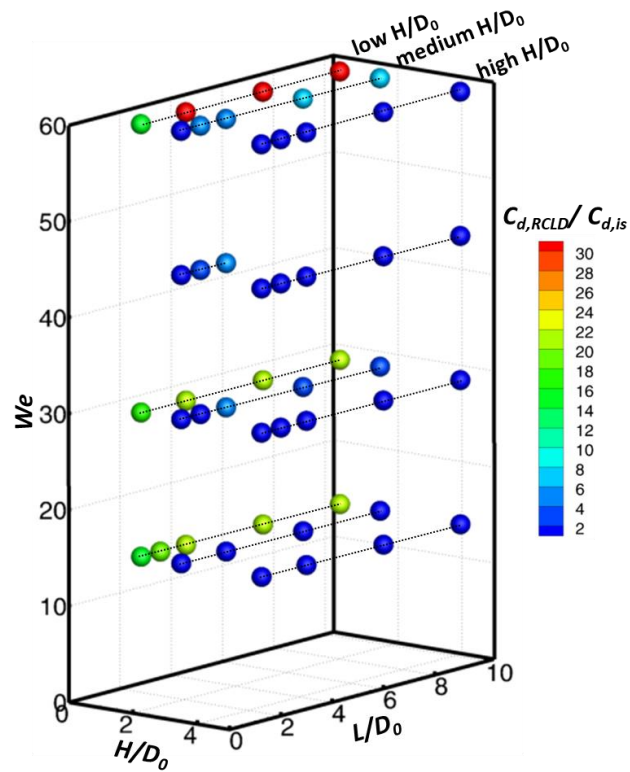


Figure 5-32: Ratio $C_{d,RCLD}/C_{d,is}$ as function of We , H/D_0 and L/D_0 .

5.4.2.3 Comparison between droplets in the three cluster formations (2-D results)

5.4.2.3.1 Droplet shapes

Figure 5-33 presents the temporal evolution of droplet shape as predicted by the 2-D axisymmetric simulation (3-D rotation) of droplets in: a) a multi-sheet cluster with $H/D_0=L/D_0=2$, b) a single-sheet cluster with $H/D_0=2$, c) tandem formation with $L/D_0=2$ and d) isolated formation; for all cases the We number is equal to 40. The first observation is that both the leading droplet in the tandem formation and the isolated one exhibit a quite similar evolution of droplet shape and experience the same breakup mode (multi-bag), as was discussed in section 5.2.2.1. The same holds true also for the leading droplet in the multi-sheet cluster and the droplet in the single-sheet cluster, which exhibit similar evolutions of droplet shape and experience shuttlecock breakup mode.

Turning now to the RCLD (multi-sheet cluster), RCD (tandem) (see Figure 5-2) and the droplet in the single-sheet cluster, these experience the same breakup mode, i.e. the shuttlecock; however, the RCD breaks up much slower than the other two, which exhibit similar breakup times. This indicates that the effect of parallel placement of the droplets is more dominant than the tandem one, for the examined conditions. As already discussed

in section 5.3.2.1, the main difference between the shape of the RCLD compared to that of the droplet in a single-sheet cluster, is that the former experiences a higher streamwise deformation, due to the presence of the upstream droplets. These affect the pressure field, as shown in Figure 5-34, which presents the contour of non-dimensional pressure ($= (P - P_\infty) / \frac{1}{2} \rho_g U_{d,0}^2$) for the multi-sheet cluster of Figure 5-33: in the RCLD an oblique pressure gradient is formed, which stretches the droplet towards a 45 degrees direction, similar to the RCD (section 5.2.2.1).

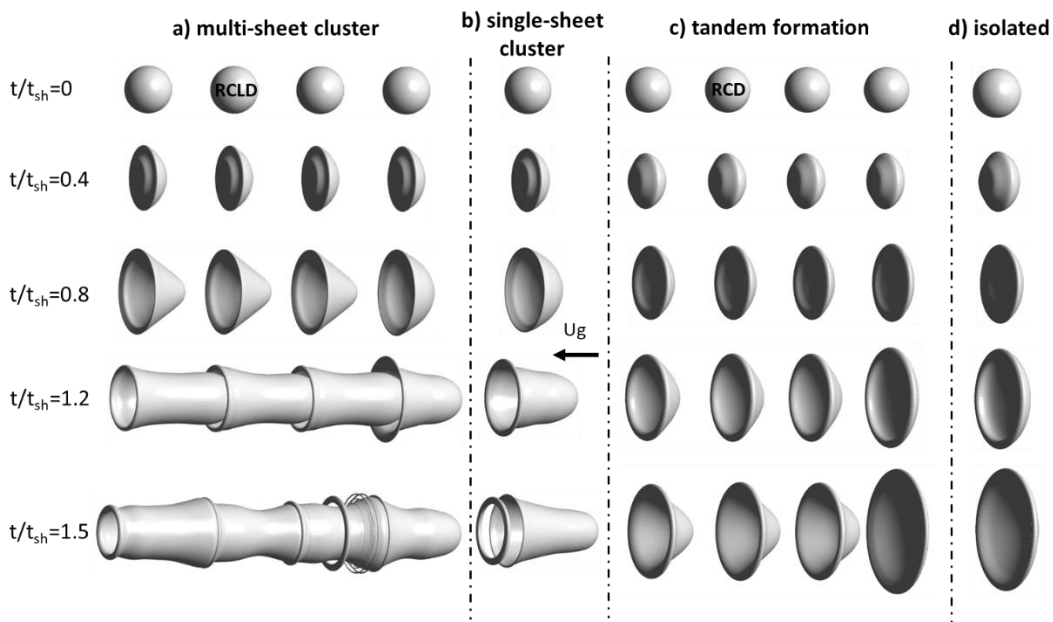


Figure 5-33: Temporal evolution of droplet shape as predicted by the 2-D axisymmetric simulation (3-D rotation) of droplets in: a) a multi-sheet cluster with $H/D_0=L/D_0=2$, b) a single-sheet cluster with $H/D_0=2$, c) tandem formation with $L/D_0=2$ and d) isolated formation ($We=40$).

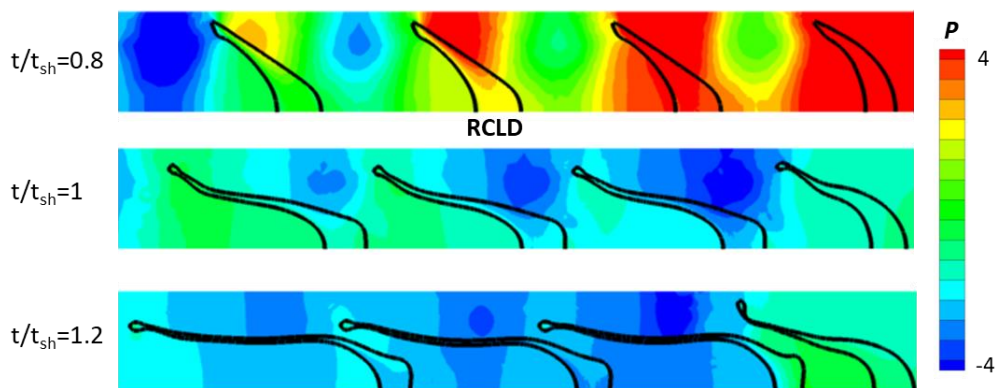


Figure 5-34: Dimensionless pressure contour for a multi-sheet droplet cluster with $H/D_0=L/D_0=2$ and $We=40$.

5.4.2.3.2 Droplet quantities

Figure 5-35 shows the temporal evolution of droplet velocity as predicted by the 2-D axisymmetric simulation of: a) an isolated droplet, b) the RCD ($L/D_0=2$), c) a droplet in single-sheet cluster ($H/D_0=2$) and d) the RCLD ($H/D_0=L/D_0=2$); for all cases $We=40$. The droplet in the single sheet-cluster shows the highest acceleration, while the RCD (tandem formation) shows the lowest, due to highest and lowest drag coefficients, respectively, as shown in Table 5.3; calculation has been done with the procedure of section 5.2.2.3.4.

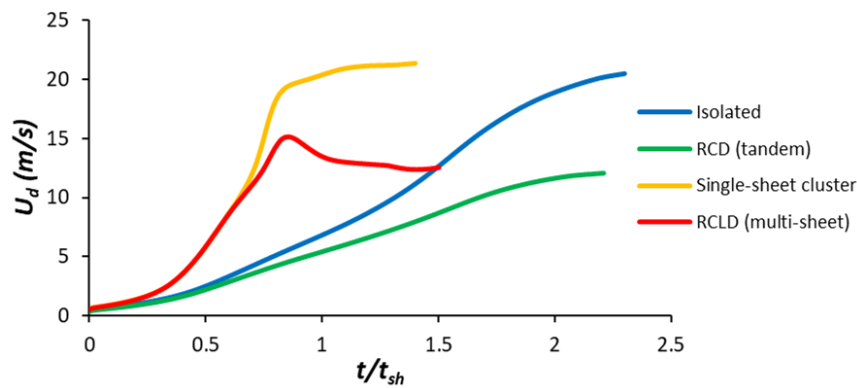


Figure 5-35: Temporal evolution of droplet velocity as predicted by the 2-D axisymmetric simulation of: a) an isolated droplet, b) the RCD ($L/D_0=2$), c) a droplet in single-sheet cluster ($H/D_0=2$) and d) the RCLD ($H/D_0=L/D_0=2$); for all cases $We=40$.

Table 5.3: Drag coefficients of an isolated droplet, the RCD, a droplet in a single-sheet cluster and the RCLD ($We=40$).

Formation	Cd
Isolated	0.85
RCD (tandem)	0.73
Single-sheet cluster	5.33
RCLD (multi-sheet)	2.52

Turning now to the droplet deformation, this is presented in Figure 5-36 for the four examined formations. The RCLD experiences the highest streamwise deformation, while the isolated droplet experiences the lowest. The former occurs due to two cumulative effects: i) the presence of the upstream droplets creates an oblique pressure field which stretches the droplet towards a 45 degrees direction (Figure 5-34), and, ii) the narrow gap between the droplets arranged parallel to the air flow, creates higher air velocities at the periphery of the droplet, compared to its center (Figure 5-17). On the other hand, for the same reasons, the RCLD experiences the lowest cross-stream deformation, while the isolated experiences the highest.

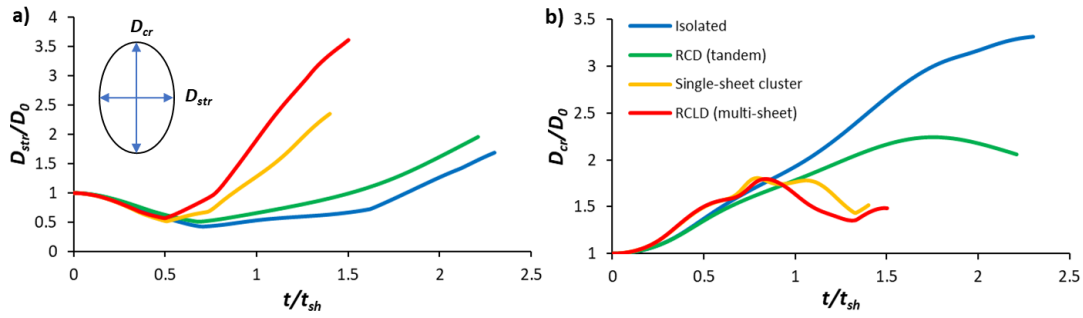


Figure 5-36: Temporal evolution of droplet deformation in both axes of: a) an isolated droplet, b) the RCD ($L/D_0=2$), c) a droplet in single-sheet cluster ($H/D_0=2$) and d) the RCLD ($H/D_0=L/D_0=2$); for all cases $We=40$.

Finally, Figure 5-37 presents the temporal evolution of droplet surface area for the examined formations. While the RCLD shows the highest rate of deformation, the maximum surface area is encountered in the isolated droplet. This occurs due to the breakup mode of the isolated droplet, which is multi-bag compared to shuttlecock in the rest, which gives higher maximum surface area due to the presence of the bags. The lowest surface area is encountered by the RCD, which is “covered” by the presence of the upstream droplets. It should be noted that for the same reason one would expect that the RCLD will have lower surface area compared to the single-sheet; however, this does not occur, since the presence of the upstream droplets enhances the, already present, stretching of the droplet, and therefore promotes the increase of surface area.

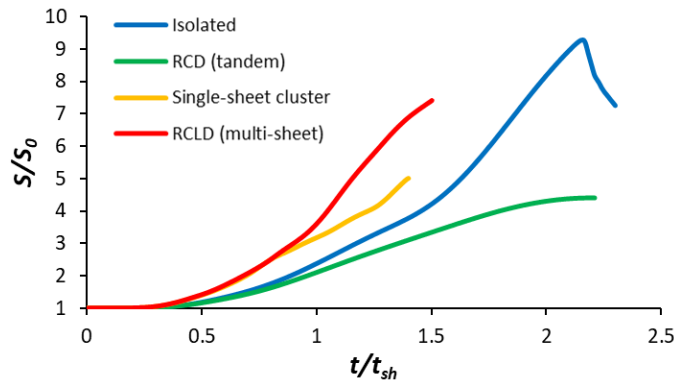


Figure 5-37: Temporal evolution of surface area of: a) an isolated droplet, b) the RCD ($L/D_0=2$), c) a droplet in single-sheet cluster ($H/D_0=2$) and d) the RCLD ($H/D_0=L/D_0=2$); for all cases $We=40$.

5.5 Conclusions

In this chapter, the breakup of droplet clusters was investigated by performing 2-D axisymmetric and 3-D simulations for the following droplet formations: i) tandem, ii) single-sheet clusters, and c) multi-sheet clusters. The examined We numbers ranged from

5 up to 60, while the non-dimensional streamwise (L/D_0) and cross-stream (H/D_0) droplet distances ranged from 1.25 up to 20.

It was found that for small droplet distances ($L/D_0 \leq 5$ or $H/D_0 \leq 5$) the droplets experience the so-called shuttlecock breakup mode, which is identified for the first time in the present work, and is characterized by an oblique peripheral stretching of the droplet. This is caused by an oblique pressure gradient created by the presence of the upstream droplets, as also by the high air velocities developed at the gap between the droplets, when arranged in parallel to the air flow (single- and multi-sheet clusters).

The parametric study showed that as the L/D_0 (streamwise distance) decreases, the drag coefficient and maximum surface area of the droplet also decrease, while the breakup initiation time and critical We increase. Regarding the H/D_0 (cross-stream distance), its decrease results in higher drag coefficients and lower breakup initiation times, while its effect on the maximum surface area depends on the We number. At very small streamwise droplet distances $H/D_0 < 1.5$, the critical We number of a droplet in a cluster becomes lower than that of an isolated droplet at the same conditions. In line with the above, the droplets in the single-sheet cluster were found to experience the highest drag coefficients of the three examined formations, as well as of an isolated droplet at the same conditions. On the other hand, the droplets in the tandem formation experience the lowest drag of the four. The third droplet of the row in the multi-sheet cluster formation was named as representative cluster droplet (RCLD), and it was found to experience the largest rate of streamwise deformation of the four, and the lowest cross-stream one. Overall, it was found that the droplets are affected by the presence of other droplets in the cross-stream direction for distances $H/D_0 \leq 5$, and in streamwise direction for distances $L/D_0 < 9$ (or higher for lower We).

Finally, correlations were provided based on the simulations for the prediction of the aforementioned quantities of the third droplet of the row in the tandem formation (representative chain droplet), as function of We and L/D_0 . The proposed correlations for the drag coefficient were used in a simplified OD model, similar to those utilized in Lagrangian numerical codes, to predict the temporal evolution of droplet velocity of a representative chain droplet, and the results showed good agreement with those of the CFD simulations.

Chapter 6

Analytical models for droplet deformation and breakup

6.1 Introduction

In this chapter, the developed/improved analytical models for droplet deformation and breakup are presented. These are: i) an improved TAB model, ii) a model based on the Navier-Stokes equations, named as M-NS, and iii) the unified secondary breakup model, which incorporates various models of the literature by using adjustable parameters (TAB, DDB, NLTAB and NS). The results of the models are compared against the results of CFD simulations for the droplet deformation of Diesel droplets in three breakup regimes: bag, multi-mode and sheet-thinning.

6.2 Mathematical models

6.2.1 Improved TAB model

In the TAB model the droplet deformation is described by a second-order differential equation similar to that of a mass-spring-damper system [95]:

$$m\ddot{x} = F - kx - d\dot{x} \quad (6-1)$$

, where x is the displacement of the drop equator from the spherical shape and m , F , k and d are the mass, external force, spring constant and damping constant, respectively. The external force acting on the droplet is the aerodynamic force, the spring constant represents the surface tension force and the damping constant the viscosity force, as presented in eq. (6-2):

$$\frac{F}{m} = C_F \frac{\rho_g U_{rel,0}^2}{\rho_L R_0} \quad \frac{k}{m} = C_k \frac{\sigma}{\rho_L R_0^3} \quad \frac{d}{m} = C_d \frac{\mu_L}{\rho_L R_0^2} \quad (6-2)$$

Substituting eq. (6-2) into (6-1) and introducing the non-dimensional numbers from equation (1-1), as well as the droplet deformation as $y=D_{cr}/D_0=x/R_0+1$, we get the final equation for the droplet deformation in eq. (6-3):

$$\ddot{y} + 4C_d \frac{Oh}{\sqrt{We}} \dot{y} + \frac{8C_k}{We} (y - 1) = 4C_F \quad (6-3)$$

The parameters of the improved TAB model (C_k and C_f) are found by fitting eq. (6-3) to the results for the temporal evolution of droplet deformation of a) the experimental studies of [16, 74, 76-78] (bag regime), and b) the results of the CFD simulations of Table 6.4 (multi-mode and sheet-thinning regimes), as presented in Table 6.1, along with those of the original TAB of [80]. The value of zero for the surface tension term C_k was found to fit better to the aforementioned group of results for $We \geq 60$, something that results in the negation of the surface tension term in the modified TAB model (eq. (6-3)). Thus, its solution for the droplet deformation results in an exponential function of time instead of an oscillation. The physical interpretation of this is that for high We numbers the aerodynamic forces are much higher than the surface tension forces, and therefore the latter can be neglected. Finally, the value of the viscosity parameter C_d is taken constant and equal to 10, in agreement with [82, 155]; this parameter is expected to be a function of Oh number, which has a constant low value in the examined cases and has a minor effect on the breakup process.

Table 6.1: Parameters of the original and improved TAB models.

Breakup mode	Original TAB			Improved TAB		
	C_d	C_f	C_k	C_d	C_f	C_k
Bag				10	$0.13 + 0.0026We$	$-1.32 + 0.12We$
Multi-mode	5	1/3	8	10	$0.46 + 0.0022We$	$7.87 - 0.13We, We < 60$
Sheet-thinning						0, $We \geq 60$

6.2.2 Modified model based on the Navier-Stokes equations (M-NS)

Initially, the viscous Navier-Stokes equations in cylindrical axisymmetric coordinates are employed (see Figure 6-1 for the definition of the droplet radius and rim thickness):

$$\rho_L \left(\frac{\partial u_r}{\partial t} + u_r \frac{\partial u_r}{\partial r} \right) = - \frac{\partial p}{\partial r} + \mu_L \left[\frac{1}{r} \frac{\partial}{\partial r} \left(r \frac{\partial u_r}{\partial r} \right) - \frac{u_r}{r^2} \right] \quad (6-4)$$

$$r \frac{\partial h}{\partial t} + \frac{\partial (r u_r h)}{\partial r} = 0 \quad (6-5)$$

Moreover, the mass conservation gives the rim thickness as:

$$h(t) = \frac{D_0^3}{6R^2} \quad (6-6)$$

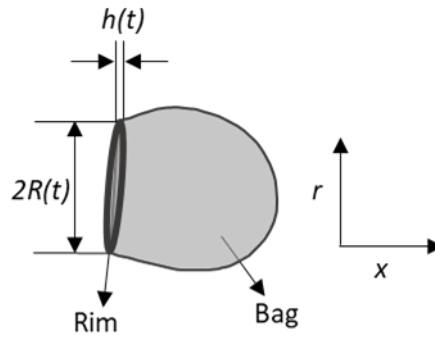


Figure 6-1: Definition of rim thickness and droplet radius in cylindrical coordinates.

The parameter u_r is found by substituting eq. (6-6) into (6-5) and solving for it:

$$u_r = \frac{r}{R} \frac{dR}{dt} \quad (6-7)$$

Eq. (6-4) requires the calculation of the pressure gradient (dp/dr). First, the normal stress balance across the interface is employed:

$$\sigma\kappa = T_{rr}(g) - T_{rr}(l) \quad (6-8)$$

$T_{rr}(l)$ and $T_{rr}(g)$ represent the normal stress components associated with the liquid and the surrounding gas, given by $-p_L(r) + 2\mu_L \frac{\partial u_r}{\partial r}$ and $-p_g(r)$, respectively. At $r=R$ equation (6-8) gives:

$$p_L(R) = p_g(R) + \sigma\kappa + 2\mu_L \frac{\partial u_r}{\partial r} \quad (6-9)$$

The gas pressure field around the droplet (p_g) can be estimated using the momentum and mass conservations in the gas phase, with the assumptions of inviscid flow, incompressible fluid and quasi-steady state. Moreover, the local gas flow is assumed to have the structure of a stagnation point: $U_x = -aU_x/D_0$, where a is an indicator of the rate of stretching. The resulting equation is (6-10):

$$p_g(r, x) = p_g(0) - \rho_g \frac{\alpha^2 U_0^2}{8D_0^2} r^2 + \rho_g \frac{\alpha^2 U_0^2}{8D_0^2} x^2 \quad (6-10)$$

At $x=0$ eq. (6-10) becomes:

$$p_g(r) = p_g(0) - \rho_g \frac{\alpha^2 U_0^2}{8D_0^2} r^2 \quad (6-11)$$

$p_g(0)$ is the stagnation pressure at $r = x = 0$, given by $p_g(0) = \rho_g U_0^2 / 2$. Substituting equations (6-11), (6-7) and the equation for the curvature $k = \left(\frac{h(t)}{2}\right)^{-1}$ into (6-9) the following equation is derived:

$$p_L(R) = p_g(0) - \rho_g \frac{\alpha^2 U_0^2}{8D_0^2} R^2 + \frac{2\sigma}{h} + 2\mu_L \frac{\partial u_r}{\partial r} \quad (6-12)$$

The pressure gradient can finally be calculated using eqs. (6-12) and (6-6) as:

$$\frac{\partial p}{\partial r} \approx \frac{p_L(R) - p_g(R)}{R} = \frac{1}{R} \left(-\rho_g \frac{\alpha^2 U_0^2}{8D_0^2} R^2 + \frac{12\sigma}{D_0^3} R^2 + \frac{2\mu_L}{R} \frac{dR}{dt} \right) \quad (6-13)$$

Substituting eqs. (6-13) and (6-7) into (6-4) we get:

$$\rho_L \frac{r}{R} \frac{d^2 R}{dt^2} = -\frac{1}{R} \left(-\rho_g \frac{\alpha^2 U_0^2}{8D_0^2} R^2 + \frac{12\sigma}{D_0^3} R^2 + \frac{2\mu_L}{R} \frac{dR}{dt} \right) \quad (6-14)$$

The integration from $r=0$ to $r=R$ gives:

$$\frac{d^2 R}{dt^2} = \left(\rho_g \frac{\alpha^2 U_0^2}{\rho_L 4D_0^2} - \frac{24\sigma}{\rho_L D_0^3} - \frac{4\mu_L}{\rho_L R^3} \frac{dR}{dt} \right) R \quad (6-15)$$

Finally, the non-dimensional parameters are introduced: We , Oh , $y = R/(D_0/2)$, $t^* = t/t_{sh} \Rightarrow t = t^* \frac{D_0 \sqrt{\varepsilon}}{U_0}$, and the final differential equation for the droplet deformation is given in (6-16):

$$\ddot{y} + 16 \frac{Oh}{\sqrt{We}} \frac{\dot{y}}{y^2} + \frac{24}{We} \dot{y} = \frac{\alpha^2}{4} y \quad (6-16)$$

This model has been originally developed in [76] and is called bag-NS for the remainder of the thesis. The multiplier of the viscosity term (2nd term from the left of eq. (6-16)) is found equal to 16 in the current work, while in [76] it was estimated equal to 8, probably due to a miscalculation in the algebraic manipulations. Either way, the contribution of this term in the calculation of the droplet deformation is low for the current examined conditions of low Oh numbers ($Oh < 0.04$), and thus it is not affecting the results. However, its contribution is expected to increase at higher Oh numbers.

In this work a numerical improvement of the bag-NS breakup model is introduced: the pressure term is considered a function of y^n instead of y (4th term from the left of eq. (6-17)). Eq. (6-17) is a second-order non-linear differential equation with no analytical solution, the numerical solution of which is obtained in this work using an explicit 4th order Runge-Kutta method [156, 157].

$$\ddot{y} + 16 \frac{Oh}{\sqrt{We}} \frac{\dot{y}}{y^2} + \frac{24}{We} y = \frac{\alpha^2}{4} y \quad (6-17)$$

The parameter α is called rate of stretching, while the parameter n is called pressure exponent and has been introduced in the present work to provide a more flexible numerical consideration of the pressure contribution. For $n \geq 1$ the deformation grows exponentially in time (note that $n=1$ corresponds to the original model of [76], as shown in Table 6.2), while for $n < 1$ the deformation becomes oscillatory. More specifically, for $n=0$ the equation becomes similar to that of the TAB model, while for $n=-1$ it becomes similar to that of the NLTAB, since the pressure term is proportional to $1/y$. For each breakup mode, the value of n that gives the higher coefficient of determination (R^2) is selected, when compared to the results of the experimental studies of [16, 74, 76-78] for the bag regime, and the CFD simulations of Table 6.4 for the multi-mode and sheet-thinning regimes, as shown in Table 6.2. Finally, instead of using a constant value for the parameter α the current study proposes this to be a function of the We number for each breakup mode (bag, multi-mode and sheet-thinning). α is found for each We number by fitting eq. (6-17) to the results of the experimental studies of [16, 74, 76-78] for the bag breakup regime, while for the multi-mode and sheet-thinning regimes the results of the CFD simulation are employed instead; the $\alpha=f(We)$ function is found by assuming a linear dependence on the We number. It should be mentioned that the equation of α in the bag breakup regime gives a value of α equal to 2.88 for $We=15$, which is close to the value of 2.83 proposed by [76] for the same We .

Table 6.2: Parameters of the bag-NS and M-NS models.

Breakup mode	Original bag-NS		Proposed M-NS	
	n	α	n	α
Bag	1	2.83	1	$3.6 - 0.048We$
Multi-mode	-	-	-0.5	$3.35 + 0.0032We$
Sheet-thinning	-	-	2	$2.35 + 0.0042We$

6.2.3 Unified secondary breakup model

In order to develop the unified secondary breakup model a similar procedure to that of Schmehl at al. [90] for the derivation of the NLTAB model is followed, but the appearing terms are expressed in a more generic way. This is accomplished by utilizing basic

equations, (e.g. the work is given by the multiplication of a force with an area), along with reference values for these variables (e.g. reference force and area). In addition, adjustable parameters are introduced to account for the effects of physical parameters/mechanisms that are not included in the equations, since they are expressed by using reference magnitudes, such as the internal flow in the droplet and the pressure distribution around it.

For convenience the mechanical energy balance of the droplet is employed first, which is written in rate form in eq. (6-18):

$$\frac{dE_d}{dt} = \dot{W}_{press} - \dot{W}_{vis,d} \quad (6-18)$$

The droplet energy consists of three parts: a) the kinetic translational energy, b) the surface energy, and c) the kinetic energy as the droplet deforms. It should be noted that heat transfer effects could be also added in eq. (6-18), which are not within the scope of the current work and therefore are neglected. It is mathematically proved that the translational droplet energy cancels the work of pressure forces in the direction of the flow, using the droplet momentum equation in the streamwise direction. Thus, the translational terms will not be included.

Starting with the kinetic energy this can be calculated as:

$$E_{kin,d} = f_{kin} \frac{1}{2} m_L U_{def,y}^2 = f_{kin} \frac{1}{2} \rho_L \frac{\pi D_0^3}{6} \left(\frac{dR}{dt} \right)^2 \quad (6-19)$$

The term $U_{def,y}=dR/dt$ denotes the deformation velocity in the cross-stream direction, and serves as a scaling velocity for the calculation of the kinetic energy, while the coefficient f_{kin} is used to include the secondary effects appearing during droplet deformation. These are: i) the secondary kinetic energy arising from the axial (transverse) deformation, ii) the variation of liquid velocity along the cross-stream diameter (it is 0 at the symmetry axis and dR/dt at the peripheral tip), and iii) the internal liquid flow/circulation. In the TAB and DDB models the value of f_{kin} is equal to 1, while in the NLTAB it is a decreasing function of y (see Table 6.3).

The rate of kinetic energy is:

$$\frac{dE_{kin,d}}{dt} = \frac{1}{2}\rho_L \frac{\pi D_0^3}{6} \left(f_{kin} 2 \frac{dR}{dt} \frac{d^2R}{dt^2} + \frac{df_{kin}}{dR} \left(\frac{dR}{dt} \right)^3 \right) \quad (6-20)$$

And by introducing the non-dimensional numbers: $y = \frac{2R}{D_0} \rightarrow R = y \frac{D_0}{2}$ (see Figure 1-3) and $t^* = \frac{t}{D_0 \sqrt{\varepsilon}} U_0 \rightarrow t = t^* \frac{D_0 \sqrt{\varepsilon}}{U_0}$, the equation becomes ($\dot{y} = \frac{dy}{dt^*}$):

$$\frac{dE_{kin,d}}{dt} = \frac{2}{3} \left(\frac{\rho_g \pi D_0^2 U_0^3}{16 \sqrt{\varepsilon}} \right) \left(f_{kin} \dot{y} \ddot{y} + \frac{1}{2} \frac{df_{kin}}{dy} (\dot{y})^3 \right) \quad (6-21)$$

Next, the rate of surface energy is given in eq. (6-22):

$$\frac{dE_{surf,d}}{dt} = \frac{d}{dt} (\sigma S) = \sigma \frac{dS}{dy} \frac{dy}{dt} = \sigma \pi D_0^2 \frac{dS^*}{dy} \frac{dy}{dt} \quad (6-22)$$

, where S^* represents the dimensionless droplet surface ($S^* = S/\pi D_0^2$).

Introducing the non-dimensional time (t^*) the equation becomes:

$$\begin{aligned} \frac{dE_{surf,d}}{dt} &= \sigma \pi D_0^2 \frac{dS^*}{dy} \frac{dy}{dt^* \frac{D_0 \sqrt{\varepsilon}}{U_0}} = \frac{\sigma \pi D_0 U_0}{\sqrt{\varepsilon}} \frac{dS^*}{dy} \dot{y} \\ &= \left(\frac{\rho_g \pi D_0^2 U_0^3}{16 \sqrt{\varepsilon}} \right) \frac{16}{We} \frac{dS^*}{dy} \dot{y} \end{aligned} \quad (6-23)$$

In eq. (6-23) the term dS^*/dy is a characteristic of the droplet shape and depends on the breakup mode and phase (e.g. flattening phase, bag creation, etc). The majority of the breakup models assumed ellipsoid shape (either cylinder or axisymmetric, see Table 1.8) and provided the term dS^*/dy as a function of the instantaneous deformation y , using either a simplified analytic formula or a polynomial fitting. Although the assumption of an ellipsoidal shape is an oversimplification it reflects with low error the droplet surface area when compared with the results of CFD (comparison not presented here).

For the pressure work term it is assumed that this is obtained by multiplying a reference force (F_{ref}) with the reference deformation velocity $U_{def,y}$:

$$\dot{W}_{press} = f_{press} \cdot F_{ref} \cdot U_{def,y} = f_{press} \frac{1}{2} \rho_g u_{rel}^2 \frac{\pi D_0^2}{4} \frac{dR}{dt} \quad (6-24)$$

The introduction of non-dimensional numbers: y , t^* and $u_{rel}^* = \frac{u_{rel}}{U_0}$, gives:

$$\dot{W}_{press} = f_{press} \left(\frac{\rho_g U_0^3 \pi D_0^2}{16\sqrt{\varepsilon}} \right) u_{rel}^{*2} \dot{y} \quad (6-25)$$

The coefficient f_{press} is used to account for the effect of pressure distribution around the droplet, as also the change of frontal area during droplet deformation. In the NLTAB model this term is proportional to \dot{y}/y , while in the model of Rimbert et al. [89] is proportional to $K_p(y) \cdot \dot{y}$, where K_p is a polynomial function of y (see Table 6.3). The term u_{rel}^* includes the effect of change of the relative drop-gas velocity; the inclusion of this effect implies that an additional equation has to be solved for the droplet motion (see [117]), while ignoring this effect, implies that u_{rel}^* is unity. The CFD simulations showed that $u_{rel}^* \geq 0.8$ for all examined cases even at the instance of breakup, when u_{rel}^* is minimum.

Finally, for the viscous dissipation term the approximation of NLTAB [90] is used (n is the unit vector in the direction of y):

$$\dot{W}_{vis,d} = f_{vis} 12\mu_L \left(\frac{\partial u_{cm}}{\partial n} \right)^2 \frac{\pi D_0^3}{6} = f_{vis} 2\mu_L \left(\frac{1}{y} \frac{dy}{dt} \right)^2 \pi D_0^3 \quad (6-26)$$

With the introduction of the non-dimensional time (t^*), and the numbers We and Oh , the equation becomes:

$$\dot{W}_{vis,d} = f_{vis} \left(\frac{\rho_g \pi D_0^2 U_0^3}{16\sqrt{\varepsilon}} \right) 32 \frac{Oh}{\sqrt{We}} \left(\frac{\dot{y}}{y} \right)^2 \quad (6-27)$$

The coefficient f_{vis} is used to account for the effect of energy dissipation in the streamwise direction.

By substituting equations (6-21), (6-23), (6-25) and (6-27) into (6-18), the final expression for y is derived in (6-28). One more coefficient has been added to the equation

for the effect of surface energy (f_{st}), and all constants have been incorporated inside the parameters.

$$\left(f_{kin}\dot{y} + \frac{1}{2} \frac{df_{kin}}{dy} \dot{y}^2 \right) + f_{vis} \frac{Oh}{\sqrt{We}} \frac{\dot{y}}{y^2} + \frac{f_{st}}{We} \frac{dS^*}{dy} = f_{press} u_{rel}^{*2} \quad (6-28)$$

By giving the appropriate values to the parameters f_{kin} , f_{vis} , f_{st} , f_{press} , dS^*/dy and u_{rel}^* , equation (6-28) matches the equations of the models TAB, NLTAB, DDB and M-NS, as shown in Table 6.3. Finally, the values of the coefficients can be estimated based on the results of the CFD simulations of Table 6.4, as presented in Table 6.3, as well. The coefficients c_1 , c_2 and c_3 are functions of the We number and could be found with a similar procedure as the one followed for the estimation of the coefficients of the improved TAB and M-NS models (Table 6.1 and Table 6.2). However, this is a difficult procedure and is still a work in progress, while instead the results of the unified secondary model are presented for specific c_1 , c_2 and c_3 coefficient corresponding to the We numbers of 15, 20, 23, 60, 80 and 250, as presented in Section 6.4.

Table 6.3: Parameters of the unified secondary breakup model to match the various models of the literature.

	TAB	NLTAB	DDB	Bag-NS	M-NS	CFD
f_{kin}	1	$\frac{\pi^2 + \frac{16}{y^6}}{\pi^2 + 16}$	1	1	1	$c_1 e^{c_2(y-1)^{c_3}}$
f_{vis}	$4y^2 C_d, C_d=5$	40	$9\pi^2$	16	16	-
f_{st}	$8C_k, C_k=8$	29	$\frac{27\pi^2}{2}$	24	24	16
f_{press}	$4C_F, C_F=1/3$	$\frac{2C_2}{y}, C_2=2/3$	$9\pi/8$	$\frac{\alpha^2}{4}y,$ $a = 2\sqrt{2}$	$\frac{\alpha^2}{4}y^n,$ $a = f(We)$	$c_1 e^{c_2(y-1)^{c_3}}$
$\frac{dS^*}{dy}$	$y - 1$	Ellipsoid	$(1 - 2y^{-6})y$	y	y	Polynomial function of y
u_{rel}^*	1	1	1	1	1	1

6.2.4 Breakup condition

Most breakup models of the literature assume a constant critical deformation (onset of breakup) in the range of 1.8 to 2.1 (see Table 1.8), with the exception of the BTB model, in which the critical deformation is a function of We . In this study it is assumed that the breakup occurs when either the maximum deformation is reached ($\dot{y}=0$) or when a critical deformation is exceeded ($y_{cr}=3.5$), whichever comes first. The condition of $y_{cr}=3.5$ is

calculated based on the results of the CFD simulations for a range of We numbers from 20 up to 350, and it is also in agreement with the experimental data of [74] for a We number equal to 20, as shown in Figure 6-2. The critical deformation of the various models of the literature is presented in the figure as well.

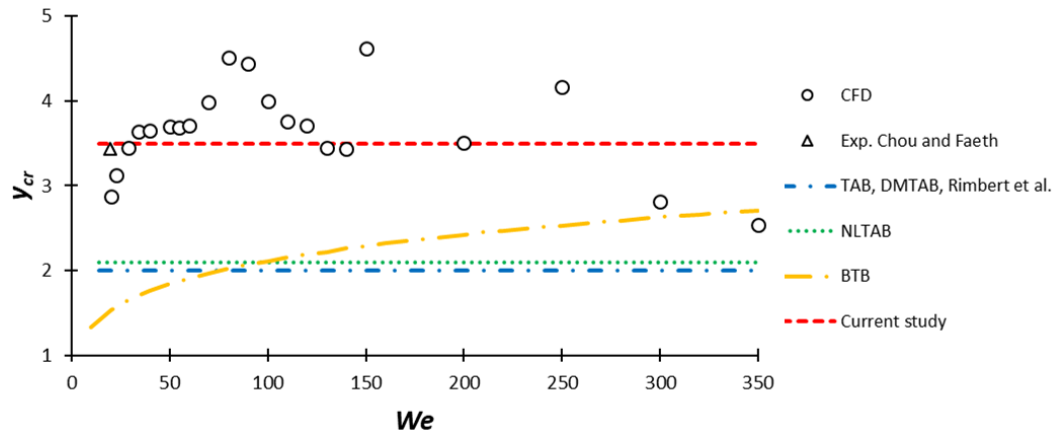


Figure 6-2: Critical deformation as estimated by the CFD simulations and the experiments of [74], as well as the assumptions of the various breakup models.

6.3 Computational setup and examined conditions of the CFD simulations

The CFD simulations that are utilized for estimating the parameters of the various models as well as for comparison with their results have been performed using the 2-D axisymmetric computational domain of Figure 3-1a (section 3.2.1). The liquid is Diesel (properties of Table 3.1), while the surrounding gas is air at temperature of 293.15K and pressure of 1bar. Although Diesel is utilized as test fuel in the current work, the results can be considered valid for low viscosity fuels as long as the Ohnesorge number is kept below 0.1 [4]. The same is true for the effect of ambient pressure or equivalently that of the density ratio, which becomes important approximately below 32 [27, 128]. Both the properties of Diesel and air as well as the droplet diameter are based on [18] (see Table 3.1 of section 3.2.1). The corresponding non-dimensional numbers are: $\epsilon=678$, $Oh=0.038$ and $N=117$. The high density ratio (ϵ) and low Oh number ensure that their effect is minimized, focusing only on the effect of We number. By altering the gas velocity, the resulting We numbers range from 20 up to 350, resulting in 21 simulations in the three

breakup regimes, i.e. those of bag, multi-mode and sheet-thinning, as shown in Table 6.4. The corresponding Re numbers range from 531 to 2221.

Table 6.4: Examined cases for comparison with the analytical models

Case	$U_{g,0}$ (m/s)	We	Re	Oh	ε	Ma
1	40.8	20	531	0.038	678	0.05
2	43.7	23	569	0.038	678	0.05
3	49.1	29	639	0.038	678	0.05
4	53.2	34	692	0.038	678	0.05
5	57.7	40	751	0.038	678	0.06
6	64.5	50	839	0.038	678	0.06
7	67.6	55	880	0.038	678	0.06
8	70.6	60	920	0.038	678	0.07
9	76.3	70	993	0.038	678	0.07
10	81.5	80	1062	0.038	678	0.08
11	86.5	90	1126	0.038	678	0.09
12	91.2	100	1187	0.038	678	0.10
13	95.6	110	1245	0.038	678	0.11
14	99.9	120	1300	0.038	678	0.12
15	103.9	130	1354	0.038	678	0.12
16	107.9	140	1405	0.038	678	0.13
17	111.7	150	1454	0.038	678	0.16
18	128.9	200	1679	0.038	678	0.18
19	144.1	250	1877	0.038	678	0.21
20	157.9	300	2056	0.038	678	0.23
21	170.6	350	2221	0.038	678	0.24

6.4 Results – comparison of analytical models with CFD simulations

The temporal evolution of droplet deformation can be calculated using the three models (improved TAB, M-NS and unified) with their respective equations and parameters: i) improved TAB model using eq. (6-3) and the parameters of Table 6.1, ii) M-NS model using eq. (6-17) and the parameters of Table 6.2 and iii) unified secondary breakup model using eq. (6-28) and the parameters of Table 6.3. The results are presented in the following sub-sections as calculated by the two models in the bag, multi-mode and sheet-thinning regimes, along with the results of experimental studies (bag breakup regime) and those of the CFD simulations (multi-mode and sheet-thinning regimes).

6.4.1 Bag breakup regime – $We=10-20$

The results of three breakup models (improved TAB, M-NS and unified) are illustrated in Figure 6-3 for two We numbers, 15 and 20, in the bag breakup regime, along with those of the experimental studies for the same We numbers [16, 74, 76-78]. The TAB and M-NS models show a good agreement with the experimental data for both cases, while the unified model deviates a bit. This is due to the fact that the unified model is based on the CFD simulations, which also do not exactly match the experiments. In addition, the TAB model predicts lower values for the deformation compared to the M-NS model at higher $t^*(\geq 2.5)$, owing to the assumption that the droplet deformation is modeled as an oscillation in contrast to the exponential behavior of M-NS. It should be noted that the experimental data of Chou and Faeth [74] exhibit a fluctuation for the case of $We=20$ at $t^*\geq 2$, something that pertains to a combined exponential and oscillatory droplet deformation. This behavior is also observed in the simulations of Figure 6-4 and Figure 6-5, and it is something that has not been reported before in the literature. Nevertheless, the exponential part seems to dominate, while further experimental and numerical studies are required to verify this observation.

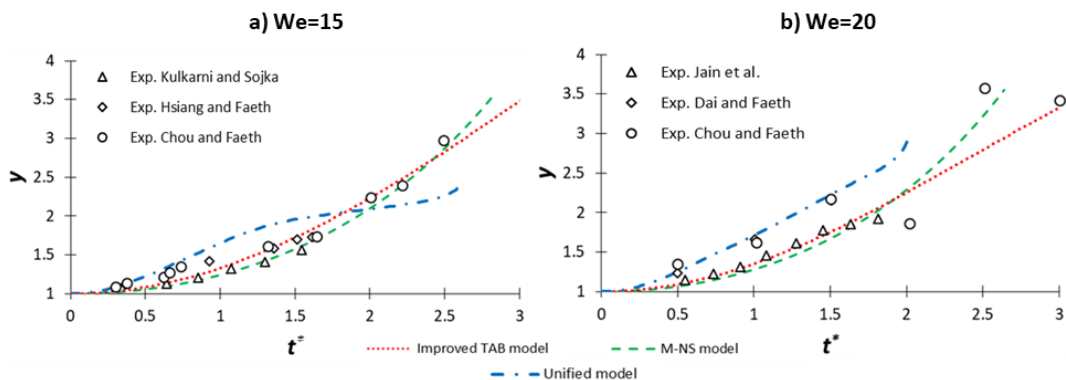


Figure 6-3: Temporal evolution of droplet deformation as predicted by the three models (improved TAB, M-NS and unified) as well as the experimental data from the literature for a) $We=15$ and b) $We=20$.

6.4.2 Multi-mode breakup regime – $We=21-65$

The results of the three breakup models (improved TAB, M-NS and unified) are presented in Figure 6-4 for two We numbers, 23 and 65, in the multi-mode regime, along with those of the simulations for the same We numbers. For the case of $We=60$ the results of all models are almost identical, while for $We=23$ the unified model deviates from the other two after $t^*\approx 2$. The latter occurs because the TAB and M-NS models estimate the

droplet deformation as an oscillation in this regime, while the unified model predicts an exponential behavior. The agreement is good overall between the models and the simulations, apart from the prediction of a slightly higher breakup initiation time in the TAB and M-NS models for the case of $We=23$. This is attributed to the occurrence of breakup at the time when $\dot{\gamma}=0$ and not at $\gamma_{cr}=3.5$.

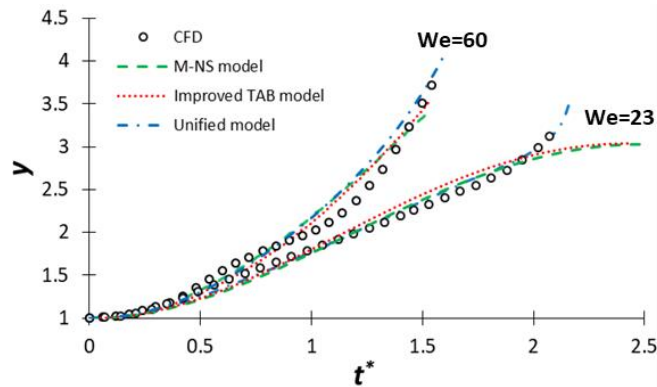


Figure 6-4: Temporal evolution of droplet deformation as predicted by the three models (improved TAB, M-NS and unified) along with the results of the simulations for a) $We=23$ and b) $We=60$.

6.4.3 Sheet-thinning breakup regime – $We=66-350$

In Figure 6-5, the results of the three breakup models (improved TAB, M-NS and unified) are presented for two We numbers (80 and 250) in the sheet-thinning regime, along with those of the simulations for the same We . Good agreement is observed again for all models, although a slight underestimation of γ_{cr} is noticed for both cases. In addition, the results of the unified and M-NS models are closer to those of the simulations due to their steeper inclination.

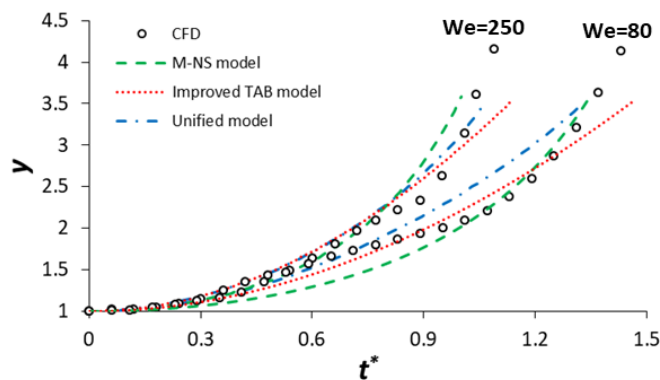


Figure 6-5: Temporal evolution of droplet deformation as predicted by the three models (improved TAB, M-NS and unified) along with the results of the simulations for two We numbers in the sheet-thinning regime (80 and 250).

6.5 Conclusions

The results of the simulations were utilized to assess the performance of the three analytical droplet breakup models developed/improved as part of this work: i) improved TAB, ii) M-NS and iii) unified secondary breakup model. Regarding the prediction of droplet deformation, all models showed good agreement against experimental data in the bag breakup regime and CFD simulations in the multi-mode and sheet-thinning regimes, with the exception of the unified model, which deviates a bit from the experimental data in the bag breakup regime. This is attributed to the derivation of its parameters in this regime using the CFD simulations instead of the experimental data. The best performance overall was achieved by the M-NS model. These models can be used in Eulerian-Lagrangian CFD codes for the simulations of sprays of low Oh numbers (low viscosity fuels), high ε and for isolated droplets, since the proposed parameters and breakup conditions are valid for these conditions.

Chapter 7

Conclusions and future work

7.1 Conclusions

The goal of this thesis was to investigate numerically the breakup of isolated droplets and droplets in clusters formations in representative engine conditions, with the aim of, on the one hand, shedding light in cases that had not been examined before, and, on the other, to provide correlations for the prediction of key droplet quantities. Initially, a parametric study for the Ohnesorge (Oh) number and density ratio (ϵ) was performed with isolated droplets, which revealed that the increase of Oh resulted in a shifting of the breakup mode from bag and multi-bag to oscillatory deformation without breakup, while the sheet-thinning regime remained unchanged. Moreover, it resulted in a decrease in the rate of deformation, liquid surface area and drag coefficient, while the breakup initiation time increased, implying that the breakup process is hindered when using high viscous fuels, such as HFO. Regarding the effect of ϵ , its increase resulted in the shifting of breakup mode from deformation to bag as also in the decrease of the drag coefficient, while the temporal evolution of liquid surface area remained unchanged. Based on these results, correlations were proposed for the prediction of breakup initiation time and drag coefficient of an isolated droplet as function of the non-dimensional numbers.

As a next step, simulations were performed with droplet clusters in three formations: i) tandem, ii) infinite single-sheet, and iii) infinite multi-sheet. A new breakup mode was identified, termed as shuttlecock, which is characterized by an oblique peripheral stretching of the droplet and is encountered at small droplet distances ($L/D_0 \leq 5$ or $H/D_0 \leq 5$). The parametric study for the We number and the initial droplet distance revealed that the decrease of L/D_0 (streamwise distance) results in a decrease in the drag coefficient and maximum surface area of the droplet, while the breakup initiation time and critical We increase. Conversely, the decrease of H/D_0 (cross-stream distance) results in higher drag coefficients and lower breakup initiation times, while its effect on the maximum surface area depends on the We . Moreover, it was found that at small cross-stream droplet distances ($H/D_0 < 1.5$) the critical We number of a droplet in a cluster becomes lower than that of an isolated droplet at the same conditions. In agreement with the aforementioned,

the droplets in the single-sheet cluster experience the highest drag coefficients of the three examined formations, as well as of an isolated droplet at the same conditions, while the droplets in tandem formation experience the lowest drag. The third droplet of the row in the multi-sheet cluster formation was named as representative cluster droplet (RCLD), and it was found to experience the largest rate of streamwise deformation of the four, and the lowest cross-stream one. Overall, it was found that the droplets are affected by the presence of other droplets in the streamwise direction for distances $L/D_0 < 9$ (or higher for lower We) and in the cross-stream one for $H/D_0 \leq 5$. Finally, the simulations were utilized to propose correlations for the prediction of the aforementioned quantities of the third droplet of the row in the tandem formation, which is named as representative chain droplet (RCD), as function of We and L/D_0 . The correlations for the drag coefficient were utilized in a simplified 0-D model, similar to those utilized in Lagrangian numerical codes, to predict the temporal evolution of droplet velocity of the RCD with acceptable accuracy, when compared to the CFD results.

In the final chapter of the thesis, three analytical droplet breakup models were developed/improved/modified as part of this work: i) improved TAB, ii) modified model based on the Navier-Stokes (M-NS), and iii) unified secondary breakup model. The results of the models regarding the prediction of droplet deformation in the three main breakup regimes (bag, multi-mode and sheet-thinning) were compared against experimental data and CFD simulations showing good agreement, apart from a small deviation of the unified model in the bag breakup regime. The best performance overall was achieved by the M-NS model. These models along with the developed correlations for the prediction of droplet quantities can be utilized in Eulerian-Lagrangian CFD codes for the simulations of sprays consisting of millions of droplets, providing a better estimation for the droplet quantities compared to the existing correlations, which have been developed for isolated droplets in atmospheric conditions.

7.2 Future work

Although the main goal of this work was achieved, i.e. to simulate conditions of droplet breakup at representative engine conditions and to propose correlations based on them for the prediction of key droplet quantities, some further research is necessary before the subject is considered totally explored. Based on the results of the current work the main points are summarized as:

- The CFD model was validated against experimental data for isolated droplets, however, it was utilized also to simulate the breakup of droplet clusters. Therefore, although the physical process is the same between one and more droplets, a further comparison with experimental data with droplet clusters would be insightful. This requires available data from experiments, as well as a large computational cost, since 3-D simulations of more than one droplet are required.
- The effect of evaporation is neglected in the current work, since focus is given on the aerodynamic breakup. However, in realistic fuel applications simultaneous breakup and evaporation occur, which might have a mutual effect. The later requires models for high pressure evaporation, which should be implemented in the CFD model.
- The diameter of the micro-droplets that appear in the simulations of high-Mach numbers are user-defined, while in reality this should be a product of the physical process. This was not possible with the current model of FLUENT (VOF-to-DPM) and perhaps a different model is needed (Euler-Euler etc) or a modification of the existing one through UDFs, which was not possible with the current version (v19.2.). If this is realized variables such as the particle size distribution can be measured in the simulations, which is of utmost importance in fuel sprays.
- Correlations for the prediction of key droplet quantities were provided only for isolated droplets and droplets in tandem formations. In order to be more relevant for spray application, correlations for single- and multi-sheet clusters should also be provided, which, however, is difficult since the dependence of some droplet quantities on the cross-stream droplet distance (H/D_0) is non-monotonic, making it difficult to propose functions that can describe it. Moreover, the prediction of the frontal area in the drag coefficient can be improved by utilizing analytical droplet deformation models, instead of a linear approximation.
- Other formations of droplets clusters should be examined, in which the droplets are placed at angles different than the 90° (parallel) and 180° (tandem), as also different droplet shapes than the spherical, such as elliptical.

- Finally, the examined analytical models for droplet deformation and breakup are valid for low Oh numbers, high ε and for isolated droplets, while further modifications are necessary to incorporate the effect of these parameters into the models. This is not an easy task, since the collaborative work of theoretical, numerical and experimental studies is required. In addition, the parameters of the unified secondary breakup model should be estimated as function of the non-dimensional numbers utilizing the results of CFD simulations.

Appendix A. Difference between the RCD of the current work with that of a seven-droplet chain

In order to estimate the difference between the RCD considered in this work with that of a seven-droplet chain, which is more representative of an infinite array of droplets, a simulation is performed with seven droplets at $We=40$ and $L/D_0=2$. Figure A-1 depicts the shapes of the droplets at the time instance of $t/t_{sh}=2.1$, which corresponds to the time of breakup of the leading droplet. It is evident that the shapes of the droplets 3 to 6 are nearly identical. Moreover, the values of the drag coefficient and maximum surface area of the droplets 4 and 5, which can be considered as representative in the seven-droplet chain, are very close and higher than those of the RCD up to 13.8% and 12.7%, respectively. Nevertheless, these differences are expected to decrease at higher We numbers and larger L/D_0 . The simulation of four droplets is chosen in the current study instead of seven, because it is more suitable for parametric studies, since the computational cost for the simulation of seven droplets is increased by approximately 75% compared to that of four.

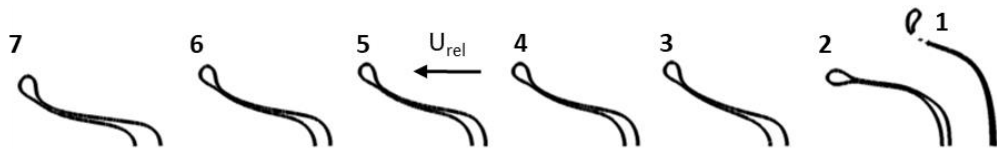


Figure A-1: Droplet shapes at the time instance of $t/t_{sh}=2.1$ from the simulation of a chain of seven droplets arranged in tandem. $We=40$ and $L/D_0=2$.

Publications

During my 3-year research I had the opportunity to travel, participate and present my ongoing work in international conferences, while I was fortunate to publish my findings in well-respected international scientific journals. The list of my achievements is given below:

Conferences (oldest first)

1. D. Stefanitsis, G. Strotos, N. Nikolopoulos and M. Gavaises, 2017, "Numerical investigation of the aerodynamic breakup of a droplet cluster", IICR 2019, Chania, Greece (poster and presentation).
 2. D. Stefanitsis, G. Strotos, N. Nikolopoulos, E. Kakaras and M. Gavaises, 2018, "Numerical examination of the aerodynamic breakup of droplets in chain formation", ICLASS 2018, Chicago, USA (paper and presentation).
 3. D. Stefanitsis, I. Malgarinos, G. Strotos, N. Nikolopoulos, E. Kakaras and M. Gavaises, 2017, "Numerical investigation of the aerodynamic breakup of Diesel droplets under various gas pressures", ILASS Europe 2017, Valencia, Spain (paper and presentation).
 4. D. Stefanitsis, I. Malgarinos, G. Strotos, N. Nikolopoulos, E. Kakaras and M. Gavaises, 2017, " Numerical investigation of the aerodynamic droplet breakup of viscous fuels", IICR 2016, Chania, Greece (poster).
-

Journal Papers (oldest first)

1. D. Stefanitsis, G. Strotos, N. Nikolopoulos, E. Kakaras and M. Gavaises, 2019, " Numerical investigation of the aerodynamic breakup of a parallel moving droplet cluster ", International Journal of Multiphase Flow, vol. 121.
2. D. Stefanitsis, G. Strotos, N. Nikolopoulos, E. Kakaras and M. Gavaises, 2019, "Improved droplet breakup models for spray applications", International Journal of Heat and Fluid Flow, vol. 76, pp. 274-286.
3. D. Stefanitsis, I. Malgarinos, G. Strotos, N. Nikolopoulos, E. Kakaras and M. Gavaises, 2019, "Numerical investigation of the aerodynamic breakup of

- droplets in tandem", *International Journal of Multiphase Flow*, vol. 113, pp. 289-303.
4. D. Stefanitsis, I. Malgarinos, G. Strotos, N. Nikolopoulos, E. Kakaras and M. Gavaises, 2017, "Numerical investigation of the aerodynamic breakup of Diesel and heavy fuel oil droplets", *International Journal of Heat and Fluid Flow*, vol. 68, pp. 203-215.
 5. D. Stefanitsis, P. Koukouvinis, N. Nikolopoulos, M. Gavaises, 2020, "Numerical investigation of the aerodynamic droplet breakup at Mach numbers greater than 1", *Journal of Energy Engineering* (under review).
-

Bibliography

1. Exxon Mobil, *2019 Outlook for Energy: A Perspective to 2040*, 2019.
2. <https://unfccc.int/process-and-meetings/the-paris-agreement/the-paris-agreement>.
3. Reitz, R.D., et al., *IJER editorial: The future of the internal combustion engine*. International Journal of Engine Research. **0**(0): p. 1468087419877990.
4. Guildenbecher, D.R., C. López-Rivera, and P.E. Sojka, *Secondary atomization*. Experiments in Fluids, 2009. **46**(3): p. 371-402.
5. Nicholls, J.A. and A.A. Ranger, *Aerodynamic shattering of liquid drops*. AIAA Journal, 1969. **7**(2): p. 285-290.
6. Ashgriz, N., *Handbook of atomization and sprays: theory and applications* 2011: Springer Science & Business Media.
7. Wadhwa, A.R., V. Magi, and J. Abraham, *Transient deformation and drag of decelerating drops in axisymmetric flows*. Physics of Fluids (1994-present), 2007. **19**(11): p. 113301.
8. Stefanitsis, D., et al., *Numerical investigation of the aerodynamic breakup of droplets in tandem*. International Journal of Multiphase Flow, 2019. **113**: p. 289-303.
9. Theofanous, T.G., *Aerobreakup of Newtonian and Viscoelastic Liquids*. Annual Review of Fluid Mechanics, 2011. **43**(1): p. 661-690.
10. Theofanous, T. and G. Li, *On the physics of aerobreakup*. Physics of Fluids, 2008. **20**(5): p. 052103.
11. Hinze, J.O., *Fundamentals of the hydrodynamic mechanism of splitting in dispersion processes*. AIChE Journal, 1955. **1**(3): p. 289-295.
12. Hanson, A.R., E.G. Domich, and H.S. Adams, *Shock Tube Investigation of the Breakup of Drops by Air Blasts*. The Physics of Fluids, 1963. **6**(8): p. 1070-1080.
13. Gel'fand, B.E., et al., *Singularities of the breakup of viscous liquid droplets in shock waves*. Journal of engineering physics, 1973. **25**(3): p. 1140-1142.
14. Arcoumanis, C., et al., *Breakup of Newtonian and non-Newtonian fluids in air jets*. Experiments in Fluids, 1994. **17**(6): p. 405-414.
15. Hsiang, L.P. and G.M. Faeth, *Drop deformation and breakup due to shock wave and steady disturbances*. International Journal of Multiphase Flow, 1995. **21**(4): p. 545-560.
16. Hsiang, L.P. and G.M. Faeth, *Near-limit drop deformation and secondary breakup*. International Journal of Multiphase Flow, 1992. **18**(5): p. 635-652.
17. Hsiang, L.P. and G.M. Faeth, *Drop properties after secondary breakup*. International Journal of Multiphase Flow, 1993. **19**(5): p. 721-735.
18. Liu, Z. and R.D. Reitz, *An analysis of the distortion and breakup mechanisms of high speed liquid drops*. International Journal of Multiphase Flow, 1997. **23**(4): p. 631-650.

19. Lee, C.H. and R.D. Reitz, *An experimental study of the effect of gas density on the distortion and breakup mechanism of drops in high speed gas stream*. International Journal of Multiphase Flow, 2000. **26**(2): p. 229-244.
20. Lee, C.S. and R.D. Reitz, *EFFECT OF LIQUID PROPERTIES ON THE BREAKUP MECHANISM OF HIGH-SPEED LIQUID DROPS*. 2001. **11**(1): p. 1-19.
21. Park, S.W., S. Kim, and C.S. Lee, *Breakup and atomization characteristics of mono-dispersed diesel droplets in a cross-flow air stream*. International Journal of Multiphase Flow, 2006. **32**(7): p. 807-822.
22. Kim, S., J.W. Hwang, and C.S. Lee, *Experiments and modeling on droplet motion and atomization of diesel and bio-diesel fuels in a cross-flowed air stream*. International Journal of Heat and Fluid Flow, 2010. **31**(4): p. 667-679.
23. Zhao, H., et al., *Experimental study of drop size distribution in the bag breakup regime*. Industrial & Engineering Chemistry Research, 2011. **50**(16): p. 9767-9773.
24. Zhao, H., et al., *Breakup characteristics of liquid drops in bag regime by a continuous and uniform air jet flow*. International Journal of Multiphase Flow, 2011. **37**(5): p. 530-534.
25. Zhao, H., et al., *Temporal properties of secondary drop breakup in the bag-stamen breakup regime*. Physics of Fluids, 2013. **25**(5): p. 054102.
26. Han, J. and G. Tryggvason, *Secondary breakup of axisymmetric liquid drops. II. Impulsive acceleration*. Physics of Fluids, 2001. **13**(6): p. 1554-1565.
27. Aalburg, C., *Deformation and breakup of round drops and nonturbulent liquid jets in uniform crossflows*2002.
28. Quan, S. and D.P. Schmidt, *Direct numerical study of a liquid droplet impulsively accelerated by gaseous flow*. Physics of Fluids (1994-present), 2006. **18**(10): p. 102103.
29. Jing, L. and X. Xu, *Direct Numerical Simulation of Secondary Breakup of Liquid Drops*. Chinese Journal of Aeronautics, 2010. **23**(2): p. 153-161.
30. Kékesi, T., G. Amberg, and L. Prahla Wittberg, *Drop deformation and breakup*. International Journal of Multiphase Flow, 2014. **66**: p. 1-10.
31. Yang, W., et al., *Influence of density ratio on the secondary atomization of liquid droplets under highly unstable conditions*. Fuel, 2016. **174**: p. 25-35.
32. Yang, W., et al., *Transitions of deformation to bag breakup and bag to bag-stamen breakup for droplets subjected to a continuous gas flow*. International Journal of Heat and Mass Transfer, 2017. **111**: p. 884-894.
33. Shao, C., K. Luo, and J. Fan, *Detailed numerical simulation of unsteady drag coefficient of deformable droplet*. Chemical Engineering Journal, 2017. **308**: p. 619-631.
34. Theofanous, T., et al., *The physics of aerobreakup. II. Viscous liquids*. Physics of Fluids, 2012. **24**(2): p. 022104.
35. Xiao, F., et al., *Simulation of drop deformation and breakup in supersonic flow*. Proceedings of the Combustion Institute, 2017. **36**(2): p. 2417-2424.
36. Joseph, D.D., J. Belanger, and G. Beavers, *Breakup of a liquid drop suddenly exposed to a high-speed airstream*. International Journal of Multiphase Flow, 1999. **25**(6-7): p. 1263-1303.
37. Joseph, D., G. Beavers, and T. Funada, *Rayleigh–Taylor instability of viscoelastic drops at high Weber numbers*. Journal of Fluid Mechanics, 2002. **453**: p. 109-132.
38. Pilch, M. and C.A. Erdman, *Use of breakup time data and velocity history data to predict the maximum size of stable fragments for acceleration-induced breakup of a liquid drop*. International Journal of Multiphase Flow, 1987. **13**(6): p. 741-757.
39. Engel, O.G., *Fragmentation of Waterdrops in the Zone Behind an Air Shock*, J. Research Nat'i. Bur. Stds, 1958. **60**(245): p. 19.

40. Boiko, V., A. Papyrin, and S. Poplavskii, *Dynamics of droplet breakup in shock waves*. Journal of applied mechanics and technical physics, 1987. **28**(2): p. 263-269.
41. Boiko, V. and S. Poplavski, *On the dynamics of drop acceleration at the early stage of velocity relaxation in a shock wave*. Combustion, Explosion, and Shock Waves, 2009. **45**(2): p. 198-204.
42. Wierzba, A. and K. Takayama, *Experimental investigation of the aerodynamic breakup of liquid drops*. AIAA Journal, 1988. **26**(11): p. 1329-1335.
43. Yoshida, T. and K. Takayama, *Interaction of liquid droplets with planar shock waves*. Journal of Fluids Engineering, 1990. **112**(4): p. 481-486.
44. Yi, X., Y. Zhu, and J. Yang. *On the Early-Stage Deformation of Liquid Drop in Shock-Induced Flow*. in *30th International Symposium on Shock Waves 2*. 2017. Springer.
45. Hébert, D., et al., *Investigation of mechanisms leading to water drop breakup at Mach 4.4 and Weber numbers above 105*. SN Applied Sciences, 2019. **2**(1): p. 69.
46. Surov, V., *Numerical modeling of the interaction of a strong shock wave with liquid drops*. Journal of applied mechanics and technical physics, 1995. **36**(3): p. 354-359.
47. Boiko, V.M., A.N. Papyrin, and S.V. Poplavskii, *Dynamics of droplet breakup in shock waves*. Journal of applied mechanics and technical physics, 1987. **28**(2): p. 263-269.
48. Liou, M.-S., et al., *Numerical study of shock-driven deformation of interfaces*, in *Shock Waves 2009*, Springer. p. 919-924.
49. Chang, C.-H., X. Deng, and T.G. Theofanous, *Direct numerical simulation of interfacial instabilities: a consistent, conservative, all-speed, sharp-interface method*. Journal of Computational Physics, 2013. **242**: p. 946-990.
50. Chang, C.-H. and M.-S. Liou, *A robust and accurate approach to computing compressible multiphase flow: Stratified flow model and AUSM+ scheme*. Journal of Computational Physics, 2007. **225**(1): p. 840-873.
51. Guan, B., et al., *Numerical Study on Liquid Droplet Internal Flow Under Shock Impact*. AIAA Journal, 2018. **56**(9): p. 3382-3387.
52. Meng, J.C. and T. Colonius, *Numerical simulation of the aerobreakup of a water droplet*. Journal of Fluid Mechanics, 2018. **835**: p. 1108-1135.
53. Meng, J.C.C., *Numerical simulations of droplet aerobreakup*, 2016, California Institute of Technology.
54. Kaiser, J., S. Adami, and N.A. Adams. *Direct Numerical Simulation of Shock-Induced Drop Breakup with a Sharp-Interface-Method*. in *Symposium on Turbulence and Shear Flow Phenomena [TSFP10]*. 2017.
55. Liu, N., et al., *Numerical simulation of liquid droplet breakup in supersonic flows*. Acta Astronautica, 2018. **145**: p. 116-130.
56. Prael, L., J. Revstedt, and L. Fuchs. *Interaction among droplets in a uniform flow at intermediate Reynolds numbers*. in *44th AIAA Aerospace Sciences Meeting and Exhibit, Reno, Nevada, USA, January*. 2006.
57. Kékesi, T., et al., *Interaction between two deforming liquid drops in tandem and various off-axis arrangements subject to uniform flow*. International Journal of Multiphase Flow, 2019. **112**: p. 193-218.
58. Liu, D., K. Anders, and A. Frohn, *Drag coefficients of single droplets moving in an infinite droplet chain on the axis of a tube*. International Journal of Multiphase Flow, 1988. **14**(2): p. 217-232.
59. Mulholland, J., R. Srivastava, and J. Wendt, *Influence of droplet spacing on drag coefficient in nonevaporating, monodisperse streams*. AIAA Journal, 1988. **26**(10): p. 1231-1237.

60. Temkin, S. and G. Ecker, *Droplet pair interactions in a shock-wave flow field*. Journal of Fluid Mechanics, 1989. **202**: p. 467-497.
61. Poo, J. and N. Ashgriz, *Variation of drag coefficients in an interacting drop stream*. Experiments in Fluids, 1991. **11**(1): p. 1-8.
62. Nguyen, Q. and D. Dunn-Rankin, *Experiments examining drag in linear droplet packets*. Experiments in Fluids, 1992. **12**(3): p. 157-165.
63. Connon, C. and D. Dunn-Rankin, *Flow behavior near an infinite droplet stream*. Experiments in Fluids, 1996. **21**(2): p. 80-86.
64. Holländer, W. and S. Zaripov, *Hydrodynamically interacting droplets at small Reynolds numbers*. International Journal of Multiphase Flow, 2005. **31**(1): p. 53-68.
65. Zhao, H., et al., *Interaction of two drops in the bag breakup regime by a continuous air jet*. Fuel, 2019. **236**: p. 843-850.
66. Kim, I., S. Elghobashi, and W. Sirignano, *Three-dimensional droplet interactions in dense sprays*, in *29th Aerospace Sciences Meeting* 1991, American Institute of Aeronautics and Astronautics.
67. Kim, I., S. Elghobashi, and W. Sirignano. *Three-dimensional flow computation for two interacting, moving droplets*. in *AIAA Materials Specialist Conference-Coating Technology for Aerospace Systems*. 1992.
68. Kim, I., S. Elghobashi, and W.A. Sirignano, *Three-dimensional flow over two spheres placed side by side*. Journal of Fluid Mechanics, 1993. **246**: p. 465-488.
69. Quan, S. *Dynamics of Droplets Impulsively Accelerated by Gaseous Flow: A Numerical Investigation*. in *ICLASS 2009, 11th Triennial International Annual Conference on Liquid Atomization and Spray Systems*. 2009. Vail, Colorado, USA.
70. Quan, S., J. Lou, and H.A. Stone, *Interactions between two deformable droplets in tandem subjected to impulsive acceleration by surrounding flows*. Journal of Fluid Mechanics, 2011. **684**: p. 384-406.
71. Magi, V. and J. Abraham, *Drop Interactions in Transient Flows with Applications to Liquid Sprays*, in *18th Australasian Fluid Mechanics Conference* 2012: Launceston, Australia.
72. ANSYS®FLUENT Theory Guide, 2014, Release 16.0.
73. Gel'Fand, B., S. Gubin, and S. Kogarko, *Various forms of drop fractionation in shock waves and their special characteristics*. Journal of Engineering Physics and Thermophysics, 1974. **27**(1): p. 877-882.
74. Chou, W.H. and G.M. Faeth, *Temporal properties of secondary drop breakup in the bag breakup regime*. International Journal of Multiphase Flow, 1998. **24**(6): p. 889-912.
75. Cao, X.-K., et al., *A new breakup regime of liquid drops identified in a continuous and uniform air jet flow*. Physics of Fluids, 2007. **19**(5): p. 057103.
76. Kulkarni, V. and P. Sojka, *Bag breakup of low viscosity drops in the presence of a continuous air jet*. Physics of Fluids, 2014. **26**(7): p. 072103.
77. Dai, Z. and G.M. Faeth, *Temporal properties of secondary drop breakup in the multimode breakup regime*. International Journal of Multiphase Flow, 2001. **27**(2): p. 217-236.
78. Jain, M., et al., *Secondary breakup of a drop at moderate Weber numbers*. Proceedings of the Royal Society A: Mathematical, Physical and Engineering Science, 2015. **471**(2177).
79. Krzeczowski, S.A., *Measurement of liquid droplet disintegration mechanisms*. International Journal of Multiphase Flow, 1980. **6**(3): p. 227-239.

80. O'Rourke, P.J., A.A. Amsden, and E. Society of Automotive, *The tab method for numerical calculation of spray droplet breakup* 1987, Warrendale, PA: Society of Automotive Engineers.
81. Lee, M.W., et al., *Comparison and correction of the drop breakup models for stochastic dilute spray flow*. Applied Mathematical Modelling, 2012. **36**(9): p. 4512-4520.
82. Marek, M., *The double-mass model of drop deformation and secondary breakup*. Applied Mathematical Modelling, 2013. **37**(16-17): p. 7919-7939.
83. Villermaux, E. and B. Bossa, *Single-drop fragmentation determines size distribution of raindrops*. Nature Physics, 2009. **5**: p. 697.
84. Opfer L., I.V.R., C. Tropea, *Aerodynamic Fragmentation of Drops: Dynamics of the Liquid Bag*, in *ICLASS 2012, 12th Triennial International Conference on Liquid Atomization and Spray Systems* 2012: Heidelberg, Germany.
85. Detkovskii, D. and S. Frolov, *Model of the deformation of a liquid droplet in a gas flow*. Journal of applied mechanics and technical physics, 1994. **35**(6): p. 911-919.
86. Wang, C., et al., *Modeling of drop breakup in the bag breakup regime*. Applied Physics Letters, 2014. **104**(15): p. 154107.
87. Wang, C., et al., *Theoretical Modeling of Spray Drop Deformation and Breakup in the Multimode Breakup Regime*. Atomization and Sprays, 2015. **25**(10).
88. Ibrahim, E., H. Yang, and A. Przekwas, *Modeling of spray droplets deformation and breakup*. Journal of Propulsion and Power, 1993. **9**(4): p. 651-654.
89. Rimbert, N., et al., *A New Look at the Droplet Deformation and Breakup Model*, in *ILASS2014*.
90. Schmehl, R., *Advanced modeling of droplet deformation and breakup for CFD analysis of mixture preparation*. Zaragoza, 2002. **9**(11).
91. Bartz, F., et al. *An extension of dynamic droplet deformation models to secondary atomization*. in *23rd Annual Conference on Liquid Atomization and Spray Systems, Brno*. 2010.
92. Bartz, F., et al. *Model comparison for single droplet fragmentation under varying accelerations*. in *24th European conference on liquid atomization and spray systems*. 2011.
93. Sichani, A.B. and M.D. Emami, *A droplet deformation and breakup model based on virtual work principle*. Physics of Fluids, 2015. **27**(3): p. 032103.
94. Majithia, A., et al. *Droplet breakup quantification and processes in constant and pulsed air flows*. in *Proceedings of the 22nd Conference on Liquid Atomization and Spray Systems (ILASS-Europe), Como Lake, Italy*. 2008.
95. O'Rourke, P.J. and A.A. Amsden, *The TAB method for numerical calculation of spray droplet breakup*, 1987, SAE Technical Paper.
96. Kolev, N.I., *Diesel fuel properties*, in *Multiphase Flow Dynamics 4* 2012, Springer Berlin Heidelberg.
97. Kyriakides, N., C. Chryssakis, and L. Kaiktsis, *Influence of Heavy Fuel Properties on Spray Atomization for Marine Diesel Engine Applications*, 2009, SAE International.
98. Hirt, C.W. and B.D. Nichols, *Volume of fluid (VOF) method for the dynamics of free boundaries*. Journal of Computational Physics, 1981. **39**(1): p. 201-225.
99. Lafaurie, B., et al., *Modelling Merging and Fragmentation in Multiphase Flows with SURFER*. Journal of Computational Physics, 1994. **113**(1): p. 134-147.
100. Sonntag, R.E., G.J. Van Wylen, and C. Borgnakke, *Fundamentals of thermodynamics* 2008: Wiley.
101. Gor, G.Y., et al., *Modulus–pressure equation for confined fluids*. The Journal of chemical physics, 2016. **145**(16): p. 164505.

102. Iivings, M., D. Causon, and E. Toro, *On Riemann solvers for compressible liquids*. International Journal for Numerical Methods in Fluids, 1998. **28**(3): p. 395-418.
103. Menon, E.S., *Transmission pipeline calculations and simulations manual*2014: Gulf Professional Publishing.
104. Perry, R.H. and D.W. Green, *Perry's Chemical Engineers' Handbook-Cdrom*1999: McGraw Hill.
105. Sutherland, W., *LII. The viscosity of gases and molecular force*. The London, Edinburgh, and Dublin Philosophical Magazine and Journal of Science, 1893. **36**(223): p. 507-531.
106. ANSYS®FLUENT User's Guide, 2018, Release 19.2.
107. Morsi, S. and A. Alexander, *An investigation of particle trajectories in two-phase flow systems*. Journal of Fluid Mechanics, 1972. **55**(2): p. 193-208.
108. ANSYS®FLUENT, 2014, Release 16.0.
109. ANSYS®FLUENT, 2018, Release 19.2.
110. Versteeg, H.K. and W. Malalasekera, *An introduction to computational fluid dynamics: the finite volume method*2007: Pearson Education.
111. Issa, R.I., *Solution of the implicitly discretised fluid flow equations by operator-splitting*. Journal of Computational Physics, 1986. **62**(1): p. 40-65.
112. Barth, T. and D. Jespersen. *The design and application of upwind schemes on unstructured meshes*. in *27th Aerospace sciences meeting*. 1989.
113. Malgarinos, I., N. Nikolopoulos, and M. Gavaises, *Coupling a local adaptive grid refinement technique with an interface sharpening scheme for the simulation of two-phase flow and free-surface flows using VOF methodology*. Journal of Computational Physics, 2015. **300**: p. 732-753.
114. Strotos, G., et al., *Numerical investigation of aerodynamic droplet breakup in a high temperature gas environment*. Fuel, 2016. **181**: p. 450-462.
115. Jain, S.S., et al., *Secondary breakup of drops at moderate Weber numbers: Effect of Density ratio and Reynolds number*. arXiv preprint arXiv:1803.02989, 2018.
116. Liang, C., *Computational methods for the investigation of liquid drop phenomena in external gas flows*, 2016, Michigan Technological University.
117. Stefanitsis, D., et al., *Numerical investigation of the aerodynamic breakup of Diesel and heavy fuel oil droplets*. International Journal of Heat and Fluid Flow, 2017. **68**: p. 203-215.
118. Kékesi, T., et al., *Interaction between two deforming liquid drops in tandem and various off-axis arrangements subject to uniform flow*. 2017.
119. Strotos, G., et al., *Aerodynamic breakup of an n-decane droplet in a high temperature gas environment*. Fuel, 2016. **185**: p. 370-380.
120. Yaws, C.L. and C. Gabbula, *Yaws" Handbook of Thermodynamic and Physical Properties of Chemical Compounds*2003: Knovel.
121. Vidal, A., et al., *Modelling of Diesel fuel properties through its surrogates using Perturbed-Chain, Statistical Associating Fluid Theory*. International Journal of Engine Research. **0**(0): p. 1468087418801712.
122. Malgarinos, I., et al., *VOF simulations of the contact angle dynamics during the drop spreading: Standard models and a new wetting force model*. Advances in Colloid and Interface Science, 2014. **212**: p. 1-20.
123. Malgarinos, I., N. Nikolopoulos, and M. Gavaises, *A numerical study on droplet-particle collision dynamics*. International Journal of Heat and Fluid Flow, 2016. **61, Part B**: p. 499-509.
124. Malgarinos, I., N. Nikolopoulos, and M. Gavaises, *Numerical investigation of heavy fuel droplet-particle collisions in the injection zone of a Fluid Catalytic Cracking*

- reactor, Part I: Numerical model and 2D simulations. Fuel Processing Technology, 2017. **156**: p. 317-330.
125. Malgarinos, I., N. Nikolopoulos, and M. Gavaises, *Numerical investigation of heavy fuel droplet-particle collisions in the injection zone of a Fluid Catalytic Cracking reactor, part II: 3D simulations*. Fuel Processing Technology, 2017. **156**: p. 43-53.
 126. G. Strotos, I.M., N. Nikolopoulos, K. Papadopoulos, A. Theodorakakos, M.Gavaises, *Performance of VOF methodology in predicting the deformation and breakup of impulsively accelerated droplets*, in *ICLASS 2015, 13th Triennial International Conference on Liquid Atomization and Spray Systems, August 23-27 2015*: Tainan, Taiwan.
 127. Strotos, G., et al., *Predicting droplet deformation and breakup for moderate Weber numbers*. International Journal of Multiphase Flow, 2016. **85**: p. 96-109.
 128. Stefanitsis, D., et al., *Numerical investigation of the aerodynamic breakup of Diesel droplets under various gas pressures*, in *28th Conference on Liquid Atomization and Spray Systems (ILASS-Europe 2017)* 2017: Valencia, Spain.
 129. Stefanitsis, D., et al., *Numerical examination of the aerodynamic breakup of droplets in chain formation*, in *14th Triennial International Conference on Liquid Atomization and Spray Systems (ICLASS 2018)* 2018: Chicago, USA.
 130. Stefanitsis, D., et al., *Numerical investigation of the aerodynamic breakup of droplets in tandem*. International Journal of Multiphase Flow, 2018.
 131. Stefanitsis, D., et al., *Improved droplet breakup models for spray applications*. International Journal of Heat and Fluid Flow, 2019. **76**: p. 274-286.
 132. Strotos, G., et al., *Predicting the evaporation rate of stationary droplets with the VOF methodology for a wide range of ambient temperature conditions*. International Journal of Thermal Sciences, 2016. **109**: p. 253-262.
 133. Temkin, S. and G.Z. Ecker, *Droplet pair interactions in a shock-wave flow field*. Journal of Fluid Mechanics, 1989. **202**: p. 467-497.
 134. Clift, R., J.R. Grace, and M.E. Weber, *Bubbles, drops, and particles* 2005: Courier Corporation.
 135. Kiya, M., H. Ishikawa, and H. Sakamoto, *Near-wake instabilities and vortex structures of three-dimensional bluff bodies: a review*. Journal of Wind Engineering and Industrial Aerodynamics, 2001. **89**(14–15): p. 1219-1232.
 136. Sakamoto, H. and H. Haniu, *A study on vortex shedding from spheres in a uniform flow*.
 137. Achenbach, E., *Vortex shedding from spheres*. Journal of Fluid Mechanics, 1974. **62**(02): p. 209-221.
 138. Toro, E.F., *The Riemann Problem for the Euler Equations*, in *Riemann Solvers and Numerical Methods for Fluid Dynamics: A Practical Introduction*, E.F. Toro, Editor 1997, Springer Berlin Heidelberg: Berlin, Heidelberg. p. 115-157.
 139. Meng, J. and T. Colonius, *Numerical simulations of the early stages of high-speed droplet breakup*. Shock Waves, 2015. **25**(4): p. 399-414.
 140. Koukouvinis, P., et al., *Numerical simulation of a collapsing bubble subject to gravity*. Physics of Fluids, 2016. **28**(3): p. 032110.
 141. Igra, D. and K. Takayama, *A study of shock wave loading on a cylindrical water column*. Report of the Institute of Fluid Science, Tohoku University, 2001. **13**: p. 19-36.
 142. Igra, D. and K. Takayama, *Numerical simulation of shock wave interaction with a water column*. Shock Waves, 2001. **11**(3): p. 219-228.
 143. Quirk, J.J. and S. Karni, *On the dynamics of a shock–bubble interaction*. Journal of Fluid Mechanics, 1996. **318**: p. 129-163.

144. Johnsen, E., *Numerical simulations of non-spherical bubble collapse: With applications to shockwave lithotripsy*, 2008, California Institute of Technology.
145. Coralic, V. and T. Colonius, *Finite-volume WENO scheme for viscous compressible multicomponent flows*. *Journal of Computational Physics*, 2014. **274**: p. 95-121.
146. Strotos, G., et al., *Numerical investigation on the evaporation of droplets depositing on heated surfaces at low Weber numbers*. *International Journal of Heat and Mass Transfer*, 2008. **51**(7-8): p. 1516-1529.
147. Strotos, G., et al., *Numerical investigation of the evaporation of two-component droplets*. *Fuel*, 2011. **90**(4): p. 1492-1507.
148. Khare P., V.Y. *Drag Coefficients of Deforming and Fragmenting Liquid Droplets*. in *ILASS Americas, 25th Annual Conference on Liquid Atomization and Spray Systems*. 2013. Pittsburgh, PA.
149. Hirahara, H. and M. Kawahashi, *Experimental investigation of viscous effects upon a breakup of droplets in high-speed air flow*. *Experiments in Fluids*, 1992. **13**(6): p. 423-428.
150. Strotos, G., et al., *Determination of the aerodynamic droplet breakup boundaries based on a total force approach*. *International Journal of Heat and Fluid Flow*, 2018. **69**: p. 164-173.
151. Lacaze, G., et al., *Analysis of high-pressure Diesel fuel injection processes using LES with real-fluid thermodynamics and transport*. *Proceedings of the Combustion Institute*, 2015. **35**(2): p. 1603-1611.
152. Mueller, C.J., et al., *Diesel Surrogate Fuels for Engine Testing and Chemical-Kinetic Modeling: Compositions and Properties*. *Energy & Fuels*, 2016. **30**(2): p. 1445-1461.
153. Loth, E. and A.J. Dorgan, *An equation of motion for particles of finite Reynolds number and size*. *Environmental fluid mechanics*, 2009. **9**(2): p. 187-206.
154. Liu, A.B., D. Mather, and R.D. Reitz, *Modeling the effects of drop drag and breakup on fuel sprays*, 1993, WISCONSIN UNIV-MADISON ENGINE RESEARCH CENTER.
155. Schlottke, M., *Analytical Investigation of Droplet Breakup in Accelerated Flow*, in *Institut für Thermodynamik der Luft- und Raumfahrt (ITLR)2011*, Universität Stuttgart.
156. Dormand, J.R. and P.J. Prince, *A family of embedded Runge-Kutta formulae*. *Journal of computational and applied mathematics*, 1980. **6**(1): p. 19-26.
157. Shampine, L.F. and M.W. Reichelt, *The matlab ode suite*. *SIAM journal on scientific computing*, 1997. **18**(1): p. 1-22.